Author/s:
Yuan, Meng

Title:
A Model-based Approach for High Performance Motion Control in Industrial Machines

Date:
2020

Persistent Link:
https://hdl.handle.net/11343/240434

A Model-based Approach for High Performance Motion Control in Industrial Machines

Meng Yuan
ORCID: 0000-0002-0875-0127

Submitted in partial fulfilment of the requirements of the degree of

Doctor of Philosophy

Department of Electrical and Electronic Engineering
THE UNIVERSITY OF MELBOURNE

February 2020

Produced on archival quality paper.

Abstract

Industrial robotics typically consider laser/water cutting, grinding, etc. Within these machines, the motion controller is responsible for the positioning of the end effector. The performance of the motion controller directly influences the quality of the resulting product as tolerance/accuracy are surrogates for machining quality. This is particularly relevant in tracking and contouring applications when the system has structural flexibility, and no direct feedback measurement of the end-effector position is available. Traditional control architectures in machining are unable to explicitly bound tracking and/or contouring errors, and conservative operation is used to ensure satisfactory performance of the overall system. Bounding errors without unduly compromising machine throughput requires advanced control algorithms. The development of such algorithms is the focus of this thesis.

Although numerous control methods are proposed, the proportional integral derivative (PID) based cascaded control is still the most prevalent in the industry. Based on this fact, the research starts by objectively assessing the tracking control performance on a single-axis industrial platform. The results provide practitioners with an in-depth understanding of the benefits and limitations of existing control algorithms as well as the motivation to consider advanced controllers as alternatives to the PID-based approach.

For the single-axis tracking problem, this research proposes a model predictive based approach that guarantees a desired level of tracking error is met for the cases where the structure is flexible and the end-effector position is estimated. To achieve this, a robust control invariant set is estimated using a computationally tractable algorithm and incorporated into the problem formulation. The applicability of the proposed approach

is successfully demonstrated via simulation and experiments conducted on a commercial single-axis system.

In terms of biaxial applications, the dual-drive gantry machines are widely used in industry for manufacturing. However, the non-synchronised movement of the dual drive may lead to deterioration in contouring accuracy. In this research, we propose two model predictive based control architectures based on the switched linear time invariant control-oriented models, that is able to guarantee a two-dimensional contouring tolerance in the presence of uncertainty arising from imperfect drive synchronisation. The performance and computational tractability of the proposed approach are demonstrated using high fidelity simulation and experiment.

Declaration

This is to certify that

1. the thesis comprises only my original work towards the PhD,
2. due acknowledgement has been made in the text to all other material used,
3. the thesis is less than 100,000 words in length, exclusive of tables, maps, bibliographies and appendices.

Meng Yuan, February 2020

This page intentionally left blank.

Preface

This thesis describes the original research work that I completed during my Ph.D. candidature at the University of Melbourne.

The main contributions of this thesis are presented in Chapters 2 - 5. I conducted the majority of the research works, including the problem formulation, theoretical analysis, test bench setup, system identification, simulations and experiments. Prof. Chris Manzie and A/Prof. Iman Shames supervised all the work and provided me with enlightening guidance.

The summary of publications to relevant chapters is given as below:

- Most of the work in Chapters 2 and 3 is in revision by *Control Engineering Practice*.
- The work in Chapter 4 has been published by *IEEE Transactions on Industrial Electronics*, 2019 and *IEEE International Conference on Industrial Technology (ICIT)*, 2019.
- Part of the work in Chapter 5 has been published by *IEEE Conference on Control Technology and Applications (CCTA)*, 2019.
- Part of the work in Chapter 5 is unpublished material and will be submitted for journal publication.

The experiments in publications are completed with the support of Dr. Lu Gan, Dr. Farzad Keynejad and Troy Robinette from ANCA Motion, Melbourne. Co-author Prof. Malcolm Good provided the comments for the manuscript.

All the work towards the thesis was carried out after the enrolment in the degree and the work has not been submitted for other qualifications. No third party editorial assistance was provided in the preparation of this thesis.

The research work was supported by the University of Melbourne through the Melbourne International Fee Remission Scholarship (MIFRS) and Melbourne International Research Scholarship (MIRS).

Acknowledgements

First, I would like to express my sincere gratitude towards my supervisors. I am thankful to my primary supervisor Professor Chris Manzie, for his continuous encouragement, thoughtful mentorship, and unwavering support during my Ph.D. time. A deep thanks also go to my co-supervisor Associate Professor Iman Shames, for many helpful and productive discussions when I was confused. It has been a great honour to work with them.

I would also like to thank Professor Malcolm Good, for all the effort he put in discussion and guidance. Although he was not my official supervisor, he was always there to help me when there were problems.

Throughout this research, I was fortunate to work with the industry partner, ANCA Motion in Melbourne. I wish to thank Troy Robinette and Dr. Farzad Keynejad for providing me with the opportunity to work on this interesting project. Great thanks go to Dr. Lu Gan for his prompt help whenever I had an implementation issue. In addition, the assistance provided by Tomas Frier and Nicholas Loh in building the test bench is greatly appreciated. I also want to mention Tracy Xing, Wenny Zhou, Steven Yu and Heng Luo, thanks for every friendly and warm lunchtime in ANCA Motion.

I am also grateful to the University of Melbourne for the financial support through the Melbourne International Fee Remission Scholarship (MIFRS) and Melbourne International Research Scholarship (MIRS) during my Ph.D. candidature.

My gratitude also goes to my colleagues in the research group. During the four years, members of this group have come and gone, but our friendship remains. I would like

to thank, Chenyang Liu, Gokul Sankar, Kaixiang Wang, Yaqi Zhu, Robert Chin, Noam Olshina, Will Clarke, Chwen-kai Liao, Changfu Zou and Ye Wang, for all the happy times together.

My thanks go to two of my closest friends, Chuan Wang and Yang Liu as well, for their continuous support and encouragement.

Finally, my deepest gratitude goes to my parents Yongqing Yuan and Zhifang Zhang, for their unconditional love and support throughout my life. A special thanks to my wife, Meng Qin, for staying with me during the ups and downs in the last four years. I sincerely appreciate the enjoyable life she brought with her optimism.

Dedicated to my beloved family and friends

This page intentionally left blank.

Contents

This page intentionally left blank.

List of Figures

Symbols and Acronyms

Symbols

(a, b)	Stacked vector $(a, b) \triangleq \left[a^T, b^T\right]^T \in \mathbb{R}^{n_a+n_b}$ if vectors $a \in \mathbb{R}^{n_a}, b \in \mathbb{R}^{n_b}$
$0_{m,n}$	Zero matrix with size m-by-n
ϵ_c	Desired contouring error tolerance
ϵ_e	Desired tracking error tolerance
ϵ_o	Upper bound of end-effector position estimation error
$\|S\|_\infty$	Matrix ∞-norm of $S \in \mathbb{R}^{m\times n}$, i.e., $\|S\|_\infty = \max_{i\in 1,\cdots,m} \sum_{j=1}^{n} \|s_{i,j}\|$
$\|x\|_Q^2$	For a column vector $x \in \mathbb{R}^n$ and matrix $Q \in \mathbb{R}^{n\times n}$, $\|x\|_Q^2 \triangleq x^T Q x$
$\mathbb{R}\,(\mathbb{R}_+, \mathbb{R}_{0+})$	Set of (positive, nonnegative) real numbers
$\mathbb{R}^n$	Set of real vectors with n elements
$\mathbb{Z}\,(\mathbb{Z}_+, \mathbb{Z}_{0+})$	Set of (positive, nonnegative) integer numbers
$\mathbb{Z}_{[a,b]}$	Set of integer numbers with elements from $a, \cdots, b$ for $a, b \in \mathbb{Z}$
b_x, b_y	Viscous friction coefficient on X and Y axes respectively
$diag(a, \cdots, b)$	Square diagonal matrix with entries $a, \cdots, b$
I_n	Identity matrix with size n
k_x, k_y	Force constant of X and Y axes motors respectively
L	Half length of the crossbeam
M_e	Mass of end-effector/head drive
M_m	Mass of actuator drive
w_N	Half width of the crossbeam

$x(i\|k)$	Predicted state vector at sampling instant $k+i$, $i>0$, given $x(k)$
$x(k)$	Value of x at sampling instant k, the time $T_s \cdot k$, where T_s is the sampling period
x_e	Position of end-effector in X axis direction
x_h	Position of end-effector in X' axis direction
x_m	Position of actuator in X axis direction
y_N	Position of center of mass for gantry beam in Y axis direction

Acronyms

CCC	Cross Coupled Control
CEBC	Contouring Error Bounded Control
CNC	Computer Numerical Control
CoM	Center of Mass
DEBC	Disturbance Estimation Based Control
DOB	Disturbance Observer
ESO	Extended State Observer
LESO	Linear Extended State Observer
LTI	Linear Time Invariant
MPC	Model Predictive Control
NLESO	Nonlinear Extended State Observer
PID	Proportional–integral–derivative
RAI	Robust Admissible Input
RCI	Robust Control Invariant

Chapter 1

Introduction

IN 2016, the size of the global industrial motion control market was $US 16.54 billion and is expected to reach approximately $US 22.8 billion by 2022 [1]. To retain a competitive advantage in the manufacturing market, two competing performance metrics, namely speed and precision, are highly valued by manufacturers. Manufacturing outcomes largely depend on the performance of motion control systems.

Motion control mainly involves the control of actuators, such as feed drives, to perform desired coordinated motion at the end effector side. The structure of a general motion control system is given as Fig. 1.1. The specifications of desired motion are sent through the human machine interface (HMI) by operators; the computer numerical controller (CNC) then coordinates the entire motion and generates the position commands with jerk, acceleration and/or velocity constraints. The drive sequentially determines the voltage to be applied to the motor based on the reference signal and the feedback measurements at each time step.

From the perspective of productivity, it is desirable that the machining is conducted with sufficient average speed. For this type of problem, the time-parameterised reference representing the desired path is given.

For applications such as grasping, cutting and scanning, multi-axes movement is involved, necessitating the coordinated control of each axis. Due to the fact that uncertainties/disturbance existing in the system and high-frequency dynamics are neglected in the control-oriented model, it is not surprising that the controlled end effector cannot follow the path exactly during the whole process. Consequently, one

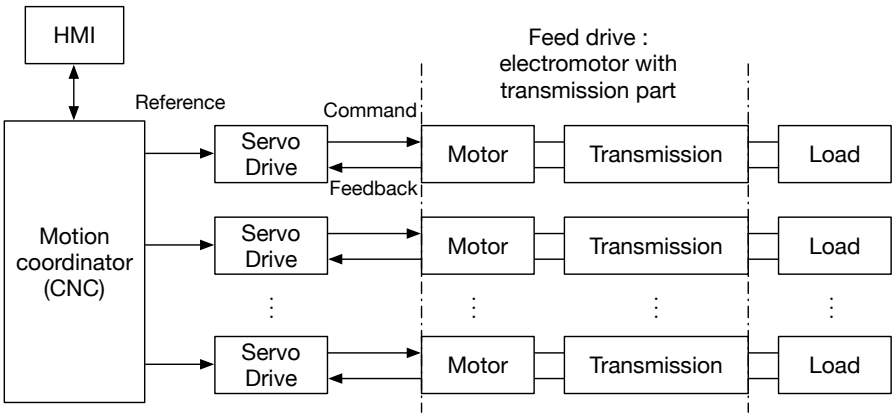

Fig. 1.1: Structure of industrial motion control.

goal of motion control is to ensure the contouring error, the shortest distance between the end-effector position and the desired contour, stays within a tolerance bounds in order to guarantee the product quality [2].

The traditional control architectures in machining are unable to bound the tracking and contouring errors explicitly, and therefore conservative operation is required to ensure satisfactory performance of the overall system. The focus of this thesis is to develop and test control algorithms for error bounded tracking and contouring without unduly compromising the machine throughput.

1.1 Trajectory tracking control and contouring control

Before moving to the control problem, two different terminologies, namely tracking error and contouring error, and the linkage between them is explained.

For a biaxial system as shown in Fig. 1.2, let the actual location of the end effector at time k be $(x_e(k), y_e(k))$ and the time-dependent reference position be $(x_e^*(k), y_e^*(k))$. The error $e_c(k) \triangleq \|(x_e^*(k) - x_e(k), y_e^*(k) - y_e(k))\|_2$ is the distance between the actual and reference position. Let $(x_e^c(k), y_e^c(k))$ be the closest projection of the end-effector onto the desired path, then the contouring error is $\epsilon(k)$ which arises due to tracking error in each of the axes [3].

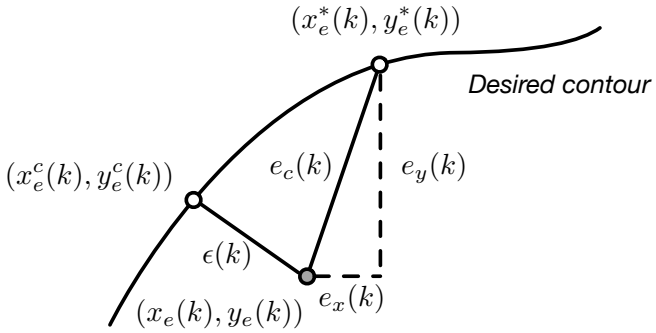

Fig. 1.2: Tracking error and contouring error.

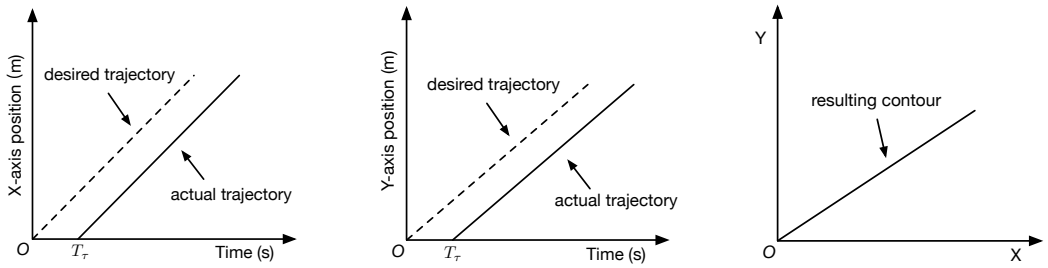

Fig. 1.3: Zero contour error with non-zero tracking error: (a) desired and actual trajectory of X axis; (b) desired and actual trajectory of Y axis; (c) resulting contour.

The contouring error not only relies on the current end-effector position but also relates to the shape of the path. As mentioned in [3], the existence of contouring error definitely indicates the existence of tracking error. However, the opposite conclusion does not always hold. For example, as a simple case shown in Fig. 1.3, tracking a biaxial linear path with same delay T_τ on both axes results in non-zero tracking errors but zero contouring error.

Although large tracking error may result in a relatively small contouring error, this does not mean reducing tracking error does not have impact on the contouring error. Considering the biaxial application in Fig. 1.2 again, since $(x_e^c(k), y_e^c(k))$ is the closest point from the actual end effector position and the triangle inequality $e_c(k) \leq |e_x(k)| + |e_y(k)|$ holds, we can have inequalities between tracking and contouring error

as follows:

$$\epsilon(k) \leq e_c(k) \leq |e_x(k)| + |e_y(k)|. \tag{1.1}$$

The internal relation (1.1) shows that the contouring error can be bounded within a desired tolerance by applying a tracking error constraint on each axis. Therein, two approaches are mainly used to reduce the contouring error in industrial manufacturing. The first is the trajectory *tracking control* method which intends to reduce the tracking error of each axis and ultimately improving the contouring performance indirectly. The second is the *contouring control* method, where the control law is designed based on the explicit consideration of the real-time estimated or calculated contouring error.

Therefore, the tracking error bounded control for single axis machines and contouring error bounded control problem for biaxial machines are investigated in this thesis.

1.2 Challenges in motion control

For machine manufacturers, the desire to reduce machine cost while retaining high speed and acceleration properties have led to lighter structures for given motor specifications [4, 5]. The lighter component means more flexible mechanical structures. The inherent flexibility of the transmission parts and the non-rigid characteristics of the lighter manipulator result in vibration and oscillation during the manufacturing process. The resulting vibration not only deteriorates the tracking accuracy but also reduces the throughput, as avoiding vibration requires lower acceleration and jerk reference trajectories [6].

In addition to structural flexibility, the non-rigid feature of transmission parts and manipulator may cause a discrepancy between the motor (actuator) and end effector (load) position. The desire to control the position of the end-effector with a non-collocated actuator and sensor spacial location results in a non-minimum phase system, which introduces undershoot, time-delay and makes the control problem more challenging [7]. Alternatively, the flexibility of the structure may be ignored, and measurements from the actuator side are used in place of the end effector [3, 8]. However, by ignoring

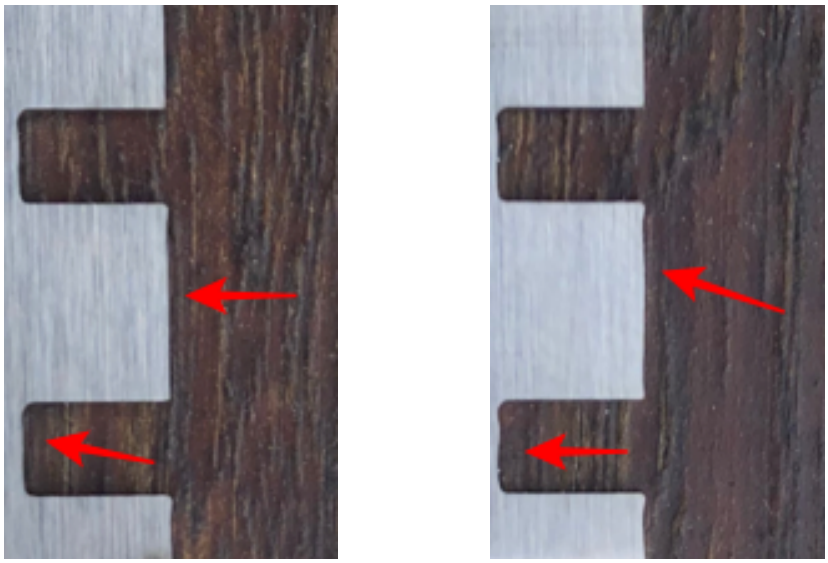

(a) (b)

Fig. 1.4: Laser cutting results in ANCA Motion where (b) is tuned based on the better motor-side performance than (a).

the structural flexibility and designing the controller based on motor-side performance cannot guarantee a desired performance from the end-effector side.

This phenomenon may be seen from the practical contouring application. In Fig. 1.4, the laser cutting results based on two tunings with the same cascaded control architecture of ANCA Motion are shown. In both cases, the controller tunings are conducted with the actuator-side position measurements. The tuning in Fig. 1.4b is to achieve better actuator-side tracking performance compared to Fig. 1.4a, however, more end effector oscillation occurs in Fig. 1.4b as highlighted by arrows. The tuning based on better motor-side tracking performance cannot guarantee a good machining outcome.

Furthermore, constraint handling - which refers to the consideration of states, input and output limitations - is essential in the design of industrial controllers. Failure to take account of the constraints can have a detrimental effect on machining performance and/or even damage the machine. Ultimately, it is desirable to explore the full potential of machines and respect the system constraints. Thus, it is favourable to consider the system constraints explicitly during controller design.

Another challenge is that disturbances on the actuator and load side can deteriorate

the trajectory tracking and contouring performance or make the system unstable, which demands consideration in controller design.

In summary, the properties such as structural flexibility, external disturbance, as well as non-collocated sensors and actuators position make the tracking and contouring problem challenging. The overall goal of this thesis is to achieve error-bounded tracking and contouring with the consideration of discussed challenges.

1.3 Thesis layout

The remainder of the thesis is described as follows. In Chapter 2, the source causing mechanical vibration and existing works on the trajectory tracking and contouring control are presented. The literature review considers different control algorithms under a uniform structure such that a clear understanding of existing research can be developed, with the consideration of the competing objectives including tracking performance, calibration effort and computational burden.

To provide researchers and practitioners with a direct insight into the limitation of existing trajectory tracking control algorithms and the trade-off between tracking performance and implementation effort, a commercial single-axis motor test bench is commissioned, and experiments based on major classes of tracking algorithms in Chapter 2 are conducted. The experimental set-up and tracking performance of different methods are analysed in Chapter 3.

In Chapter 4, a tracking error bounded model predictive control (MPC) method for machines with structural flexibility and external disturbance is presented. This is particularly relevant in applications when the end effector is connected to the drive via a flexible link, and no direct feedback measurement about the end effector position is available. To achieve this, a robust control invariant (RCI) set is estimated using the proposed computationally tractable algorithm and is incorporated into the problem formulation. The applicability of the proposed approach is successfully demonstrated via simulation and experiments.

In Chapter 5, the contouring error bounded control problem is considered. To develop the controller, we first introduce a high-fidelity model for the dual-drive gantry machine and identify its parameters using data from an industrial laser machine. The proposed tracking error bounded MPC is firstly extended to contouring error bounded control for biaxial systems based on a systematically reduced control-oriented model. Then, a less conservative contouring error bounded controller is proposed based on the explicit consideration of the calculated contouring error. The effectiveness of the proposed algorithms is demonstrated by experiments based on a designed back-to-back motor test bench.

Finally, the contributions of this thesis and potential further work are summarised in Chapter 6.

This page intentionally left blank.

Chapter 2

Literature review

ADVANCED manufacturing involves moving an end effector through a given trajectory to perform operations such as cutting, grinding and positioning. The quality of the resulting product is directly impacted by the ability of the machine to closely follow the desired trajectory.

Traditionally, the manipulators are built with high stiffness and are assumed to be as rigid in models used for controller synthesis. However, greater rigidity results in more weight. Consequently, larger and more costly motors are required to perform a given operation in a timely fashion [9]. Alternatively, using lighter (but more flexible) manipulators promises faster movements and more efficient utilisation of energy. However, the flexibility of the lightweight structure can lead to system vibration, which degrades the trajectory tracking performance [10] and may even lead to system instability [11].

To improve the trajectory tracking performance of systems with flexible linkages, a range of control methods have been proposed in the industrial motion control field. Furthermore, for industrial machines, the spatially separate location of actuator and end-effector leads to a non-minimum phase system which makes the tracking problem more challenging and highlights the need for control architectures that can compensate for such challenges in order to maintain or improve the product quality. The objective of this chapter is to conduct a literature survey of the state-of-art research in addressing these challenges.

The literature review starts with the discussion of mechanical vibration in feed drives and machines with flexible linkage. The efforts in modelling this vibration for controller

design purpose are presented. This is followed by a survey of existing trajectory tracking control algorithms in Section 2.2. For multi-axis application, the contouring performance is of more importance than the tracking performance of each axis. The contouring control schemes are those controllers designed based on direct calculated or estimated contouring error. The studies of contouring control are reviewed in Section 2.3. Finally, based on the literature review, the research aims of this thesis are proposed in Section 2.4.

2.1 Mechanical vibration in industrial machines

To achieve accurate tracking for references with high-frequency content, high closed-loop bandwidth is required when designing controllers [12]. Although the approach such as feedforward control can be used to extend the system bandwidth, the achievable bandwidth is often limited by the fundamental vibration modes. Thus, the effect of mechanical vibration on tracking and contouring performance should be considered when designing the motion controller.

Based on the assumption that the structure of the machine is fixed, the literature review here focuses on vibrations that can be compensated by the properly designed control laws.

2.1.1 Mechanical vibration in feed drives

To deliver the translational movement by a rotary motor, transmission parts such as rack and pinion, conveyor belt and ball screw are commonly used. However, the inherent structural flexibility of the transmission parts can cause mechanical vibration when the load moves, thereby deteriorating the tracking accuracy. In this subsection, the rotary motor with ball screw is taken as an example to show how the dynamics of feed drive with structural flexibility are considered for control purpose.

A diagram of a ball screw feed drive mechanical assembly is given in Fig. 2.1. For this type of feed drive, the mechanical vibration is caused by torsional flexibility at the motor

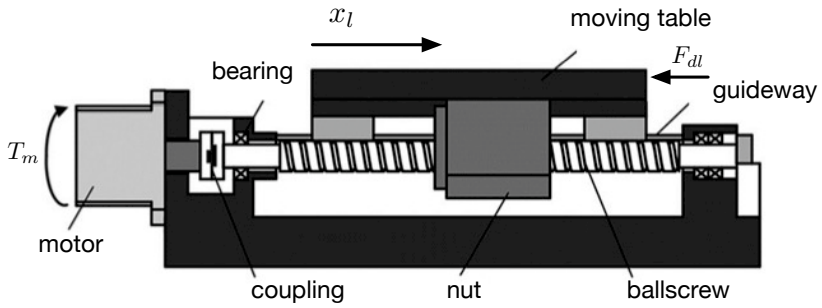

Fig. 2.1: Schematic diagram of a ball screw feed-drive assembly [12].

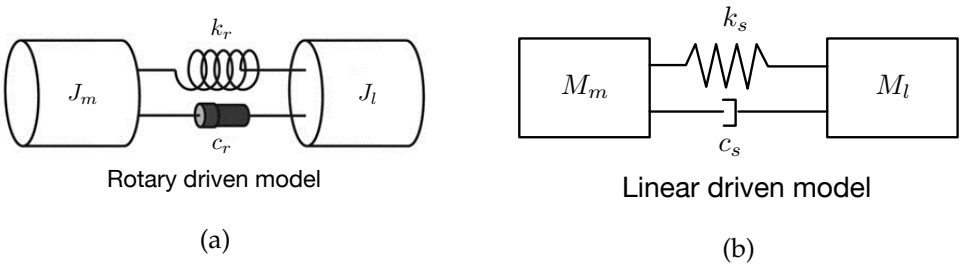

Fig. 2.2: Simplified model of ball screw drive: (a) rotary driven model; (b) linear driven model [15].

shaft-screw coupling, screw, and nut intersection [13, 14]. The inputs of this system include the equivalent force F_m from the rotary motor torque T_m and the disturbance force F_{dl} (e.g., cutting force) acting on the load. The outputs are the equivalent linear displacement of motor x_m, which is transformed from the angular displacement θ_m, and the linear displacement of the load x_l.

To describe the vibration and deformation in ball screw assembly, a multi-input multi-output model based on the mass-spring-damper structure is generally used [12, 15, 16]. In general, the flexible structure of a rotary motor with ball screw can be modelled either through an equivalent rotary-driven or direct-driven model with the linkage of spring and damper [15], as shown in Fig. 2.2. If linear-driven model is used, the system model can be expressed as,

$$\begin{bmatrix} x_m(s) \\ x_l(s) \end{bmatrix} = \begin{bmatrix} G_1(s) & G_{dm}(s) \\ G_2(s) & G_{dl}(s) \end{bmatrix} \begin{bmatrix} F_m(s) \\ F_{dl}(s) \end{bmatrix}, \tag{2.1}$$

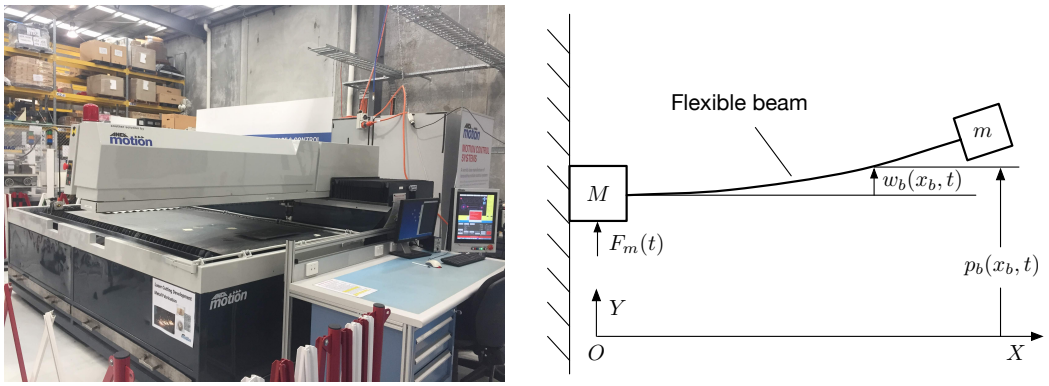

(a) (b)

Fig. 2.3: Industrial machine with cantilever beam structure: (a) cantilever laser machine in ANCA Motion; (b) simplified schematic diagram used in [10].

where $G_{dm}(s)$ and $G_{dl}(s)$ represent the transfer function from F_{dl} to x_m and x_l respectively, and $G_1(s)$, $G_2(s)$ stand for the transfer function from F_m to x_m and x_l with explicit form as

$$G_1(s) = \frac{1}{(M_m + M_l)s^2} \cdot \frac{M_l s^2 + c_s s + k_s}{M_p s^2 + c_s s + k_s}, \tag{2.2}$$

$$G_2(s) = \frac{1}{(M_m + M_l)s^2} \cdot \frac{c_s s + k_s}{M_p s^2 + c_s s + k_s}, \tag{2.3}$$

where $M_p \triangleq M_m M_l/(M_m + M_l)$; M_m is the equivalent mass of motor and M_l is the mass of load; k_s and c_s are the equivalent axial stiffness and damping coefficient.

2.1.2 Mechanical vibration in machines with flexible linkage

In addition to machines with flexible transmission part, mechanical oscillations are prevalent in industrial machines with flexible linkage.

For the industrial machine with one slide motor as shown in Fig. 2.3a, the long cantilever beam may oscillate around the point where the structure is extended. The simplified schematic diagram of this system is shown as Fig. 2.3b.

In [10], an Euler–Bernoulli beam model using truncated mode method is utilised to

represent the dynamics of a machine with cantilever beam structure as:

$$\left(\rho_l \int_0^{L_b} \varphi_1(x_b)dx_b + m\varphi_1(L_b)\right)\ddot{p}_b(t) + \ddot{q}_1(t) + 2\zeta_1 w_1 \dot{q}_1(t) + w_1^2 q_1(t) = 0,$$

$$(M + m + \rho_l L_b)\ddot{p}_b(t) + \left(\rho_l \int_0^{L_b} \varphi_1(x_b)dx_b + m\varphi_1(L_b)\right)\ddot{q}_1(t) = F_m(t) - b_l\dot{p}_b(t) - \delta_b(t),$$

$$w_b(x_b, t) = \varphi_1(x_b)q_1(t), \tag{2.4}$$

where the first vibration mode of beam deflection is considered; p_b is the position of the motor stage and $w_b(x_b, t)$ be the lateral displacement of the point with x_b distance to its base; L_b is the length of beam; ρ_l is the linear density of the beam inertia; $\varphi_1(x_b)$ and q_1 are the time-independent eigenfunction (modes shape function) and the generalised coordinate of the fundamental vibration mode, respectively; ζ_1 and w_1 are the corresponding damping ratio and frequency of oscillating mode; $F_m(t)$ stands for the electromagnetic force of the motor, and δ_b represents the lumped input disturbances and uncertainties.

Depending on the configuration of the machine with flexible beam, the clamped-free boundary conditions are used here to derive the eigenfunction $\varphi_1(x_b)$ as [17]:

$$\varphi_1(x_b) = \alpha_1 \left(\cosh\left(\frac{\beta_1}{L_b}x_b\right) - \cos\left(\frac{\beta_1}{L_b}x_b\right) - \frac{\cosh\beta_1 + \cos\beta_1}{\sinh\beta_1 + \sin\beta_1}\left(\sinh\left(\frac{\beta_1}{L_b}x_b\right) - \sin\left(\frac{\beta_1}{L_b}x_b\right)\right)\right),$$

where α_1 is a constant with β_1 being the positive solutions of

$$1 + \cosh\beta_1 \cos\beta_1 + \frac{m\beta_1}{\rho_l L_b}(\cos\beta_1 \sinh\beta_1 - \sin\beta_1 \cosh\beta_1) = 0.$$

The model (2.4) is then used for tip tracking of a linear-motor-driven flexible beam system. The simulation and experiment results show that the model with the consideration of fundamental vibration mode is sufficient for designing a tracking controller and ensuring the convergence of tracking error.

To reduce the detrimental vibration effect when the manipulator moves at high

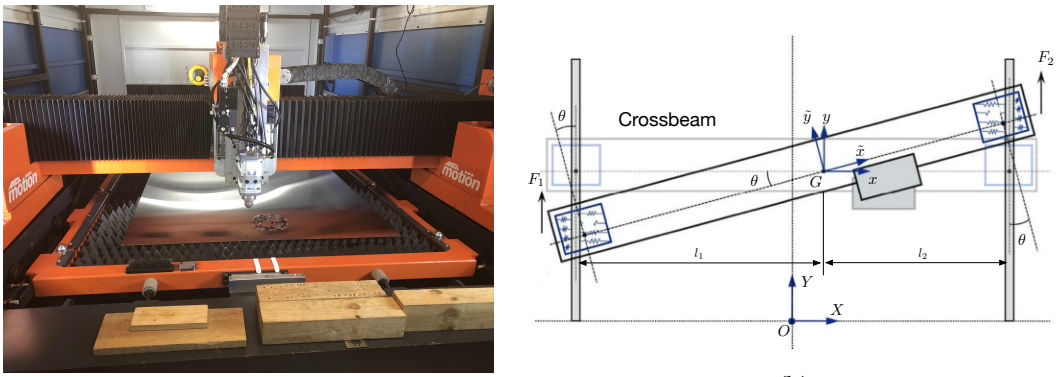

(a) (b)

Fig. 2.4: Mechanical resonance in dual-drive gantry machine: (a) gantry laser machine in ANCA Motion; (b) schematic diagram in [20].

speed, methods such as structure stiffness enhancement are used during the machine design. For instance, to increase the structural rigidities of biaxial machines, the gantry structure with two parallel drives is used, and the structure is shown as Fig. 2.4a.

However, the improvement of structural rigidity comes at the expense of increased machine cost by introducing another motor on the Y axis. Moreover, difficulties in maintaining complete synchronisation in movement along the parallel axes can cause deformation in the beam and lead to deteriorated accuracy of the end effector. This non-synchronised behaviour may arise due to the limited joint stiffness, different characteristics of the dual drives or the variational load distribution when load moving along the gantry [18, 19]. Consequently, some efforts have been devoted to modelling the dynamics of the dual-drive gantry machine, e.g. [19,20].

In [19], the Lagrangian equations are used to obtain the dynamics of the gantry system. However, the motion of gantry oscillation contradicts with the assumption that the crossbeam connection is rigid. To address the dynamics coupling issue, in [20], linear springs are introduced to approximate the effect of ball bearings between the motors and linear guides as shown in Fig. 2.4b. By neglecting the lateral dynamics, the model of the gantry system is simplified as:

$$M_t \ddot{y}_G = F_1 + F_2 - (b_1 + b_2)\,\dot{y}_G + (b_1 l_1 - b_2 l_2)\,\dot{\theta},$$

$$J_t\ddot{\theta} = -F_1 l_1 + F_2 l_2 + (b_1 l_1 - b_2 l_2)\,\dot{y}_G - \left(b_1 l_1^2 + b_2 l_2^2\right)\dot{\theta} - K_\theta \theta, \tag{2.5}$$

where the two generalised coordinates y_G and θ are the position of mass centre in the Y axis and the rotation angle formed between the coordinate frame Gxy and OXY respectively; M_t and J_t stand for, respectively, the mass and rotational inertia of the entire rigid body; F_1 and F_2 are the electromagnetic force generated by the motors on the parallel slides, b_1 and b_2 are the viscous friction coefficients; K_θ is the rotational stiffness.

Although the inclusion of linear springs justifies the lateral deformation when the rotational motion occurs, the lateral dynamics are neglected in [20]. Furthermore, the movement of the end effector along the perpendicular axis is ignored.

The lack of model accuracy necessitates the need for a system model that possesses position-dependent structural coupling characteristics.

2.1.3 Summary

The accuracy of the control-oriented model directly influences the performance of the motion controller, and thus impacting the manufacturing outcome. It has been shown in Section 2.1.1 and 2.1.2 that with the explicit consideration of the fundamental vibration mode in system dynamics, the control-oriented model is sufficient for designing the motion controller.

For biaxial machines with structural flexibility, the desire to improve the contouring accuracy motivates the proposition of system model with position-dependent structural coupling characteristics.

It should be noted that the effect of vibration is only reduced instead of eliminated by changing the machine structure from the cantilever beam to gantry configuration. Therefore, in addition to increasing the structural stiffness during the machine design, proper system modelling and controller design are essential to enhance tracking and/or contouring accuracy.

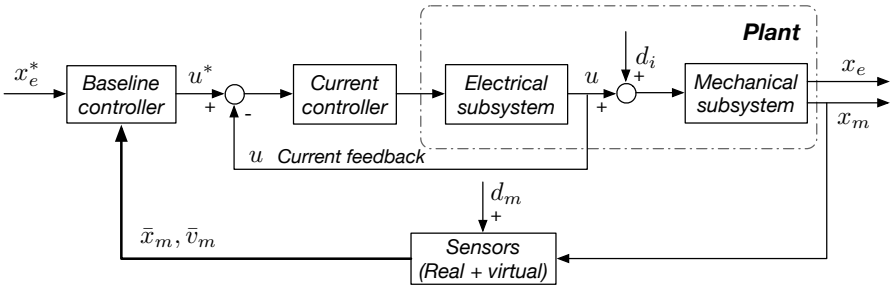

Fig. 2.5: Schematic diagram of industrial trajectory tracking control.

2.2 Trajectory tracking control algorithms

Let the actuator position x_m and end-effector position x_e be the system outputs, the motor current u be the input to the mechanical subsystem, the industrial trajectory tracking control architectures can be represented as Fig. 2.5. The electric drive control in current loop mainly involves the operation of power converter in different frames. Based on the assumption that the time scale of electrical subsystem is much faster than the mechanical subsystem in an industrial plant, the motion control investigated is related to the dynamics of the mechanical subsystem and the electric drive control in current loop is not the main focus of this thesis and is omitted. However, it has to be noticed that the performance of electric drive directly influences the performance of high-level position control and has drawn plenty of research interest [21].

In practical implementation, the current u contains the process disturbance d_i, and the motor position x_m and motor velocity v_m are contaminated by sensor noise d_m. Then the purpose of tracking control is to derive the current command u^* based on the desired position reference x_e^* and available feedback, e.g., the measured motor position $\bar{x}_m$ and motor velocity $\bar{v}_m$, such that end-effector of the machine can follow the reference in a desired pattern.

The existing trajectory tracking control approaches for mechanical subsystem can be grouped into three classes. The first class of algorithms do not utilise an explicit model of the system in the design process, and consist of variations on traditional proportional-integral-derivative (PID) approaches, H_∞ control and sliding mode control. The second class of algorithms use observers to estimate the disturbances in the system in order

to provide pre-emptive disturbance compensation in the control input. The final class considers explicit use of the system dynamics in the calculation of the control input, and are known as model-based approaches.

2.2.1 Non-model based feedback control

Non-model based feedback controllers do not utilise an explicit form of system dynamics in the controller design [22]. The low commissioning effort and relatively low computation load make non-model based feedback control easy for implementation in trajectory tracking applications, and these are highly utilised in industry implementations. The approach can be further divided into a number of categorisations.

PID-based cascaded control

Despite many advanced control algorithms being proposed for trajectory tracking, by far the most adopted controller in industrial settings is still the PID-based cascaded control [23]. The standard cascaded controller consists of three control loops, namely position, velocity and current loop from outside to inside. In the outermost loop, the position controller uses the error between the desired and measured position to generate the command for the velocity loop. In a similar way, the velocity controller in the middle loop uses the velocity difference to calculate the reference signal for the innermost current loop. For the innermost loop, the current error is used as the input to the current controller for generating the voltage required to drive the motor [24]. The core idea of cascaded control is to feedback intermediate variables that lie between the disturbance injection point and the output [25]. Note, however, the disturbances on each loop are effectively treated as constants that are rejected by the integral action of the corresponding controller.

Structural flexibility in the system can lead to high-frequency vibration and reduced tracking performance at the end effector side in industrial machines. The standard PID-based cascaded structure is not able to directly handle these types of disturbances,

and so many modifications to the structure have been considered.

Active approaches rely on additional sensing such as position and velocity of the end-effector side [26], and build this into the velocity feedback loop. In [27], a comparative study of various PI-based controller structures for the speed and current loops was conducted. The approaches considered additional feedback for vibration suppression in systems with a flexible connection, and theoretical and experimental results demonstrated that the resonant frequency could be shifted sufficiently to avoid speed oscillations in the closed-loop system. The primary disadvantage of this approach is the need for sensors at the end effector, which may be impractical from both a cost and placement perspective in practice.

Alternatively, the flexibility of the structure may be ignored and measurements of the motor are used in place of those of the end effector [3, 8]. In systems with some degree of flexibility, using the collocated control architecture to control the position of the end-effector leads to a non-minimum phase system which requires detuning the control gains.

Instead of using additional sensors and/or redesigning the mechanical hardware, 'passive' approaches intended to avoid vibration being initiated have been used widely in practice. These can involve command shaping, where the reference is modified to remove energy around the natural frequencies of the system. By doing so, the vibration modes of the system are not excited, thus reducing the residual vibration during the process [28, 29]. As one example, the input shaping in [30] involves convolving the desired command with a sequence of impulses, where the amplitude and time locations of the impulses are determined based on the natural frequencies and damping ratio of the system.

As another passive approach to deal with un-modelled dynamics online, Fig. 2.6 illustrates how filtering may be included in an industrial trajectory tracking application. Here the signal generated by the velocity controller is subjected to input shaping before serving as the current command. Note that without the filtering block, the structure demonstrated in Fig. 2.6 reduces to the standard cascaded controller. In [28], different

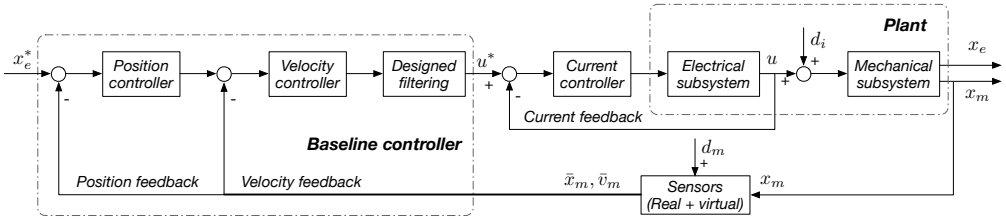

Fig. 2.6: Schematic diagram of cascaded control with filtering for trajectory tracking.

methods including low-pass and notch filters are described in detail, while the performance comparisons of filtering and input shaping schemes can be found in [29,31,32].

Due to the mechanical coupling between the motor and the end-effector, vibration at the end effector induces oscillations in the motor current and position. Consequently, the filtering schemes above indirectly target the end effector vibration, with the effectiveness being discussed in applications including ball screw drives [33–35] and servo drive systems [26,36,37].

In summary, the additional filtering augments the standard cascaded controller to increase the closed-loop bandwidth slightly. This is achieved by attenuating the detrimental frequency-domain effects of resonance and anti-resonance on the closed-loop transfer function through careful filter design. However, this approach does not target other sources of performance degradation arising from system nonlinearities and other time-varying or unmodelled dynamics.

Non-model based robust control approaches

The cascaded controller is designed based on the assumption that the different loops are separated in time scales so that independent controller design is possible. Using PI-variants on the loops is ideally suited for rejection of slowly varying disturbances (in the time scale inherent to the loop of interest). However, controller calibration that does not consider structural flexibility or changes due to variation in machine characteristics may lead to poor tracking in a given loop. This can then detrimentally impact on the performance of subsequent outer loops [38].

The desire to improve the robustness of the closed-loop system to these variations has seen proposed solutions including the controller calibration that explicitly considers parameter variation through tuning subject to constraints on gain margin or sensitivity [39, 40].

Other non-model based robust control methodologies such as H_∞ control have also been proposed [41]. The H_∞ control explicitly considers the robustness of the system; however, it requires more system information than the cascaded controller as the frequency spectrum of possible disturbances is required for control synthesis. Although the robustness and performance are considered during the H_∞ design process, the control performance of H_∞ is conservative, since the worst scenario of disturbance is considered, and there is always a compromise between the performance and robustness when a purely H_∞ controller is used [42].

Furthermore, the design of the controller is often complicated. To simplify the H_∞ control design, [43] proposed combining it with dynamic surface control. The authors applied the approach for reference tracking of an electrostatic micro-actuator with model uncertainty and external disturbances. Other applications of H_∞ control include [44], where the non-minimum phase nature of the system was dealt with by shaping the reference trajectory using a causal inversion approach. The combination was shown, via simulation of a one-link flexible manipulator, to avoid the destabilising effect of having the sensor and controller spatially disparate.

In addition to H_∞ control, other non-model-based robust control approaches that have been suggested widely include sliding mode control. This control technique is robust to model uncertainty and insensitive to parameter variation. Sliding mode control has been widely applied for trajectory tracking in applications including robot manipulators [45], mobile robots [46] and electrical feed drives [47]. The potential disadvantages of the technique include the possibility to induce chattering, and the need for a bounded disturbance model prior to controller development.

Implementation considerations

For the non-model-based algorithms discussed, the design of a controller does not rely heavily on the existence of an explicit plant model. In the case of the robust algorithms, an approximate linear model with some knowledge of plant variability is typically enough to design the controllers.

Achieving a high level of performance using this class of algorithms through gain tuning can be challenging. Often heuristic approaches are employed in practice to balance the competing needs of robustness and performance, although some effort has been devoted to systematically approaching this problem [48–50].

On the positive side, once designed, the algorithms are readily implemented at high computation rates due to the relative simplicity of the associated control calculations. This has allowed them to be deployed for decades in industrial tracking applications with relatively low computation resources (e.g. position loop sample rates as high as 26 kHz for PID and H_∞ were used as far back as 1998 [51]), or to increase the sampling rates to very high rates when more computational resources are available.

2.2.2 Disturbance estimation based feedback control

To compensate for the unknown disturbances arising from nonlinear effects including friction, disturbance-estimation based methods have been widely proposed. Although a direct position measurement from the end effector side is not generally available, vibration at the end effector induces oscillations in the motor current and position which can be measured. Whilst the filtering approaches of the previous section attempt to avoid excitation of vibrations, the disturbance estimation techniques instead try to actively compensate for any measured indications by modifying the current control input.

For disturbances that can be explicitly measured or modelled, feedforward and feedback linearisation have been proposed to attenuate or eliminate the effect of disturbances [52]. Implementation of these techniques is typically not undertaken in practice due to the difficulty and/or expense of the required direct measurements. Instead, different

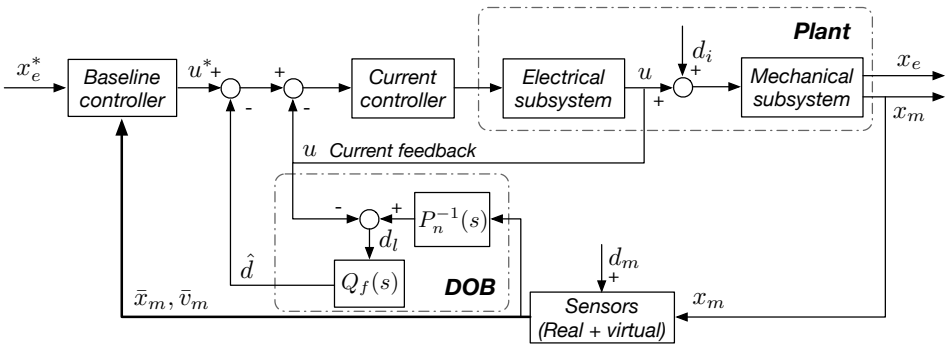

Fig. 2.7: Schematic diagram of DOB based reference tracking control scheme.

types of disturbance-estimation-based control (DEBC) methods have been proposed. These approaches have been shown to preserve the nominal performance of the baseline controller in the absence of disturbance [53], which is advantageous from a controller tuning perspective.

Whilst many types of disturbance estimator have been proposed in the literature, herein their key features are summarised with a focus on the disturbance observer (DOB) and extended state observer (ESO) methods.

Disturbance observer based control

The disturbance observer was first proposed in 1983 for estimating the load torque in the speed control of a DC motor [54], under an implicit assumption that the load torque is constant. Since then, modifications to the original disturbance observer have been designed to enable application in a range of systems requiring disturbance suppression. These include extending the algorithm for the position loop in servo-motors [55–60], applications in X-Y tables [61–63], robotic manipulators [64, 65] and grinding circuits [66]. An extensive review of disturbance estimation and attenuation techniques and their application in different domains was presented in [53], although a direct comparison with other trajectory tracking methods was not considered.

The fundamental idea of DOB can be illustrated as shown in Fig. 2.7, where d_l is the lumped disturbance, and $\hat{d}$ is the estimated lumped disturbance. If the mechanical

subsystem from current to motor position can be represented by the transfer function $P(s)$, the DOB consists of an inverse of the nominal model $P_n^{-1}(s)$ and a low-pass filter $Q_f(s)$. Under the assumption that the time scale of the current loop is much faster than mechanical loop (implying $u \to u^* - \hat{d}$), and the subsystem from current to motor position is minimum phase, the lumped disturbance reduces to

$$d_l(s) = (P_n^{-1}(s) - P^{-1}(s))x_m(s) + d_i(s) + P_n^{-1}(s)d_m(s). \tag{2.6}$$

Now, if the filter is designed to have $Q_f(s) \approx 1$ within the desired operating frequency range of the closed loop, then $\hat{d} = d_l$. By substitution of (2.6) into the equation $x_m(s) = (u(s) + d_i(s))P(s)$, the output of the system can be shown to be

$$x_m(s) = P_n(s)u^*(s) - d_m(s). \tag{2.7}$$

Hence, the impact of the load disturbance d_i has been suppressed from the output, x_m by the DOB.

The efficacy of the approach is clearly dependent on the linearity of the plant model, and subsequent design of the filter $Q_f(s)$. Furthermore, for machines with structural flexibility, (2.7) only deals with the position tracking of actuator instead of the end effector. There is no direct compensation for structural flexibility.

Extended state observer based control

The extended state observer (ESO) was first proposed in 1995 to estimate the lumped disturbance with incomplete information about the system dynamics [67]. Unlike many other methods, there is no reliance on linear plant assumptions. Typically, this observer is incorporated into the so-called active disturbance rejection control (ADRC) for reference tracking while reducing the effect caused by unknown disturbance [68].

ESO observers have been successfully deployed in many industrial applications, usually in conjunction with ADRC, including mechatronics servo systems [69–72], robotic

manipulators [73–75] and power converters [76–78] for disturbance estimation and rejection. In addition to experimental results, the ESO-based approaches have been commercialised for industrial usage in systems such as the SpinTAC^{TM} control software and motion control chip of Texas Instruments [79]. Nonetheless, despite the wide deployment of the approach, fundamental theoretical results for the broad class of ESO algorithms lagged until 2011 [80].

The structure of a typical ESO is reviewed in the following, under the assumption the mechanical system is considered as a rigid structure:

$$\begin{aligned} \dot{x}_m &= v_m, \\ \dot{v}_m &= \frac{k_t}{M_m} u + \frac{F_{dm}}{M_m}, \end{aligned} \tag{2.8}$$

where k_t and M_m are the values of force constant and actuator mass respectively; F_{dm} is the unknown disturbance on the motor. By taking the model mismatch and external disturbance as additional state ζ_m, the mechanical subsystem (2.8) may be rewritten as,

$$\begin{aligned} \dot{x}_m &= v_m, \\ \dot{v}_m &= \frac{k_t'}{M_m'} u + \zeta_m. \end{aligned} \tag{2.9}$$

Here k_t' and M_m' are the nominal values of the force constant and actuator mass respectively; and $\zeta_m = \left(\frac{k_t}{M_m} - \frac{k_t'}{M_e'} \right) u + \frac{F_{dm}}{M_m}$.

For a system in the form of (2.9), the ESO estimates ζ_m by introducing another state and applying error feedback on each stage as follows:

$$\begin{aligned} \dot{\hat{x}}_m &= \hat{v}_m + l_1 \Phi_1 \left(\tilde{x}_m \right), \\ \dot{\hat{v}}_m &= \frac{k_t'}{M_m'} u + l_2 \Phi_2 \left(\tilde{x}_m \right) + \hat{\zeta}_m, \\ \dot{\hat{\zeta}}_m &= l_3 \Phi_3 \left(\tilde{x}_m \right), \end{aligned} \tag{2.10}$$

Here $\hat{x}_m$, $\hat{v}_m$ and $\hat{\zeta}_m$ are the estimated value of x_m, v_m and ζ_m respectively; l_i is the gain of the observer to be chosen and $\Phi_i(\tilde{x}_m)$ is a function of estimation error with

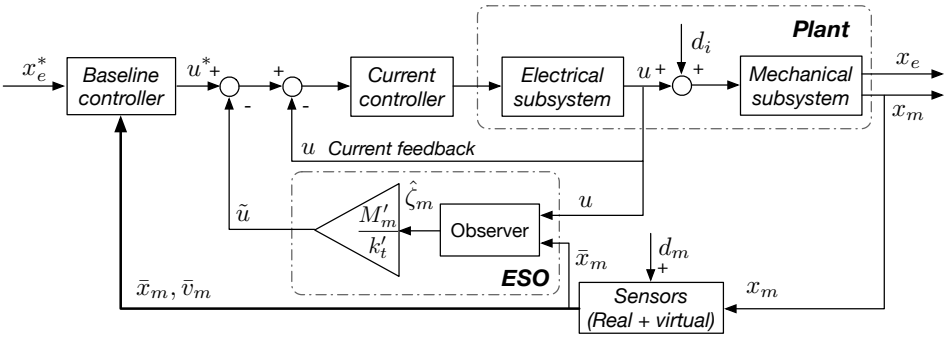

Fig. 2.8: Schematic diagram of ESO based reference tracking control scheme.

$\tilde{x}_m = \bar{x}_m - \hat{x}_m$ for $i = 1, 2, \cdots, n+1$, where n is the order of mechanical subsystem, which is chosen to be $n = 2$ here according to (2.9). The resulting structure of the ESO based reference tracking control scheme is shown in Fig. 2.8.

Whilst many different ESO implementations have been considered, they may be broadly categorised as belonging to either linear ESO (LESO) or nonlinear ESO (NLESO) based on the choice of function $\Phi_i(\cdot)$.

The convergence and stability analysis of LESO, where $\Phi_i(\tilde{x}_m) = \tilde{x}_m$, was first provided in [81] for an n-order single-input, single-output system with an integrator chain structure, under the assumption that all disturbances have bounded derivatives. Using the observer gain $l_i = \alpha_i \eta_o^{-i}$, where $\alpha_i = \frac{(n+1)!}{i!(n+1-i)!}$, $i = 1, 2, \cdots, n+1$, the bandwidth of the observer $1/\eta_o$ becomes the only tuning parameter in the observer design.

In the LESO case, if $\dot{\zeta}_m$ is bounded, there exists an estimation error bound and a finite time T such that the estimator error of each states $|\tilde{x}_i(t)| \leq \mathcal{O}\left(\eta_o^k\right), \forall t \geq T \geq 0$, $i = 1, \cdots, n+1$ for a positive integer k. This result was later extended to include bounds on either the disturbance or its derivative [82].

To apply the ESO to nonlinear estimators, [68] proposed specific heuristic structures for the nonlinear functions, $\Phi_i(\cdot)$. These NLESO algorithms have been widely used in many applications [71, 73, 75], although the nonlinear functions $\Phi_i(\cdot)$ were further generalised in [80], where it was shown that they need only satisfy a converse Lyapunov theorem property. Under this assumption, the observer gain can be chosen as $l_i = \eta_o^{n-i}$

for $i = 1, 2, \cdots, n+1$ and the estimation error on each state is bounded as $|\tilde{x}_i(t)| \leq \mathcal{O}\left(\eta_o^{n+2-i}\right)$ for all $t \geq T \geq 0$ and $i = 1, \cdots, n+1$. In practice, the NLESO errors are typically smaller than the corresponding errors observed using the LESO.

Implementation considerations

As an auxiliary control structure, the tuning of the disturbance estimation part should ensure that the convergence of disturbance estimation is much faster than the control loop where the observer located. For the disturbance observer based control, the selection of the nominal model P_n and the design of the Q_f-filter determine the estimation accuracy of DOB. For the LESO case, since the function of estimation error $\Phi_i(\tilde{x}_m)$ is fixed, the tuning is relatively straightforward compared to NLESO as the choice of function $\Phi_i(\tilde{x}_m)$ offers more degrees of freedom in the design of the observer.

By directly estimating and compensating for external disturbances, the approaches discussed in this subsection improve the robustness of the system. However, a potential drawback of high-gain observers is the propensity to introduce a peaking phenomenon in the estimation error [83]. This was observed for the NLESO applied to velocity control in [84] as an initial sharp spike in the response of state estimation may make the system unstable.

Furthermore, in a non-minimum phase system, applying disturbance attenuation from the motor side can lead to inferior end-effector tracking performance. This explains why the disturbance estimation based methods are generally applied in combination with other approaches such as command filtering in industrial implementations.

From the perspective of computation effort, the disturbance estimation part is essentially another low order state space model added to a baseline controller. As such, it does not significantly increase the computation load relative to the baseline controller.

2.2.3 Model based control

The class of model-based controllers (MBC) rely on knowledge of the plant dynamics to achieve trajectory tracking. Therefore, system modelling and identification are essential for MBC [85]. Depending on the type of control algorithm, models may also be required to capture uncertainty or disturbance levels in the control design.

In this section, we will distinguish between two types of model-based controllers on the basis of system constraints consideration - with the general class of unconstrained model-based controllers separated from those approaches explicitly encompassing constraints denoted model predictive control.

Unconstrained model-based control

Unconstrained model-based control covers a broad range of control architectures including state feedback control and linear quadratic (LQ) control for linear systems; through to Lyapunov-based control and feedback linearisation for nonlinear systems [85]. Many of these approaches have been applied to industrial trajectory tracking for machines with structural flexibility, as discussed below.

Pole-placement is a full state feedback control method that utilises a linear model of the mechanical system. For the cases where the dynamics of actuator and end-effector are involved, by defining the states as $\xi \triangleq (x_m, v_m, x_e, v_e)$ and discretising the plant, the control-oriented model of the mechanical subsystem may be represented in a general form:

$$\begin{aligned} \xi(k+1) &= A_d\xi(k) + B_d u(k) + E_d d_i(k), \\ \bar{y}_d(k) &= C_d\xi(k) + d_m(k), \end{aligned} \tag{2.11}$$

where v_e is the velocity of the end effector. Here, the output is the measured end-effector position, i.e., $\bar{y}_d \triangleq \bar{x}_e$. Assuming $d_i = d_m = 0$, the poles of the closed-loop system are assigned using $u = -K\xi$ based on transient performance requirements. In

[33], a pole-placement method was used to control the translational movement of a ball screw driven table. With the feedback measurement from both the rotary motor and table side, the poles related to the axial mode are assigned to speed up the decay of vibration. A similar pole-placement based active damping method was used for the speed control of a two-mass drive system in [27]. It has been shown that with measurement of either shaft torque or load speed as the additional feedback for control, the desired damping coefficient or the resonant frequency can be adjusted. However, a major disadvantage of this approach is that the pole-placement method requires full state feedback, thereby necessitating observer design. Without observers, the additional measurements are difficult to obtain in a production environment and are therefore not widely implemented. Even with observers, pole placement control does not explicitly account for state constraints, so that subsequent careful tuning is required, particularly in systems with nonlinearities, to ensure the control signals are within the achievable domain for the entire operating envelope.

Linear quadratic control is another state feedback control method that uses the plant model (2.11) but assumes the noise processes d_i and d_m are Gaussian with respective covariances. The controller gain, K_{LQ} is designed based on an offline optimisation of a specified cost function in the form:

$$K_{LQ} = \arg\min_{K} \mathbb{E}\left[\|\xi(k)\|_Q^2 + \|u(k)\|_R^2\right], \tag{2.12}$$

subject to (2.11) where $\mathbb{E}$ is the expectation. For systems with unmeasurable states and additional system noise, as the problem investigated in this paper, the optimal regulator is combined with an optimal state observer to produce a linear quadratic Gaussian (LQG) approach. To implement this approach, quasi-steady states ξ_d and inputs u_d are calculated from a reference, x_e^* as follows,

$$\begin{bmatrix} A_d - I_4 & B_d \\ C_d & 0 \end{bmatrix} \begin{bmatrix} \xi_d \\ u_d \end{bmatrix} = \begin{bmatrix} 0_{4,4} \\ x_e^* \end{bmatrix},$$

The estimated state $\hat{\xi}(k)$ is calculated based on a two-step process (measurement and

update with intermediate state ξ') according to:

$$\hat{\xi}(k) = \xi'(k) + L_{LQ}\left(\bar{y}_d(k) - C_d\xi'(k)\right),$$
$$\xi'(k+1) = A_d\hat{\xi}(k) + B_d u(k).$$

The controller gain K_{LQ} and observer gain L_{LQ} can be calculated analytically [86], leading to the control input $u(k) = -K_{LQ}(\hat{\xi}(k) - \xi_d(k)) + u_d(k)$.

Linear quadratic control has been used in applications including the tip positioning of a robot manipulator with flexible link [87] and speed control of an electric motor with flexible shaft [88]. The weightings of the cost function (2.12) are adjusted to achieve a desired control performance such as improving accuracy [89] or achieving energy minimisation [88]. The drawbacks of this approach include the number of tuning parameters for a nth-order system increasing from n in the pole placement case to $n^2 + 1$ for LQ. Furthermore, any nonlinearities in the system are not explicitly considered or compensated for, which may impact on potential tracking performance.

One approach to address this latter point involves using Lyapunov-based approaches that enable rigorous stability guarantees. The implementation of these approaches has been demonstrated in the position tracking control of a flexible-linked robot arm [90, 91] and position tracking of electric motors [92]. To further improve tracking performance in the presence of parameter variations or slowly varying disturbances, Lyapunov-based methods may be augmented with other control methods such as adaptive control or integral feedback, e.g. [92]. However, it is not trivial to find a Lyapunov candidate for designing this type of combined controller.

Instead of designing the controller based on the nonlinear dynamics of the system, feedback linearisation has been proposed to cancel out the nonlinearities in the system, enabling the deployment of algorithms for linear systems in the form of (2.11). For the tracking problem investigated in this paper, the feedback linearisation method has been utilised in numerous applications including decoupling the current and speed nonlinearities in electric drives [93] and cancelling out nonlinear dynamics of a flexible

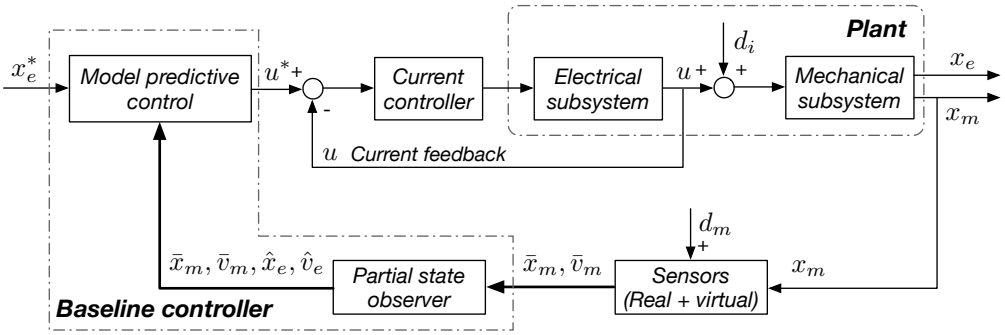

Fig. 2.9: Schematic diagram of MPC based reference tracking control scheme. Note that $\hat{x}_e$ and $\hat{v}_e$ stand for the estimated load position and velocity.

beam for tip position tracking [94]. However, the successful implementation of feedback linearisation requires exact cancellation of nonlinearities which may be challenging in real scenarios.

In summary, we can see although some decent trajectory tracking results have been demonstrated by unconstrained model-based control, none of the control methods above explicitly take account of input, output and states constraints, and are reliant on the accuracy of the plant model.

Model predictive control

Model predictive control (MPC) solves an online optimisation problem over a finite receding horizon with explicit consideration of system constraints [95]. Over the last 30 years, model predictive controllers have been gaining interest across a number of industrial domains as computational resources have advanced [96].

For systems with unmeasurable states, an observer is typically included leading to a control architecture as shown in Fig. 2.9. The MPC-based trajectory tracking problem involves solving the following constrained optimisation problem (where $\mathcal{X}$ and $\mathcal{U}$

represent the state and input constraint sets) at each sampling instant:

$$U^*(k) = \arg\min_{U(k)} \sum_{i=0}^{N-1} \left(\|\xi(i|k) - \xi_d(k)\|_Q^2 + \|u(i|k) - u_d(k)\|_R^2 \right) + \|\xi(N|k) - \xi_d(k)\|_P^2 \tag{2.13}$$

$$s.t.\ \xi(i+1|k) = A_d\xi(i|k) + B_d u(i|k), \tag{2.14}$$

$$\xi(i|k) \in \mathcal{X},\ u(i|k) \in \mathcal{U},\ i \in \mathbb{Z}_{[0,N-1]}, \tag{2.15}$$

$$\xi(0|k) = (\bar{x}_m(k), \bar{v}_m(k), \hat{x}_e(k), \hat{v}_e(k))\,. \tag{2.16}$$

Note that the solution returns the control trajectory $U^*(k) = [u^*(0|k), \ldots, u^*(N-1|k)]$, but only the first element $u^*(0|k)$ is imposed on plant. Ensuring the feasibility of the optimisation problem above, and the stability of the closed-loop system under control are two of the fundamental aspects of predictive control design.

An early contribution in the application of predictive control to motion control of feed drives was made in 1990 via a combination of cascade control structure with generalised predictive control (GPC) [97]. Although the idea of including system dynamics (2.14) and receding horizon with update (2.16) were shown in this early work, the state and input constraints (2.15) were not considered. Later, this initial work was extended to handle changing plant parameters such as variation of inertia [98], by updating the system model online based on observed errors.

To solve the tracking problem (2.13)-(2.16) with constraints while ensuring recursive feasibility of the open-loop optimisation problem, a command governor was introduced in [99] to modify the reference and ensure an admissible solution exists. Similar ideas were expanded in [100]. As an alternative, in [101] a dual-mode predictive control strategy is proposed where a feasibility recovery mode operates to recover feasibility should it be lost. These approaches were given a theoretical footing by introducing an artificial steady state and input as decision variables in the problem formulation (2.13), leading to a modified control algorithm with provable guarantees for piecewise constant reference tracking [102]. This was further extended to allow offset-free reference tracking with explicit consideration of disturbances in the system dynamics [103]. For applications

where periodical references are involved, the predictive repetitive control is proposed by incorporating the frequency information of reference within the structure of controller to enhance the tracking performance while ensuring the operational constraints [104, 105].

However, achieving asymptotically offset-free tracking for a disturbance-free system is not enough in many practical implementations. For applications such as laser cutting, it is highly desirable that the contouring error or the tracking error of each axis is within some desired tolerance. In [106], an error-bounded tracking controller is designed for a linear time invariant (LTI) system by modifying (2.15) such that the system states stay within a robust control invariant (RCI) set. The existence of the offline-computed RCI set indicates that the error bounds can be guaranteed for particular classes of reference and system with consideration of state and input constraints. However, the RCI set may not be finitely determined for systems with state disturbances [107–109], making it non-trivial to be computed for practical implementation.

Implementation considerations

Since model-based controllers are designed and implemented based on the system model dynamics, the accuracy of the model influences the control performance. This can be direct, through the reliance on the model in the generation of the control signals, or indirect in the case of approaches which remain robust to specified model inaccuracy. To achieve a good control performance typically requires effort to be spent on the system identification process.

For model-based controllers, the control performance in terms of accuracy is often reported to be superior to non-model based methods, which is not surprising as the knowledge of the system dynamics is used constructively in the controller. However, better performance always comes with a higher commissioning effort. For instance in LQ control described above, the tuning parameters in the matrices Q and R increase polynomially with the number of states and inputs; and these parameters may not be explicitly related to the time domain responses. This can lead to more challenging commissioning compared to non-model based schemes, especially when there is a lack

of systematic tuning criteria.

In terms of the embedded computation, the computational load of model-based control methods is generally higher than a comparable non-model-based controller. Methods such as pole-placement and an LQ-based controller are essentially control algorithms reliant on off-line computed state feedback gains, and so have a relatively low computational burden. In fixed-point microcontrollers, this may be increased if the feedback linearisation involves certain types of functions - e.g. exponentials.

On the other hand, the online solution of a constrained optimisation problem in MPC can be computationally challenging even for relatively straightforward system dynamics depending on the computational resource available. The growing interest in these algorithms is being driven by their potential capabilities in reference tracking and constraint satisfaction, yet the computation requirement of fast sample rate applications remains challenging. For those MPC variations with additional constraints, such as the error-bounded MPC mentioned above, an extra commissioning effort is required to compute the required disturbance sets, and the additional inequalities introduced may pose further challenges in terms of online computation on embedded industrial platforms.

2.3 Contouring control schemes

Although reducing the tracking error of the individual axis can ultimately improve the contouring performance, the contouring error does not necessarily rely on the tracking performance of each axis [110, 111]. This can be seen from the example demonstrated in Fig. 2.10 where the larger tracking errors in Case II result in a smaller contouring error compared to Case I.

As another way to improve the contouring control performance, contouring control schemes are discussed in this section. Different from the tracking control methods, contouring control schemes are controllers designed based on information from calculated or estimated contouring error.

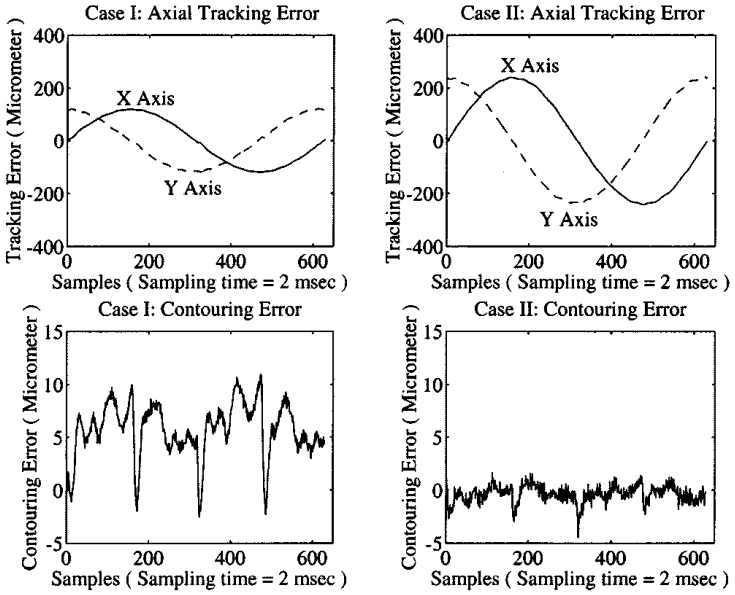

Fig. 2.10: Two case studies of tracking and contouring error [110].

2.3.1 Cross-coupled control with estimated contour error

In order to minimise contour error when a reference trajectory is given, the cross-coupled control (CCC) is proposed to correct the input command and force the axial tool position onto the path [112]. Fig. 2.11 shows the structure of the cross-coupled controller, where K_x and K_y are the gains for computing contouring error; the compensator W and cross-coupling gains C_x and C_y are related to the control law for correcting the reference. The variants of cross-coupled control are related to the choice of contour error model and the control law [113].

In the original CCC design [112], the corrective command is calculated from the weighted contour error and forwarded equally to axis controller, i.e., $C_x = C_y = 1$ with individual axis controllers unchanged. However, the constant compensator value and cross-coupling gains make the conventional CCC not effective in dealing with nonlinear contours and even lead to oscillation for linear contours when steady-state error tends to zero [114]. To deal with these drawbacks, a variable gain CCC approach was proposed in [113, 114], where the coupling gains C_x and C_y are state-dependent for nonlinear contour.

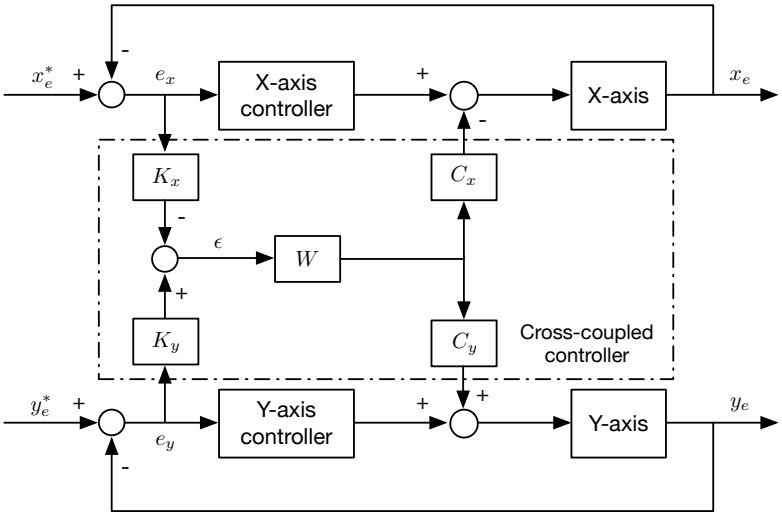

Fig. 2.11: The cross-coupled system block diagram.

Implementation consideration

The complexity of cross-coupled control highly depends on the choice of compensator W. Generally, a PID structure is used as the compensator, which makes the tuning of CCC similar to what described in Section 2.2.1. Without a systematic way of tuning, achieving high-performance contouring is non-trivial, and the trial and error method is involved.

However, on the other side, the expression of components in CCC is straightforward which means the designed control algorithm can be implemented at a high sampling rate. A higher sampling rate means a higher closed-loop bandwidth can be achieved, which is beneficial for tracking and contouring performance.

2.3.2 Coordinate transform based approach

Another category of contouring control method is based on the coordinate transformation where a decoupled contour controller is generally designed to minimise the contouring error. In [115], a tangential-contouring frame is proposed, and the controllers for minimising tangential and contour error are decoupled and designed separately based on the assumption that the dynamics of X- and Y- axis are close enough. Later,

this tangential-contouring frame is extended to Euclidean space and is formulated as the task coordinate frame [110].

The tangential-contouring frame simplifies the controller design by decoupling the tangential and contour dynamics [111]. Its application can be found in biaxial applications including robotics [116] and XY tables [117]. However, the difficulty in obtaining the coordinate transformation matrix for free-form contour and the assumption that the dynamics of two axes should be small limit the applicability of the tangential contouring control (TCC) method.

In addition to TCC, the polar coordinate is proposed in [118], and the contouring error is approximated by the radial error. Then the contouring control problem is reformed into a stabilisation problem by taking the contour error as a state variable. By integrating the feedback linearisation with the PID controller, the proposed coordinate frame is used for position tracking in single-axis positioning stage and XY position stage.

Implementation consideration

As an auxiliary method for minimising the contouring error, the complexity of the coordinate transformation is mainly influenced by the transformation matrix.

Moreover, for the tangential-contouring control, conditions such as the dynamics for X and Y axes should be similar cannot always be satisfied, which poses restriction on applicable systems.

2.3.3 Contour control with adaptive feed-rate

Although the contour control methods mentioned above have shown some improvements in contouring accuracy, interpolating the trajectory with higher feed-rate velocity can deteriorate the contour performance. This motivates the development of contour control methods with adaptive feed-rate.

For the biaxial contouring problem, the cross-coupled pre-compensation method

(CCPM) is thus developed to reduce the contour error by adding correction terms in the velocity command of the two axes [119]. The experiment results on the XY table shows a comparable contouring performance with CCC when tracking a linear contour and relatively better performance for circular contour.

Similar methods include the cross-coupling position command shaping controller (CPSCS) proposed in [120]. Different from the CCPM scheme, the CPSCS modifies the position command instead of velocity command based on the computed contour error and can be implemented on the CNC system or external computers.

To ensure system constraints while adjusting the feed-rate online, a model predictive contouring control (MPCC) method was proposed in [121] to deal with competing objectives, improving the contouring accuracy and minimising the traverse time. A virtual input for controlling the velocity of the reference is penalised with the approximated tangential and contouring error in the designed optimisation problem. The proposed method was compared with cascaded PI controller and MPC with pre-determined feed-rate on an XY table. Although the recursive feasibility of online optimisation cannot be guaranteed due to the competing objectives, the MPCC showed better performance in contouring accuracy with less traverse time.

Implementation considerations

Since the methods such as CCPM and CPSCS are proposed to modify the position and velocity command, they do not impose much additional computation burden on the baseline controller.

Conventionally, the MPC has a near cubic growth in computation time with respect to the number of system variables, i.e. $t_{MPC} = \mathcal{O}(n^3)$ where n is the order of the system. This means the computation load of MPCC increases non-linearly compared to the conventional model predictive control used for single-axis tracking. Furthermore, the decision variable that introduced for updating the velocity reference in MPCC adds more computation burden. The applicability of MPCC is highly limited by its computation time, and only 250 Hz sampling rate is achieved in [121].

2.4 Research aims

In summary, despite a considerable amount of research has been proposed in the motion control field, the PID-based cascaded control is still the most prevalent in the industry. With the ever-increasing demand on industrial manufacturing, there is a need to objectively assess the tracking control performance on an industrial platform to provide practitioners with the benefit and limitation of existing control algorithms. This motives the first research aim:

- Provide in-depth benefit and limitation of existing tracking control algorithms on single-axis platform.

This research aim is discussed in Chapter 3 where a test bench is built, and experiment results are presented.

For industrial contouring and machining applications, it is desirable the designed controller can guarantee bounded tracking and contouring errors without unduly compromising machine throughput. Although taking account of the structural flexibility in the control-oriented model can lead to improved trajectory tracking accuracy, achieving guaranteed tolerance on tracking error using existing control approaches, particularly in the presence of system disturbances, is not possible. This motivates the second research aim:

- Develop and validate a tracking error bounded control approach for industrial machines that has strict stability and feasibility guarantees.

The approach will utilise existing structures proposed in [106], but requires new techniques for computing RCI set in order to have guarantees on convergence. The developed approaches are presented and validated experimentally in Chapter 4.

In terms of applications involving multi-axis movement, the contouring error is of more importance than the tracking error. Thus, it is desirable to achieve contouring error bounded control. This motivates the following research aim as:

- Extend the tracking error bounded approach to multi-axis industrial contouring problems.

In this thesis, the biaxial movement is investigated. This research aim involves developing a model of biaxial industrial machine with the consideration of position-dependent structural flexibility. Two contouring error bounded controllers are presented and validated in Chapter 5.

This page intentionally left blank.

Chapter 3

Performance limitation of existing tracking control algorithms *

AS covered in the literature review part, although numerous control methods are proposed, the proportional-integral-derivative (PID) based cascaded control is still the most prevalent in the industry, due to a combination of factors including its relatively simple design and low implementation cost [23]. However, with the ever-increasing demands on industrial machining, there is a need to objectively assess when the benefits of advanced controller architectures might provide sufficient motivation to consider alternatives to the PID-based approaches.

For the one-dimensional system with structural flexibility and non-collocated output, there is also a lack of controller comparison based on a uniform platform to offer practitioners an insight into the limitation of existing tracking control algorithms. Therefore, it is the purpose of this chapter to present a performance comparison of existing control methods based on a design single-axis test bench.

This chapter starts with a general system description representing the one degree-of-freedom machines with a flexible manipulator and non-collocated output in Section 3.1. To quantitatively compare the tracking performance of different existing control algorithms under the uniform experiment setup, a test bench is designed and described in Section 3.2. The system identification of the test bench is described in Section 3.3. The experiment results of existing classes of tracking control algorithms are demonstrated and compared in the following Section 3.4. Conclusions are summarised in Section 3.5.

*Significant parts of this chapter will appear in *Control Engineering Practice.*

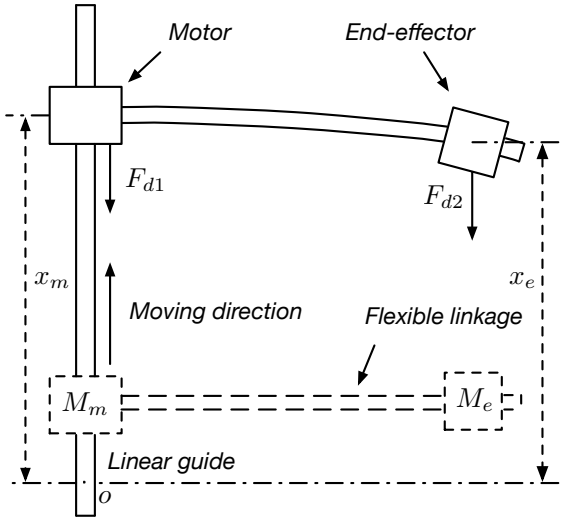

Fig. 3.1: Schematic diagram of investigated system with structural flexibility.

3.1 System description

For the one-degree of freedom system with structural flexibility, the schematic diagram can be represented as Fig. 3.1. This diagram shows two snapshots of the system, with the lower (dotted black line) indicating a steady state when the end effector position, x_e is equal to the motor position, x_m; and the upper (solid black line) indicating an orientation during dynamic behaviour $x_e \neq x_m$.

If first order approximations of the dynamics are modelled with all higher order modes relegated to part of the disturbance terms, the system can be represented by the following equations:

$$\begin{aligned} \dot{x}_m &= v_m, \\ \dot{v}_m &= \frac{1}{M_m}\left(k_t u - k_s\left(x_m - x_e\right) - c_s\left(v_m - v_e\right) - F_{d1}\right), \end{aligned} \tag{3.1}$$

$$\begin{aligned} \dot{x}_e &= v_e, \\ \dot{v}_e &= \frac{1}{M_e}\left(k_s\left(x_m - x_e\right) + c_s\left(v_m - v_e\right) - F_{d2}\right). \end{aligned} \tag{3.2}$$

Here $v_m \triangleq \dot{x}_m$ and $v_e \triangleq \dot{x}_e$ are the velocity of the motor and end-effector respectively; u represents the current to the motor; k_t is the equivalent force constant of the motor; k_s

and c_s are the equivalent spring constant and internal damping coefficient of the flexible mechanical components. In a lumped parameter approximation, M_m and M_e represent the equivalent mass of the motor and machine end; while F_{d1} and F_{d2} stand for the lumped disturbances on the motor and end-effector respectively, which may include influences arising from un-modelled dynamics or imperfect model parameters, as well as noise effects.

This control-oriented model structure has been used to describe many industrial applications including ball screw mechanisms [12, 33, 35, 122], conveyor belts [123] and two-mass drives with shaft elasticity [11, 124].

Furthermore, in many related works such as [125], it has been demonstrated this lumped parameter model (3.1), (3.2) can lead to effective trajectory tracking by the end effector in single-link flexible manipulator.

3.2 Experimental setup

To demonstrate the tracking performance of existing classes of control methods, a single-axis test bench representing the dynamics (3.1) and (3.2) is developed. The experimental setup is covered in this section.

The single-axis test bench consists of a linear motor and a flexible beam, where the end effector lies at the end of the beam furthest from the motor as shown in Fig. 3.2a. The LinX® M-series linear motor designed by ANCA Motion is used as the actuator, which is a permanent magnet synchronous tubular motor with high-precision position measurement. To quantitatively compare the trajectory tracking performance, another linear encoder is installed at the end of the beam to measure the end effector movement parallel to the motor base as shown in Fig. 3.2b. It has to be noticed that the measured end-effector position is not used in the controller design process and is only used for documenting experiment results.

In order to approximate the practical industrial situation where the dominant resonant frequency lies within the closed-loop bandwidth of general cascaded controllers,

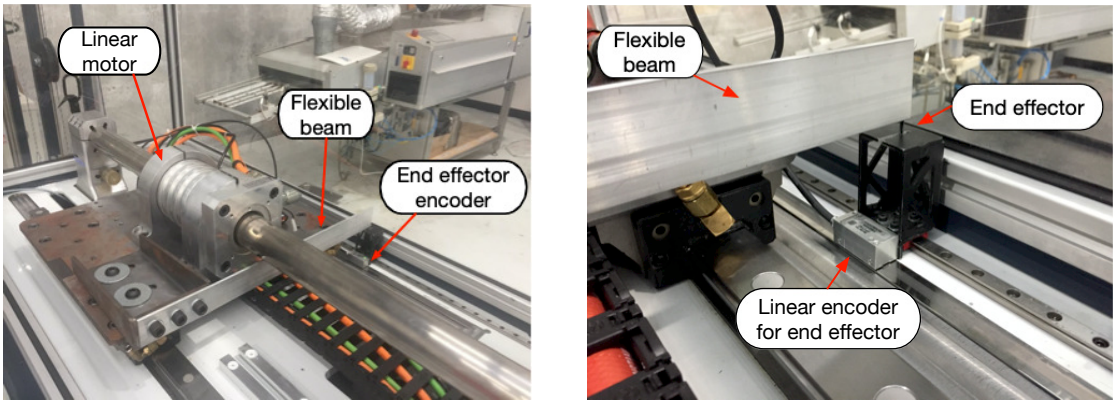

(a) (b)

Fig. 3.2: Designed test bench: (a) linear motor with stretched out flexible beam; (b) end effector measurement with linear encoder and designed bracket.

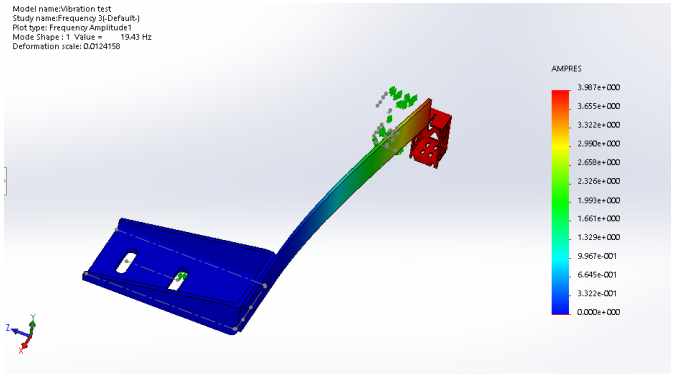

Fig. 3.3: Frequency analysis of the designed flexible manipulator.

the characteristics of the flexible beam and the structure for measuring end-effector position are carefully designed. For the aluminium beam used in this experiment, the Young's modulus and density are $E = 71 \times 10^9$ N/m^2 and $\rho_l = 2.7 \times 10^3$ kg/m^3. The beam is 350 mm long and comes with a rectangular cross-section with 40 mm width and 4 mm thickness. The frequency analysis, shown in Fig. 3.3, was conducted in SolidWorks to validate the designed vibration mode before the parts were sent for manufacturing.

To implement the real-time controller, Simulink Real-Time is used as the rapid prototyping system, and the compiled controller is downloaded onto an embedded target computer. The entire experiment setup is shown in Fig. 3.4. The communication rate between the target computer and test bench drive is 1 kHz, and the digital controller

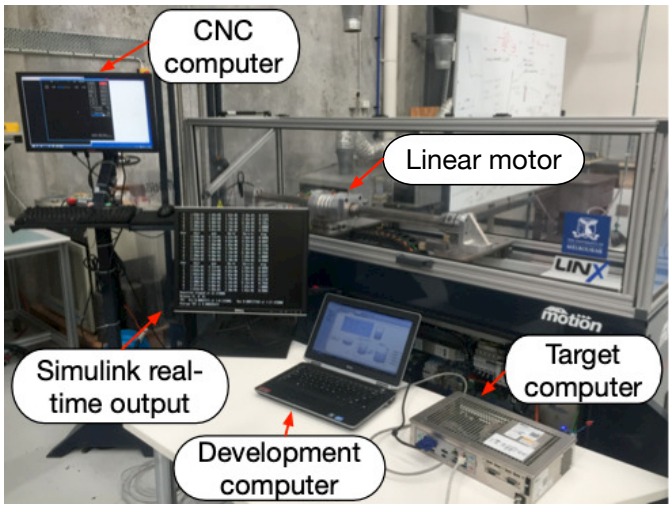

Fig. 3.4: Overview of experiment test bench.

updates at the same rate for all the investigated control algorithms.

3.3 System identification

For model-based control methods, the accuracy of the control-oriented model directly influences the performance of motion controllers. In this section, the electrical subsystem and nonlinear disturbance force in the mechanical subsystem are modelled. The parameters in electrical subsystem are identified first. Then, with the current loop controller implemented, the mechanical subsystem is identified with the closed current loop. The identified high-fidelity model is used for controller design purpose.

Electrical subsystem

The d-q (direct and quadrature axis) model is frequently used for the design of control algorithms in sinusoidally excited permanent magnet synchronous motors. By doing so, time-varying parameters are eliminated, and all variables are expressed in orthogonal or mutually decoupled d and q axes [126].

Here, the current equations of a general synchronous machine (with field excitation

circuit and damping circuit) are described first,

$$u_d = Ri_d + \frac{\partial \psi_d}{\partial t} - \omega_e \psi_q,$$

$$u_q = Ri_q + \frac{\partial \psi_q}{\partial t} + \omega_e \psi_d,$$

$$u_f = R_f i_f + \frac{\partial \psi_f}{\partial t},$$

$$0 = R_D i_D + \frac{\partial \psi_D}{\partial t},$$

$$0 = R_Q i_Q + \frac{\partial \psi_Q}{\partial t},$$

where u_d, u_q are the terminal voltage and i_d, i_q are the current in d and q axes respectively, R is the armature winding resistance, ω_e is the angular frequency of armature current. The field winding resistance R_f, field excitation current i_f, excitation circuit voltage u_f, only exist when electromagnetic excitation is used. The damper resistance in the d and q axes are represented by R_D and R_Q. The damper inductance in the d and q axes are L_D and L_Q respectively. The magnetic flux $\psi_d, \psi_q, \psi_f, \psi_D, \psi_Q$ in above equations are defined as

$$\psi_d = (\bar{L}_d + L_l)i_d + \bar{L}_d i_D + \psi_f = L_d i_d + \bar{L}_d i_D + \psi_f,$$

$$\psi_q = (\bar{L}_q + L_l)i_q + \bar{L}_q i_Q = L_q i_q + \bar{L}_q i_Q,$$

$$\psi_f = L_f i_f,$$

$$\psi_D = \bar{L}_d i_d + (\bar{L}_d + L_D)i_D + \psi_f,$$

$$\psi_Q = \bar{L}_q i_q + (\bar{L}_q + L_Q)i_Q,$$

where $L_d \triangleq \bar{L}_d + L_l$ and $L_q \triangleq \bar{L}_q + L_l$; $\bar{L}_d$ and $\bar{L}_q$ are armature self-inductance in d and q axes, L_l is the leakage inductance of armature winding per phase. It has to be noticed that flux linkage $\psi_f = L_f i_f$ only holds for motor with excitation field, where L_f is the maximum value of mutual inductance between the armature and field winding, and $\psi_f = \psi_{PM}$ is a constant for permanent magnet motor.

For the permanent magnet synchronous motor (PMSM) without damping winding, i.e., $i_D = i_Q = 0$, the governing equations of the current loop are:

$$u_d = Ri_d + \frac{\partial \psi_d}{\partial t} - \omega_e \psi_q = Ri_d + L_m \frac{\partial i_d}{\partial t} - \omega_e L_m i_q,$$

$$u_q = Ri_q + \frac{\partial \psi_q}{\partial t} + \omega_e \psi_d = Ri_q + L_m \frac{\partial i_q}{\partial t} + \omega_e L_m i_d + \omega_e \psi_{PM},$$

where $L_m \triangleq L_d = L_q$ holds for permanent synchronous motor. For the linear permanent magnet synchronous motor (LPMSM) used in the test bench, the dynamics of the electrical subsystem is:

$$u_d = Ri_d + L_m \frac{\partial i_d}{\partial t} - \frac{p\pi L_m}{\tau} v_m i_q, \tag{3.3}$$

$$u_q = Ri_q + L_m \frac{\partial i_q}{\partial t} + \frac{p\pi L_m}{\tau} v_m i_d + k_e v_m, \tag{3.4}$$

where the conversion $\omega_e = p\omega_m = p\pi v_m/\tau$ holds, v_m is the translational velocity of the motor, p is the number of pole pairs and τ is the pole pitch.

The linear least squares method is then used to identify parameters R, L_m and k_e based on

$$u_q = Ri_q + L_m \frac{\partial i_q}{\partial t} + k_e v_m,$$

where the back EMF constant $k_e \triangleq \frac{p\pi\psi_{PM}}{\tau}$ and the current in d axis is controlled to be 0 A. The armature winding resistance is identified as $R = 12.51\ \Omega$. The inductance and back EMF constant are identified as $L_m = 10.7$ mH and $k_e = 52.89$ Vs/m.

Mechanical subsystem

To get the expression of electromagnetic force in PMSM, we start with the power equation of a three-phase machine as,

$$\begin{aligned} P_{elm} &= \frac{3}{2}\omega_e(\psi_d i_q - \psi_q i_d) = \frac{3}{2}\omega_e\left((L_d i_d + \psi_{PM})i_q - L_q i_d i_q\right) \\ &= \frac{3}{2}\omega_e\left(\psi_{PM} + (L_d - L_q)i_d\right) i_q, \end{aligned} \tag{3.5}$$

With $L_d = L_q$ holds for the LPMSM, the electromagnetic force is given as,

$$F_m = \frac{P_{elm}}{v_s} = \frac{3}{2}\frac{p\pi\psi_{PM}}{\tau} i_q = k_t i_q, \tag{3.6}$$

where k_t is the force constant of motor with value $k_t = 79.33$ N/A inferred from the value of back EMF constant k_e.

The disturbance F_{d1} in (3.1) may include friction, cogging force and measurement noise. The cogging force and friction are identified as the disturbance force F_{d1} on the motor base, i.e. $F_{d1} \triangleq F_c + F_f$. Since no explicit models exist for F_{d2}, the nominal model used in simulation is $F_{d2} = 0$. Furthermore, the system identification requires identifying the motor and end effector mass, spring constant and internal damping coefficient.

The identification of friction and cogging force are separated by using the constant and frequency-dependent component of the applied force required to maintain a constant velocity.

The model of cogging force is adopted from [127]:

$$F_c(x_m) = \sum_{j=1}^{P} \left(S_{cj} \sin\left(\frac{2\pi j}{\tau} x_m\right) + C_{cj} \cos\left(\frac{2\pi j}{\tau} x_m\right)\right), \tag{3.7}$$

where P is a positive integer number, S_{cj} and C_{cj} are the coefficients before trigonometric functions. The reference velocity is set to a small positive value, and the input force is measured through current feedback. A fast Fourier transform of the measured force is then used to identify the frequency components of the cogging force, and subsequently can be correlated to the pole pitch and further used to identify the number of harmonics, P, required for (3.7).

The power spectral density of cogging force under constant velocity at 0.06 m/s is shown as Fig. 3.5. Using this technique, the pole pitch is identified as $\tau = 87.5$ mm based on the fundamental peak, and three harmonics are required to approximate the cogging force. Subsequently, the time series data of applied force can be used to identify the remaining model parameters of cogging force using a least squares approach, yielding

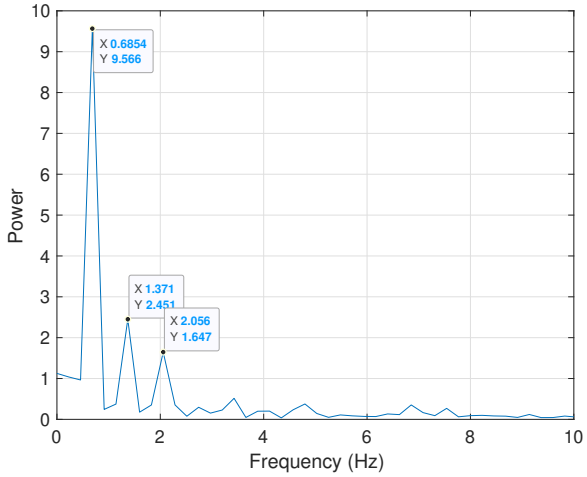

Fig. 3.5: Spectral analysis of cogging force under constant 0.06 m/s velocity.

$S_{c1} = 4.07$, $C_{c1} = 9.20$, $S_{c2} = 0.95$, $C_{c2} = -0.26$, $S_{c3} = -0.72$, $C_{c3} = 0.57$.

The friction model employed in simulations is based on the Lorentzian model of [128] employing the Karnopp remedy [129] to avoid simulation issues around zero velocity:

$$F_f(x_m, v_m, u) = \begin{cases} \left(f_c + b_v|v_m| + \dfrac{f_s}{1+\left(\frac{v_m}{v_s}\right)^2} \right) sgn(v_m) & |v_m| > \lambda \\ F_e & |v_m| \leq \lambda \\ & |F_e| \leq |f_c + f_s| \\ (f_s + f_c)\, sgn(F_e) & otherwise \end{cases} \tag{3.8}$$

where $sgn(\cdot)$ is the sign function; $F_e \triangleq (k_t u - F_c(x_m))$ is the externally imposed force. The system is run at different constant speeds and the constant offset in the applied force is correlated with the friction at that speed. A least squares method is then used to identify the parameters of (3.8) from the data across the speed range. Fig. 3.6 shows the comparison between the measured friction data and the value calculated based on friction model (3.8). For the test bench, this led to identified values of $f_c = 36.36$ N, $b_v = 250.9$ Ns/m, $f_s = 22.04$ N, $v_s = 2.82$ m/s and $\lambda = 10^{-6}$ m/s.

To identify the system parameters in (3.1) and (3.2), the motor runs at a constant

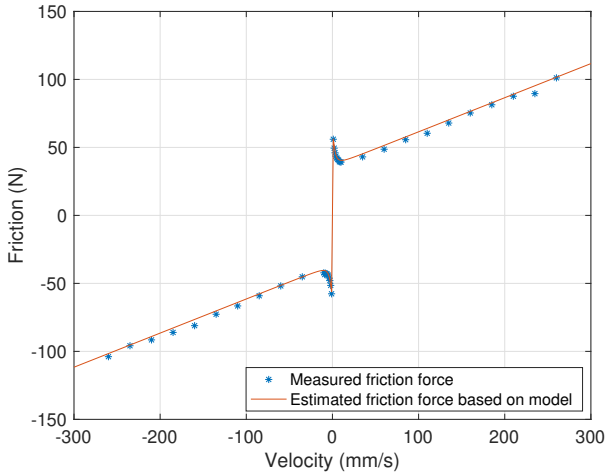

Fig. 3.6: Friction model fits with the measured friction force data.

acceleration, with the applied force measured and the disturbance force calculated from the model identified above. The total effective mass of motor and end-effector is subsequently identified as $M_e + M_m = 40$ kg, which is used to set a range of allowable solutions for each parameter.

Then a point-to-point movement is conducted on the test bench. By using the identified disturbance model to approximate F_{d1}, a constrained optimisation routine is then conducted to identify the values of M_m, M_e, k_s and c_s that minimise the difference between the transient simulated end effector trajectory and the trajectory collected from a point-to-point movement on the test bench, as shown in Fig. 3.7. The outcome of this optimisation was $M_e = 0.38$ kg, and $M_m = 39.62$ kg, whilst the spring constant and damping coefficient were identified as $k_s = 2908$ N/m, $c_s = 2.10$ Ns/m.

3.4 Performance comparison

In this section, the trajectory tracking performance of algorithms including standard cascaded controller, cascaded controller with notch filter and cascaded controller with LESO are demonstrated.

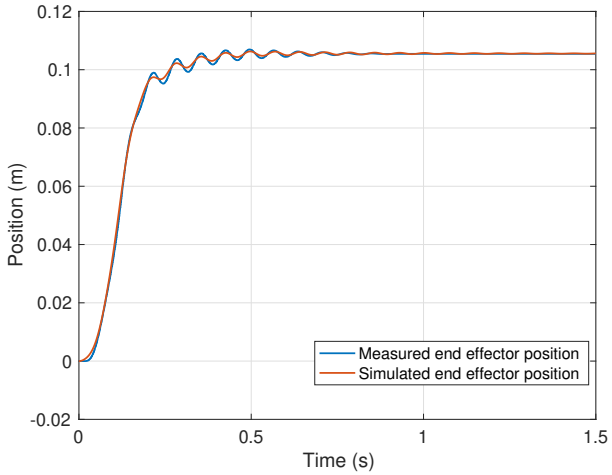

Fig. 3.7: Model validation based on the end-effector trajectory.

3.4.1 Desired trajectory

To evaluate the tracking performance of the above controllers, two widely used trajectory-tracking tasks were considered. In Task A, we require the load to conduct a point-to-point (PTP) movement for 0.1 m distance with maximum velocity 0.1 m/s and maximum acceleration 4 m/s^2. For Task B, a sinusoidal reference trajectory $x_e^*(t) = 0.05\cos(2t) + 0.05$ is used for reference tracking. A 0.1 s waiting time at the beginning of each trajectory is included in both references.

3.4.2 Tuning of the controllers

Throughout this work, in keeping with most production scenarios, it is assumed that the position measurement of end-effector is not available when designing the controllers and is only used to demonstrate the tracking performance.

The high-fidelity model identified in Section 3.3 is used to tune the gains of the cascaded controller, both without and with a notch filter to improve the actuator-side tracking accuracy. The cascaded controller consists of a P controller with proportional gain $k_{pp} = 30$ (1/s) as the position controller, a PI controller with proportional gain $k_{pv} = 55.67$ As/m, and time constant $T_{iv} = 0.04$ s as the velocity controller. The current

controller is implemented at the drive level and is not considered in the controller design due to its fast time scale. The instantaneous transfer function of the notch filter is given as

$$N_f(s) = \frac{s^2 + 2g\zeta\omega s + \omega^2}{s^2 + 2\zeta\omega s + \omega^2}, \tag{3.9}$$

where the gain of notch filter g and the damping ratio of the filter ζ are tuned to be 0.85 and 0.05. The value of the notch frequency ω is chosen as 87 rad/s to reduce the amplitude of the damped natural frequency present in the test bench.

For the cascaded controller with LESO, we used the same tuning parameters for the baseline cascaded controller and tuned the observer bandwidth $1/\eta_o$ as 700 rad/s to ensure a fast convergence of estimated states.

3.4.3 Trajectory tracking results

The actuator and load-side trajectory performance for the point-to-point (Task A) and sinusoidal (Task B) movement are demonstrated in Fig. 3.8 and Fig. 3.10, with the corresponding tracking error given in Fig. 3.9 and Fig. 3.11. In general, it can be seen that the flexible linkage amplifies the vibration at the end effector side relative to the motor oscillations. Anecdotally, this phenomenon is consistent with observations in production machines where good motor tracking can still result in poor tolerance at the end effector.

To quantitatively analyse the tracking performance of the tasks using the different controllers, a number of performance metrics are considered. As there is an implicit zero vibration assumption in most of the control architectures (i.e. the link between the end effector and the motor is assumed rigid), the difference between the motor position and the end effector reference $|x_m - x_e^*|$ indicates the typical error available for feedback in a production machine. The output quality is however better indicated by the error between the end effector and the reference, $|x_e - x_e^*|$.

The maximum deformation in the rigid link is calculated as $\|x_m - x_e\|_\infty$. This indicates the lateral vibration magnitude and internal stress on the mechanism, which

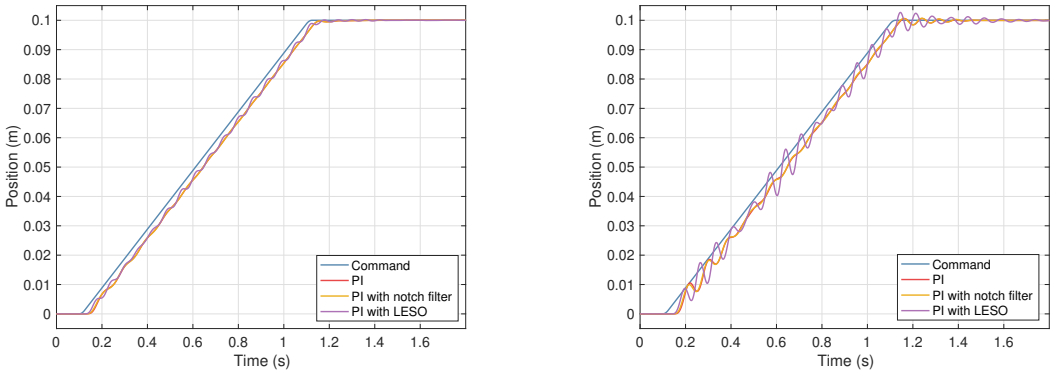

(a) (b)

Fig. 3.8: Point-to-point trajectory tracking based on different controllers: (a) motor position; (b) end-effector position.

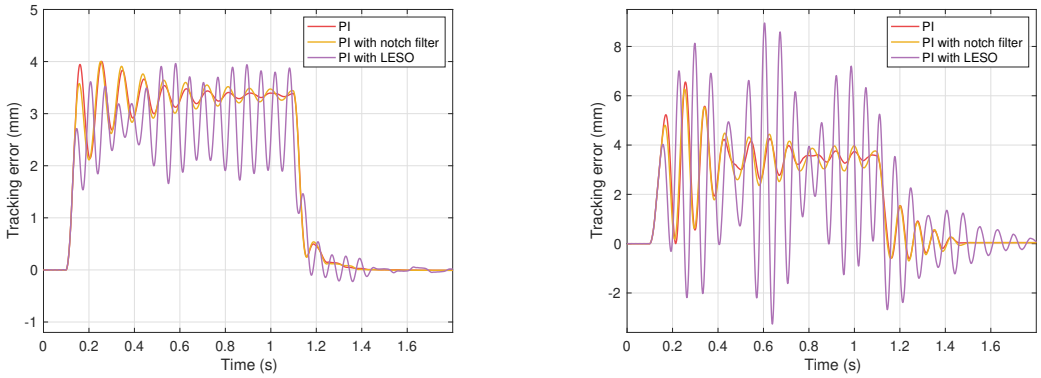

(a) (b)

Fig. 3.9: Point-to-point trajectory tracking error based on different controllers: (a) motor side error; (b) end-effector side error.

ideally should be kept low.

The mean absolute value of the current input is used as an indicator of the control effort, and the implementation cost is characterised by the average computation time per sampling period. These metrics are captured for the two tasks in Table 3.1 and 3.2.

If we first consider the tracking trajectory results for the cascaded PI structures, from Fig. 3.8 to Fig. 3.10, it can be seen that there is more vibration at the load side than the motor side. Quantitatively, the additional filter only provides marginal improvements in most performance metrics for two tasks, although the maximum deformation across

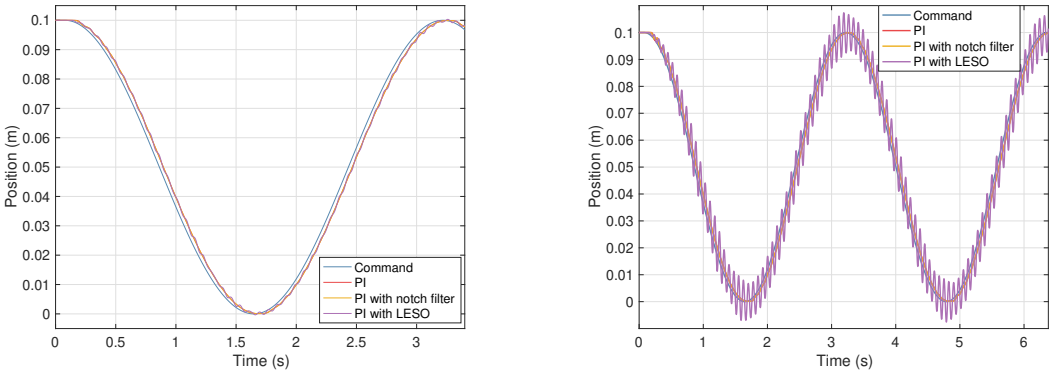

(a) (b)

Fig. 3.10: Sinusoidal tracking trajectory based on different controllers: (a) motor position; (b) end-effector position.

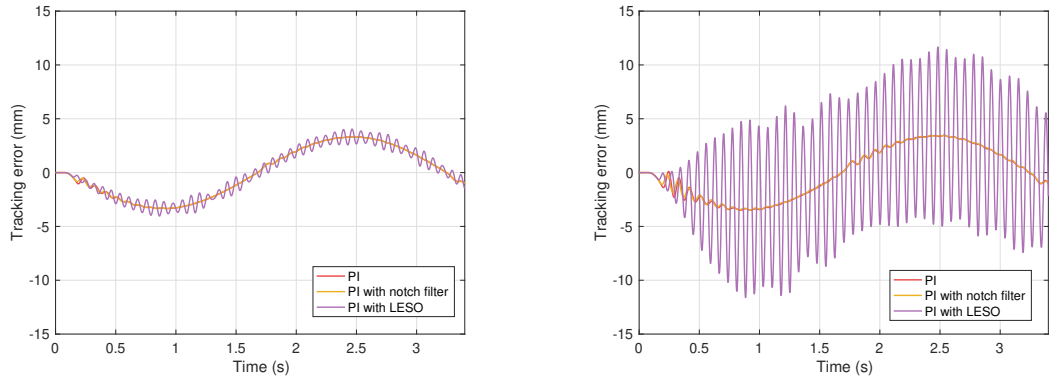

(a) (b)

Fig. 3.11: Sinusoidal tracking trajectory error based on different controllers: (a) motor side error; (b) end-effector side error.

the beam is reduced by approximately 11% in Task A and 33% in Task B.

If the cascaded PI is instead augmented with the LESO, the motor side performance is improved in terms of both the maximum and average tracking error aspect in Task A. However, the inclusion of LESO deteriorates the tracking accuracy in Task B for both actuator and end effector side as seen in Fig. 3.10 and Table. 3.2. This is again commonly observed in industrial applications where better actuator-side performance achieved may lead to a worse machining result. In practice, this leads to LESO often being combined with other augmentations (such as notch filtering) to provide improved

Table 3.1: Task A performance comparison

Controller	$\lvert x_m - x_e^* \rvert$ (mm)		$\lvert x_e - x_e^* \rvert$ (mm)		$\lvert x_m - x_e \rvert$ (mm)	Control effort	Computation time
	max	mean	max	mean	max	(A)	(ms)
Cascaded PI	4.002	1.603	6.556	1.722	2.556	0.744	0.026
Cascaded PI with filter	4.001	1.596	6.271	1.695	2.272	0.707	0.028
Cascaded PI with LESO	3.963	1.379	8.953	1.823	6.910	1.743	0.027

Table 3.2: Task B performance comparison

Controller	$\lvert x_m - x_e^* \rvert$ (mm)		$\lvert x_e - x_e^* \rvert$ (mm)		$\lvert x_m - x_e \rvert$ (mm)	Control effort	Computation time
	max	mean	max	mean	max	(A)	(ms)
Cascaded PI	3.358	1.975	3.552	2.053	0.830	0.595	0.0115
Cascaded PI with filter	3.344	1.968	3.535	2.043	0.551	0.553	0.0118
Cascaded PI with LESO	4.044	1.969	11.758	4.394	9.105	2.118	0.0117

tracking results with vibration attenuation.

3.5 Summary

Systems with features such as structural flexibility, non-collocated output and external disturbances are common in industrial applications, which makes the trajectory tracking problem challenging. The desire to improve manufacturing accuracy and throughput inspires the development of different control algorithms.

Based on the designed test bench, the performance and implementation cost of

existing tracking control methods are compared. Compared to the tracking error on the actuator side, the relative larger tracking error on the end-effector side shows the necessity of considering the structural flexibility when designing the controller. Ultimately, it is desirable to propose a controller for error bounded tracking of the end effector.

Chapter 4

Tracking error bounded control for machines with structural flexibility *

FOR industrial contouring and machining applications such as laser cutting, it is desirable to be able to bound errors without unduly compromising machine throughput. Traditional control architectures in machining are unable to explicitly bound tracking errors, and therefore conservative operation is required to ensure satisfactory performance of the overall system.

In this chapter, a model predictive approach is proposed that guarantees a desired level of tracking error is met for the case where the structure is flexible and the end-effector position is estimated. The system description and problem formulation are firstly described in Section 4.1. This is followed by the detailed control architecture and controller formulation presented in Section 4.2. To achieve the error bounded tracking, a robust control invariant (RCI) set is estimated using a computationally tractable algorithm and incorporated into the problem formulation. In Section 4.3, the applicability of the proposed approach is successfully demonstrated via simulation and experiments conducted on the commercial single-axis system described in Chapter 3. This chapter is ended with a summary in Section 4.4.

*Significant parts of this chapter is presented in *2019 IEEE International Conference on Industrial Technology* [130] and *IEEE Transactions on Industrial Electronics* [131].

4.1 System description and problem formulation

In Section 3.1, the two-degree-of-freedom model characterised by (3.1) and (3.2) is shown to represent systems with flexibility and nonlinear disturbance. In digital control, the dynamic equations (3.1) and (3.2) can be rewritten in the following discrete-time representation with sampling time T_s as:

$$\begin{aligned}
x_m(k+1) &= x_m(k) + T_s v_m(k), \\
v_m(k+1) &= v_m(k) + \frac{T_s}{M_m}\left(k_t u(k) - k_s\left(x_m(k) - x_e(k)\right) - c_s\left(v_m(k) - v_e(k)\right) - F_{d1}(k)\right), \\
x_e(k+1) &= x_e(k) + T_s v_e(k), \\
v_e(k+1) &= v_e(k) + \frac{T_s}{M_e}\left(k_s\left(x_m(k) - x_e(k)\right) + c_s\left(v_m(k) - v_e(k)\right) - F_{d2}(k)\right).
\end{aligned} \tag{4.1}$$

The mechanical system dynamics (4.1) can be written in state-space form with the viscous friction explicitly considered in the system matrices:

$$\xi(k+1) = A_d\xi(k) + B_d u(k) + E_d F_d(k), \tag{4.2}$$

$$y_d(k) = C_d\xi(k), \tag{4.3}$$

where the state vector is $\xi \triangleq (x_m, v_m, x_e, v_e)$ and y_d is the output; $F_d \triangleq (\delta, F_{d2})$ is the disturbance vector with $\delta \triangleq F_{d1} - b_v v_m$ and b_v is the viscous friction coefficient. The specific matrices of the LTI model (4.2) are given as:

$$A_d = \begin{bmatrix} 1 & T_s & 0 & 0 \\ -\frac{T_s k_s}{M_m} & 1 - \frac{T_s(c_s+b_v)}{M_m} & \frac{T_s k_s}{M_m} & \frac{T_s c_s}{M_m} \\ 0 & 0 & 1 & T_s \\ \frac{T_s k_s}{M_e} & \frac{T_s c_s}{M_e} & -\frac{T_s k_s}{M_e} & \frac{M_e - T_s c_s}{M_e} \end{bmatrix},$$

$$B_d = \begin{bmatrix} 0 \\ \frac{T_s k_t}{M_m} \\ 0 \\ 0 \end{bmatrix}, \; E_d = \begin{bmatrix} 0 & 0 \\ -\frac{T_s}{M_m} & 0 \\ 0 & 0 \\ 0 & -\frac{T_s}{M_e} \end{bmatrix}. \tag{4.4}$$

The state and input are assumed to belong to prescribed convex sets, and the external lumped disturbances are unknown and are assumed to be in closed and bounded sets, i.e.,

$$\xi \in \mathcal{X},\ u \in \mathcal{U},\ \delta \in \Delta,\ F_{d2} \in \mathcal{F}. \tag{4.5}$$

Here (A_d, B_d) is controllable. We assume (C_d, A_d) is observable and C_d has full row rank. Furthermore, to ensure error-bounded tracking, it is necessary to impose constraints on the reference that can be tracked. With this in mind, the reference is assumed to be generated by an external LTI system

$$\begin{aligned} r(k+1) &= A_r r(k) + B_r u_r(k), \\ y_r(k) &= C_r r(k), \end{aligned} \tag{4.6}$$

where $r \in \mathbb{R}^{n_r}$, $u_r \in \mathbb{R}^{m_r}$, $y_r \in \mathbb{R}$ are the state, input and output of the reference model, subject to the constraints,

$$r \in \mathcal{X}^r,\ u_r \in \mathcal{U}^r. \tag{4.7}$$

Moreover, it is considered that the reference is generated offline, and as such, a sufficient amount of preview of the reference trajectory (denoted N sampling instants) is available at each time step. Ultimately, it is desirable to ensure that the tracking error between the end effector and the reference is bounded by some constant value, ϵ_e, to ensure the tolerance of the machined part. This tracking error requirement can be represented as

$$\|y_r(k) - x_e(k)\|_\infty \leq \epsilon_e. \tag{4.8}$$

The complete problem of interest here is formalised as:

Problem 4.1. *Consider system* (4.2) *subject to* (4.5) *with reference generated by* (4.6) *satisfying* (4.7). *Given a desired tolerance* $\epsilon_e \in \mathbb{R}_+$ *and initial conditions satisfying* (4.5) *and* (4.8), *design a feedback control law* $u(k) = \kappa(\cdot)$, *such that the closed-loop system satisfies* (4.8) *for all* $k \in \mathbb{Z}_{0+}$.

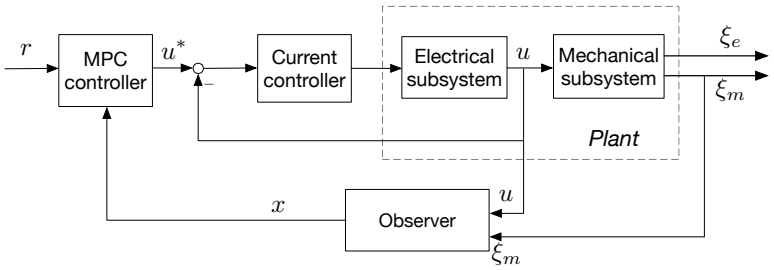

Fig. 4.1: Proposed control structure for error bounded tracking.

4.2 Proposed control architecture

Due to the presence of constraints, model predictive control is a good candidate to solve Problem 4.1. This typically involves solving an open-loop optimisation problem at each time step subject to constraints that reflect the system dynamics and operational constraints, without sacrificing feasibility of the optimisation problem at future time intervals.

In order to guarantee the recursive feasibility of the MPC problem, one approach is to ensure the system and reference states staying inside an RCI set [106]. For most industrial systems, it is hard or impossible to measure the position and velocity of the end effector. We seek to guarantee the error between the reference and estimated position in a tighter tolerance in order to bound the actual end-effector tracking error within the desired tolerance. An augmented system that incorporates the dynamics of estimated states is thus required for controller design.

In the subsequent subsections, the observer design and augmented system dynamics are described. For systems that the RCI set may not be finitely determined, the proposed off-line RCI set estimation approach is presented in detail, leading to the formulation of the MPC problem used to address Problem 4.1. The entire closed-loop structure is illustrated in Fig. 4.1. Since the time scale of the electrical subsystem is much faster than the mechanical subsystem, the design of the current controller is not considered.

4.2.1 Estimation of the end effector states

In general, the value of C_d depends on the measurable states of the system. Here, only the position and velocity of the motor are measurable.

Thus, the explicit expression of C_d is

$$C_d = \begin{bmatrix} 1 & 0 & 0 & 0 \\ 0 & 1 & 0 & 0 \end{bmatrix}.$$

The mechanical system dynamics (4.2) can be written in partitioned matrix form based on measured and unmeasured states as:

$$\xi(k+1) = \left[\begin{array}{c|c} A_{11} & A_{12} \\ \hline A_{21} & A_{22} \end{array}\right] \begin{bmatrix} \xi_m(k) \\ \xi_e(k) \end{bmatrix} + \left[\begin{array}{c} B_1 \\ \hline B_2 \end{array}\right] u(k) + \left[\begin{array}{c|c} E_1 & 0_{2,1} \\ \hline 0_{2,1} & E_2 \end{array}\right] \begin{bmatrix} \delta(k) \\ F_{d2}(k) \end{bmatrix},$$

where $\xi_m \triangleq (x_m, v_m)$, $\xi_e \triangleq (x_e, v_e)$. Let $\hat{\xi}_e \triangleq (\hat{x}_e, \hat{v}_e)$, where $\hat{x}_e$ and $\hat{v}_e$ are the estimated position and velocity of end effector respectively. A Luenberger observer with observer gain, L_r, for the unmeasured state can be formulated as

$$\hat{\xi}_e(k+1) = A_{22}\hat{\xi}_e(k) + A_{21}\xi_m(k) + B_2 u(k) + L_r(\xi_m(k+1) - A_{11}\xi_m(k) - B_1 u(k) - A_{12}\hat{\xi}_e(k)). \tag{4.9}$$

To avoid causality issues in calculating $\xi_m(k+1)$, an auxiliary variable $z \triangleq \hat{\xi}_e - L_r\xi_m$ can be introduced with dynamics as follows:

$$\begin{aligned} z(k+1) &= \hat{\xi}_e(k+1) - L_r\xi_m(k+1) \\ &= (A_{22} - L_rA_{12})\, z(k) + (B_2 - L_rB_1)\, u(k) \\ &\quad + ((A_{22} - L_rA_{12})\, L_r + A_{21} - L_rA_{11})\, \xi_m(k). \end{aligned} \tag{4.10}$$

The reduced-order estimation error can be defined as $\tilde{\xi}_e = \xi_e - \hat{\xi}_e$. The error dynamics are given by:

$$\tilde{\xi}_e(k+1) = (A_{22} - L_rA_{12})\, \tilde{\xi}_e(k) - L_rE_1\delta(k) + E_2F_{d2}(k). \tag{4.11}$$

The measured states ξ_m are then combined with the auxiliary variable to form an augmented state vector $x \triangleq (\xi_m, z)$. Denote the output of augmented system as $y \triangleq (\xi_m, \hat{\xi}_e)$, and the dynamics of this augmented system is given as follows:

$$\begin{aligned} x(k+1) &= \begin{bmatrix} A_{11} + A_{12}L_r & A_{12} \\ \Lambda L_r + A_{21} - L_r A_{11} & A_{22} - L_r A_{12} \end{bmatrix} x(k) \\ &\quad + \begin{bmatrix} B_1 \\ B_2 - L_r B_1 \end{bmatrix} u(k) + \begin{bmatrix} I_2 \\ 0_{2,2} \end{bmatrix} \Big(E_1 \delta(k) + A_{12} \tilde{\xi}_e(k) \Big) \\ &:= Ax(k) + Bu(k) + Ew(k) \\ y(k) &= Cx(k), \end{aligned} \tag{4.12}$$

where the matrix C can be inferred from the state x and output y; $\Lambda \triangleq (A_{22} - L_r A_{12})$; $w \triangleq E_1\delta + A_{12}\tilde{\xi}_e$ is considered as a combined disturbance. This lumped disturbance is assumed within a closed and bounded sets as $w \in \mathcal{W}$, where the range of set $\mathcal{W}$ can be identified. The observer gain L_r should be chosen to ensure the eigenvalues of Λ are inside the unit circle when designing the observer. In this paper, the gain of the partial state observer is chosen (after some tuning) to be:

$$L_r = \begin{bmatrix} 0 & 0.001 \\ 0 & 0.001 \end{bmatrix}.$$

From (4.11) it follows that given a positive constant, ϵ_o, there exists a positive pair of sets (Ω, Γ) such that for all $||\tilde{\xi}_e(0)||_\infty \in \Omega$ and $||\left(\delta(k), F_{d2}(k)\right)||_\infty \in \Gamma, \forall k \in \mathbb{Z}_{0+}$, the estimator maintains a bounded estimation error performance, i.e.,

$$\|x_e(k) - \hat{x}_e(k)\|_\infty \leq \epsilon_o, \; \forall k \in \mathbb{Z}_{0+}. \tag{4.13}$$

To ensure this infinity-norm bound can be satisfied in practice, it is necessary that the system must be started from a limited range of initial conditions - for example, the end effector is at rest and on the desired trajectory initially.

The control problem then becomes ensuring that for a given desired tracking error

tolerance, ϵ_e, the difference between the reference position and the estimated position of the end effector is bounded by $\|y_r(k) - \hat{x}_e(k)\|_\infty \leq \bar{\epsilon}_e = \epsilon_e - \epsilon_o$.

Remark 4.1. *In practice, the upper bounds of the estimation error ϵ_o is identified first. Then a desired tracking error bound ϵ_e is chosen to ensure $\epsilon_o \leq \epsilon_e$. If the estimation error is within an error bound $\|\hat{x}_e - x_e\|_\infty \leq \epsilon_o$ and the designed controller can guarantee $\|y_r - \hat{x}_e\|_\infty \leq \epsilon_e - \epsilon_o$, we can ensure the end effector tracking error is always within the desired error bound $\|y_r - x_e\|_\infty \leq \epsilon_e$. This inequality is based on the triangular inequality:*

$$\|y_r - x_e\|_\infty \leq \|y_r - \hat{x}_e\|_\infty + \|\hat{x}_e - x_e\|_\infty .$$

4.2.2 Estimation of the maximal robust control invariant set

The following three definitions are presented for completeness in the most general setting:

Definition 4.1. (RCI and maximal RCI sets) *Consider the system $x(k+1) = Ax(k) + Bu(k) + Ew(k)$, where $x \in \mathcal{X} \subseteq \mathbb{R}^n$, $u \in \mathcal{U} \subseteq \mathbb{R}^m$ and $w \in \mathcal{W} \subseteq \mathbb{R}^d$ are the state, input and disturbance vectors. The set $\mathcal{R} \subseteq \mathcal{X}$ is a RCI set if*

$$x(k) \in \mathcal{R}, \exists_{u \in \mathcal{U}}, Ax + Bu + Ew \in \mathcal{R}, \forall w \in \mathcal{W}, \forall k \in \mathbb{Z}_{0+}.$$

Furthermore, the set $\mathcal{R}$ is called a control invariant (CI) set if $w = 0$; the set $\mathcal{R}_\infty$ is the maximal RCI set if any $\mathcal{R} \subseteq \mathcal{R}_\infty$.

Definition 4.2. (Robust admissible input set) *The robust admissible input set of $\mathcal{R}$ is*

$$\Theta^u(x) = \{u \in \mathcal{U} | Ax + Bu + Ew \in \mathcal{R}, \forall w \in \mathcal{W}\}$$

Definition 4.3. (Pre-set) *The pre-set represents the set of states that can be robustly steered to a given set $\mathcal{Y} \in \mathbb{R}^n$ in one step under any possible disturbance $w \in \mathcal{W}$, and can be computed as*

$$D(\mathcal{Y}, \mathcal{W}) \triangleq \{x \in \mathbb{R}^n | \exists_{u \in \mathcal{U}}, Ax + Bu + Ew \in \mathcal{Y}, \forall w \in \mathcal{W}\} \tag{4.14}$$

Denote the maximal control invariant set of the reference by $\mathcal{R}^r_\infty$. We assume the reference is generated offline and stays within the set, i.e., $r(k) \in \mathcal{R}^r_\infty, \forall k \in \mathbb{Z}_{0+}$ by selecting $u_r(k) \in \Theta^{u_r}(r(k)) \subseteq \mathcal{U}^r$, where $\Theta^{u_r}(r_k)$ is the robust admissible input set of reference system. This guarantees the constraints in (4.7) are satisfied.

Having ensured the invariance of the reference, we now shift attention to ensuring $\|y_r - \hat{x}_e\|_\infty \leq \bar{\epsilon}_e$. We begin by defining an initial set of the system and admissible reference states:

$$\mathcal{S}^{x,r} = \{(x,r) \,|Cx \in \mathcal{X}, r \in \mathcal{R}^r_\infty, \|y_r - \hat{x}_e\|_\infty \leq \bar{\epsilon}_e\}\,.$$

At any time $k \in \mathbb{Z}_{0+}$ if $(x(k), r(k)) \in \mathcal{S}^{x,r}$, the system constraints are satisfied and the tracking error requirement is guaranteed. Consequently, the controller synthesis problem must ensure $(x(k+1), r(k+1)) \in \mathcal{S}^{x,r}$ for every admissible $r(k+1) \subseteq \mathcal{R}^r_\infty$. This requires a RCI set of the augmented system $\mathcal{R}^{x,r} \subseteq \mathcal{S}^{x,r}$, i.e.,

$$\begin{aligned}(x,r) \in \mathcal{R}^{x,r}, &\exists_{u \in \mathcal{U}}, (Ax + Bu + Ew, A_r r + B_r u_r) \in \mathcal{R}^{x,r}, \\ &\forall\,(w, u_r) \in (\mathcal{W}, \Theta^{u_r}(r))\,. \end{aligned} \tag{4.15}$$

One method of computing this RCI set $\mathcal{R}^{x,r}$ involves the iteration $\mathcal{R}_{i+1} = D(\mathcal{R}_i, (\mathcal{W} \times \Theta^{u_r}(r))) \cap \mathcal{R}_i$, where $\mathcal{R}_0 = \mathcal{S}^{x,r}$, until $\mathcal{R}_i = \mathcal{R}_{i+1}$ and $\mathcal{R}^{x,r} = \mathcal{R}^{x,r}_\infty = \mathcal{R}_i$. If this property can be satisfied, the maximal RCI set $\mathcal{R}^{x,r}_\infty$ is called finitely determined [109].

In [132], the maximal RCI set is computed as a union of polyhedra, which is non-convex and leads to the complexity in terms of convex elements growing exponentially with the number of iterations. In [106], an algorithm is proposed to compute a convex RCI set, but relies on the computation of the pre-set (4.14). The stopping criterion for the algorithm relies on either reaching a maximum number of iterations (i.e. no solution found) or the maximal set estimate being equal at successive iterations. This latter condition may be numerically difficult to be satisfied, and consequently we propose a

modification here based on an *estimate* of the pre-set using an inner approximation [109]:

$$\hat{D}\left(\mathcal{Y},\rho\right)=\left\{x\in\mathbb{R}^{n}|\,\exists_{u\in\mathcal{U}},Ax+Bu+Ew\subseteq\mathcal{Y}-\mathbb{B}^{n}(\rho),\ \forall w\in\mathcal{W}\right\}. \tag{4.16}$$

The parameter ρ in this equation is a tuning parameter that can be used to influence the conservativeness of the estimate; i.e., a larger ρ leads to a more conservative estimate of the pre-set [109]. The modified algorithm for estimating $\mathcal{R}^{x,r}$ is now given as follows:

Algorithm 1 RCI set computation for error bounded tracking

1: *Initialisation:*
2: $i\leftarrow 0$, $\mathcal{R}_0\leftarrow\mathcal{R}_s\cap\bar{\mathcal{R}}_0$, where
3: $\mathcal{R}_s\leftarrow\left(\mathbb{R}^n\times\mathcal{R}_\infty^r\right)$,
$\bar{\mathcal{R}}_0\leftarrow\left\{(x,r)\in\mathbb{R}^{n+n_r}|\,Cx\in\mathcal{X},\left\|y_r-\hat{x}_e\right\|_\infty\leq\bar{\epsilon}_e\right\}$.
4: *Iteration:*
5: $\mathcal{R}_{i+1}\leftarrow\mathcal{R}_s\cap\bar{\mathcal{R}}_{i+1}$, where
6: $\bar{\mathcal{R}}_{i+1}\leftarrow\hat{D}\left(\bar{\mathcal{R}}_i,\rho\right)\cap\bar{\mathcal{R}}_i$,

$$\hat{D}\left(\bar{\mathcal{R}}_i,\rho\right)\leftarrow\left\{(x,r)\in\mathbb{R}^{n+n_r}|\,\exists_{u\in\mathcal{U}},\,(Ax+Bu+Ew,A_rr+B_ru_r)\in\bar{\mathcal{R}}_i-\mathbb{B}^{n+n_r}(\rho),\right.$$
$$\left.\forall\,(w\times u_r)\in(\mathcal{W}\times\mathcal{U}^r)\right\}. \tag{4.17}$$

7: **if** $\mathcal{R}_i-\mathbb{B}^{n+n_r}(\rho)\subseteq\mathcal{R}_{i+1}$ **then**
8: **return** $\mathcal{R}^{x,r}\leftarrow\mathcal{R}_{i+1}$
9: **else**
10: $i\leftarrow i+1$
11: **go to** 4
12: **end if**

The inclusion of the ρ-radius ball in the stopping criterion ensures the computed $\mathcal{R}_{i+1}$ is an RCI set. The critical difference in the proposed algorithm here relates to the inclusion of the estimate, which enables a finite number of iterations to be employed. This is proven in the following theorem.

Theorem 4.1. *Given a prescribed tracking error bound $\bar{\epsilon}_e$ and a closed ball with radius ρ, Algorithm 1 terminates in finite steps. If the computed set $\mathcal{R}_{i+1}\neq\emptyset$, then $\mathcal{R}^{x,r}=\mathcal{R}_{i+1}\subseteq\mathcal{R}_\infty^{x,r}$ is a polyhedral RCI set for* (4.12) *and* (4.6) *subjected to input constraint, and robust to $w\in\mathcal{W}$ and $u_r\in\Theta^{u_r}(r)$.*

Proof. The proof includes two parts: showing the finite termination of computing RCI

set and the calculated $\mathcal{R}^{x,r}$ is a RCI set. Firstly the finite termination of the algorithm is shown. If $\mathcal{R}_i = \emptyset$, specifically $\mathcal{R}_s \cap \bar{\mathcal{R}}_i = \emptyset$, implies $\mathcal{R}_{i+1} = \mathcal{R}_s \cap \hat{D}\left(\bar{R}_i, \rho\right) \cap \bar{\mathcal{R}}_i = \emptyset$. Since $\emptyset \subseteq \emptyset$, for $i \in \mathbb{Z}_{0+}$ with $\mathcal{R}_i = \emptyset$ stop criterion holds.

If $\mathcal{R}_i \neq \emptyset$ for $i \in \mathbb{Z}_{0+}$, we assume maximal RCI set $\mathcal{R}_\infty^{x,r}$ exists. As in [109], we have $\mathcal{R}_\infty^{x,r} = \lim_{i\to\infty} \mathcal{R}_i$ and there exists $j \in \mathbb{Z}_{0+}$ such that $\mathcal{R}_i - \mathbb{B}^{n+n_r}(\rho) \subseteq \mathcal{R}_\infty^{x,r}, \forall i \geq j$. Thus $\mathcal{R}_i - \mathbb{B}^{n+n_r}(\rho) \subseteq \mathcal{R}_{i+1}$ holds since $\mathcal{R}_\infty^{x,r} \subseteq \mathcal{R}_{i+1}, \forall i \in \mathbb{Z}_{0+}$.

The proof of $\mathcal{R}_{i+1}$ is a RCI set is given as follows. Suppose $(x, r) \in \mathcal{R}_{i+1} = \mathcal{R}_s \cap \hat{D}\left(\bar{\mathcal{R}}_i, \rho\right) \cap \bar{\mathcal{R}}_i$, $\mathcal{R}_s \cap \hat{D}\left(\bar{\mathcal{R}}_i, \rho\right)$ can be rewritten as

$$\begin{aligned}\mathcal{R}_s \cap \hat{D}\left(\bar{\mathcal{R}}_i, \rho\right) = \big\{(x, r) \,|\, r \in \mathcal{R}_\infty^r, \exists_{u\in\mathcal{U}}, (Ax + Bu + Ew, A_r r + B_r u_r) \in \bar{\mathcal{R}}_i - \mathbb{B}^{n+n_r}(\rho),\\ \forall (w \times u_r) \in (\mathcal{W} \times \mathcal{U}^r)\big\}.\end{aligned} \tag{4.18}$$

Since the order of projection and intersection can be inverted considering $\mathcal{R}_s$ is independent of the projection variable u and $\mathcal{R}_i = \mathcal{R}_s \cap \bar{\mathcal{R}}_i$, (4.18) can be represented as

$$\begin{aligned}\mathcal{R}_s \cap \hat{D}\left(\bar{\mathcal{R}}_i, \rho\right) = \big\{(x, r) \,|\, \exists_{u_r\in\Theta^{u_r}(r)}, A_r r + B_r u_r \in \mathcal{R}_\infty^r,\\ \exists_{u\in\mathcal{U}}, (Ax + Bu + Ew, A_r r + B_r u_r) \in \mathcal{R}_i - \mathbb{B}^{n+n_r}(\rho),\\ \forall (w \times u_r) \in (\mathcal{W} \times \mathcal{U}^r)\big\}.\end{aligned} \tag{4.19}$$

Because $\mathcal{R}_i - \mathbb{B}^{n+n_r}(\rho) \subseteq \mathcal{R}_{i+1}$ according to stop criterion, (4.19) means there exists $u \in \mathcal{U}$ such that $(Ax + Bu + Ew, A_r r + B_r u_r) \in \mathcal{R}_i - \mathbb{B}^{n+n_r}(\rho) \subseteq \mathcal{R}_{i+1}$. This implies $(Ax + Bu + Ew, A_r r + B_r u_r) \in \mathcal{R}_{i+1}$, which shows R_{i+1} is a RCI set according to the Definition 4.1.

The property $\mathcal{R}^{x,r} \subseteq \mathcal{R}_\infty^{x,r}$ follows from the proof in [106], so the details are omitted here. The RCI set calculated based on Algorithm 1 is more conservative than the RCI set computed using $\bar{R}_{i+1} = D\left(\bar{\mathcal{R}}_i, (\mathcal{W} \times \mathcal{U}^r)\right) \cap \bar{R}_i$ since $\hat{D}\left(\bar{\mathcal{R}}_i, \rho\right) \subseteq D\left(\bar{\mathcal{R}}_i, (\mathcal{W} \times \mathcal{U}^r)\right)$. □

Now, assuming an RCI set has been estimated, the controller synthesis task requires ensuring that the system remains within this set at all times to guarantee the estimated end-effector position remains within the specified tolerance bound. The con-

troller should also consider minimising some performance objective, $J(x, r, u)$, whilst retaining the system within the RCI set and obeying the system dynamic constraints. If the performance measure is to be considered over multiple steps, it is clear that the reference trajectory must be available, i.e. at $k \in \mathbb{Z}_{0+}$, $N \in \mathbb{Z}_{+}$ step future reference $\gamma_k^N = (r(k), \cdots, r(k+N-1))$ is assumed known. One possible choice of performance objective is $J(\cdot) = Q_1 \left(y_r(k+i) - \hat{x}_e(i|k)\right)^2 + R_1 u^2(i|k)$, for $i \in \mathbb{Z}_{[0,N-1]}$, where Q_1 and R_1 are positive scalars which are used to emphasise weight on tracking performance and control effort respectively.

As discussed previously, model predictive control provides a systematic way of achieving these synthesis requirements, and the resulting controller, $\kappa(x(k), \gamma_k^N) := u^*(0|k)$, results from the solution of the online optimisation problem:

$$\begin{aligned} U^*(k) = &\arg\min_{U(k)} \sum_{i=0}^{N-1} J\left(x(i|k), r(k+i), u(i|k)\right) \\ s.t.\ \ & x(i+1|k) = Ax(i|k) + Bu(i|k), \\ & y_r(k+i) = C_r r(k+i), \\ & x(i|k) \in \mathcal{R}^{x,r}\left(x, r(k+i)\right), \forall i \in \mathbb{Z}_{[0,N-1]}, \\ & x(0|k) = x(k) \end{aligned} \tag{4.20}$$

where $U^*(k) = (u^*(0|k), \cdots, u^*(N-1|k))$. At each time instant, the optimal control $u(k) = u^*(0|k)$ is applied to the plant.

Remark 4.2. *The cost function used here $J(\cdot) = Q_1 \left(y_r(k+i) - \hat{x}_e(i|k)\right)^2 + R_1 u^2(i|k)$ is chosen as it aligns reasonably well with the overall control objective by penalising tracking error and control effort. Other choices, which consider control rate or terminal costs, are possible and may result in different closed-loop responses. These alternative cost functions are not investigated here but are readily accommodated in the proposed approach. Similarly, for a given R_1 matrix, the magnitude of the elements of Q_1 will have an effect on the closed-loop response, with larger Q_1 typically resulting in smaller maximum tracking error at the cost of increased vibrations observed in the end effector along the reference trajectory.*

Remark 4.3. *Robustness is directly handled through the guarantees that the controller maintains*

the system states within the RCI set $x(i|k) \in \mathcal{R}^{x,r}\,(x, r(k+i))$. At the time of computing the RCI set, the influence of any unknown disturbance within a disturbance set, $\mathcal{W}$, is considered during the iteration process. Following calculation of the RCI set, provided the feasibility of MPC is satisfied initially, the recursive feasibility of the MPC problem can be guaranteed and all state and input constraints will be satisfied in the future, i.e. robustness to any disturbance in $\mathcal{W}$ is provided.

4.3 Effectiveness demonstration

To validate the effectiveness of the proposed algorithm, the point-to-point trajectory tracking is firstly conducted in high-fidelity simulation with the model identified in Section 3.3. Then the same test bench described in Section 3.2 is used for experimental trajectory tracking based on the proposed algorithm and cascaded PI controller.

4.3.1 Disturbance set identification

In addition to the parameters identified in Section 3.3, the lumped disturbance set, $\mathcal{W}$ in (4.12), requires identification. To identify $\mathcal{W}$, a library of representative tracking trajectories is defined. The difference between the measured and modelled motor velocities is then collected over the complete set of trajectories, leading to the population of the disturbance set. To allow for potentially unconsidered references being used, the size of the set is increased by a safety factor of 25%. For the plant of interest and its identified model, this led to a disturbance range of $\bar{w} \in [-5, 5]$ mm/s for $w \triangleq [0, \bar{w}]^T$.

4.3.2 Simulation results and comparison

In this section, we desire the end effector to track a reference trajectory with a tracking error bound $\epsilon_e = 5$ mm. The reference trajectory is described as $r \triangleq (y_r, v_r)$, where y_r and v_r are the desired position and velocity of the end effector. The reference is generated from a double-integrator model whilst considering position and velocity constraints;

i.e., $(0, -0.1) \leq r(t) \leq (0.1, 0.1)$ [m, m/s]. Acceleration is the input to the model, u_r and is subject to the constraint $-4 \leq u_r(t) \leq 4$ [m/s^2]. The LTI model of the reference (4.6) prior to constraint consideration, is given as follows:

$$\begin{aligned} r(k+1) &= \begin{bmatrix} 1 & T_s \\ 0 & 1 \end{bmatrix} r(k) + \begin{bmatrix} 0 \\ T_s \end{bmatrix} u_r(k), \\ y_r(k) &= \begin{bmatrix} 1 & 0 \end{bmatrix} r(k). \end{aligned} \tag{4.21}$$

The state and input constraints of the system are:

$$\begin{aligned} -[5,\ 10,\ 5,\ 10]^T \leq (\xi_m, \hat{\xi}_e) \times 10^2 \leq [15,\ 10,\ 15,\ 10]^T, \\ -9 \leq u \leq 9. \end{aligned}$$

Yalmip [133] and MPT3 [134] are used to estimate the pre-set, $\hat{D}(\cdot)$ in (4.16). The RCI set is subsequently calculated using Algorithm 1, with the tracking error bound considered to be $\|y_r - \hat{x}_e\|_\infty \leq \bar{\epsilon}_e = 4.5$ mm considering the upper bound of estimation error is identified as $\epsilon_o = 0.5$ mm.

Proposed controller vs standard MPC

With the RCI set established, the proposed MPC problem can now be explicitly formulated. The cost function solved at each time step, (4.20), uses $J = (y_r(k+i) - \hat{x}_e(i|k))^2 + 5 \times 10^{-5} u^2(i|k)$ to emphasise tracking accuracy over control effort.

Fig. 4.2 illustrates the simulated tracking performance of the proposed controller following a point-to-point movement reference with 4 m/s^2 maximum acceleration and 0.2 s zero position waiting time. It shows that the end-effector position stays inside the error bound during the whole process.

As an initial comparison, we consider a standard tracking MPC with terminal cost

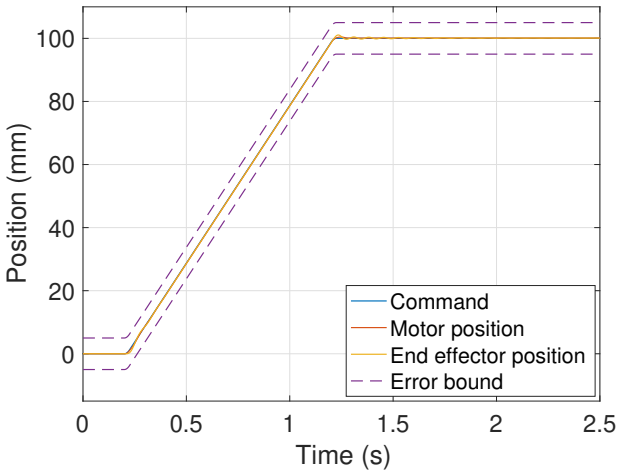

Fig. 4.2: Trajectory of simulated point-to-point tracking of proposed controller with $Q_1 = 1, R_1 = 5 \times 10^{-5}$.

[103] where the controller solves the following optimisation at each sampling instant:

$$
\begin{aligned}
U^*_{mpc}(k) = \arg \min_{U_{mpc}(k)} & \sum_{i=0}^{N-1} \Big(\|y(i|k) - y^*(k+i)\|^2_{Q_1} + R_1 u^2(i|k) \Big) \\
& + \|y(N|k) - y^*(k+N)\|^2_{P_1} \\
s.t. \;\; & x(i+1|k) = Ax(i|k) + Bu(i|k), \quad y(i|k) = Cx(i|k), \\
& u(i|k) \in \mathcal{U}, \; i \in \mathbb{Z}_{[0,N-1]}, \\
& y(i|k) \in \mathcal{X}, \; i \in \mathbb{Z}_{[1,N]}, \\
& x(0|k) = x(k)
\end{aligned}
$$

Here $\|x\|^2_{Q_1} = x^T Q_1 x$ and $y^* \triangleq (r, r)$ is the full state reference. The first element of U^*_{mpc} is applied to the plant. For fair comparison, the tuning weights of standard MPC are chosen as $Q_1 = diag(0, 0, 1, 0), R_1 = 5 \times 10^{-5}$ and P_1 solved according to the discrete-time algebraic Riccati equation.

The tracking error of the proposed controller and standard MPC are illustrated in Fig. 4.3. It can be seen that the tracking error of the standard MPC violates the 5 mm error constraint, primarily due to the control-oriented model not capturing all dynamics. Retuning the standard tracking controller may lead to constraint satisfaction on this

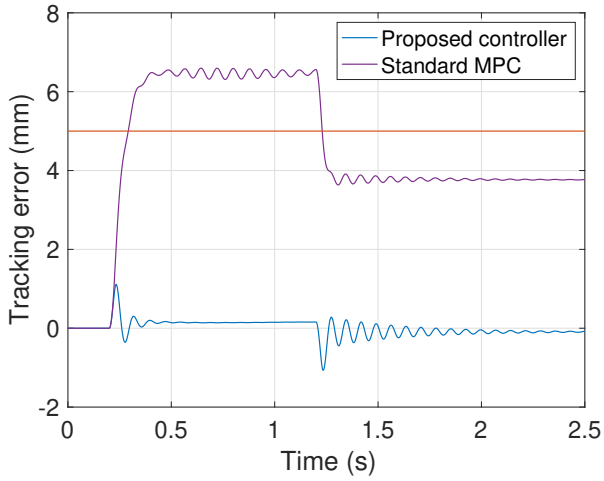

Fig. 4.3: Simulated end-effector tracking error by using proposed controller and standard MPC.

particular reference but is not guaranteed for other references. On the other hand, the proposed method uses the same control-oriented model but *guarantees* constraint satisfaction in the presence of the same unmodelled dynamics for all references used in the RCI set calculation.

Proposed controller vs standard MPC and cascaded PI controller

Based on the fact that the cascaded PI controller is still widely used in industry, it represents a good candidate to provide a benchmark for assessing the performance of the proposed algorithm. To further demonstrate the effectiveness of the proposed controller while comparing with cascaded controller, we retune the cost function of proposed controller to $J = 10^5 \left(y_r(k+i) - \hat{x}_e(i|k)\right)^2 + 0.4u^2(i|k)$ for less conservative control. Fig. 4.4a illustrates the simulated tracking performance of the proposed controller, resulting from the current applied as shown in Fig. 4.4b. The end effector position still remains inside the error bound and input current stays within the acceptable range, and further validates the efficacy of the proposed approach.

Since the position of the end effector is not measurable, only the motor position and velocity errors are used by the cascaded PI architecture. This approach is typical

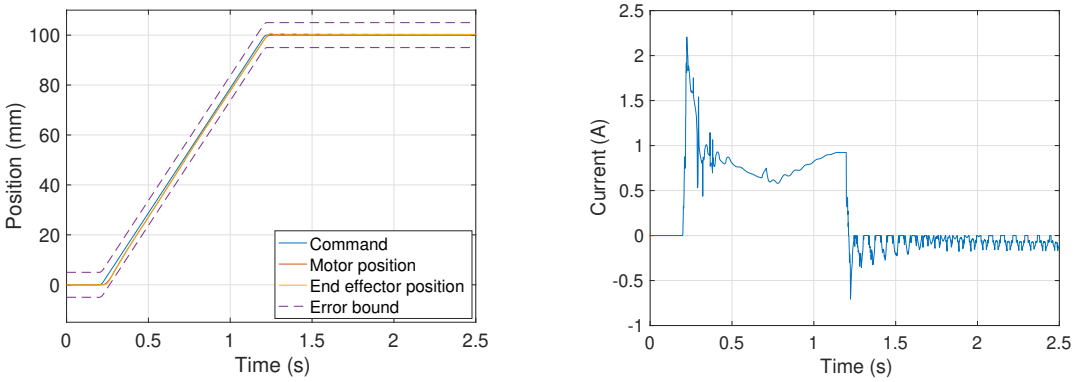

(a) (b)

Fig. 4.4: Simulated point-to-point tracking of proposed controller with $Q_1 = 10^5, R_1 = 0.4$: (a) position trajectory, (b) current command generated by proposed controller.

of an industrial implementation. For a fair comparison, a notch filter was added after the calculated current command, and the calibration of the cascaded controller was undertaken using the high-fidelity plant model and the same cost function used in the MPC formulation. After tuning to achieve good performance, the proportional gain and integral time constant of the velocity loop controller are $k_{pv} = 38.21$ As/m, $T_{iv} = 0.04$ s. The proportional gain of the position loop is chosen as $k_{pp} = 30$ (1/s). A continuous notch filter is designed with 0.80 minimum gain and 0.18 damping ratio. The continuous notch filter is then discretised by Tustin discretisation and used in digital control.

To provide a fairer comparison between the cascaded PI and the proposed algorithm, two sampling rates of the PI controller are considered to allow for the increased computational demand of the optimisation problem in (4.20). In the first case, an identical sample rate of 1 kHz is initially considered for both controllers, whilst a faster rate of 4 kHz is also used with the PI controller to reflect the higher computational load associated with incorporation of an MPC approach and provide a 'computationally-agnostic' comparison of the controller architectures. To improve the performance of the standard MPC relative to Fig. 4.3, it is retuned with weightings $Q_1 = diag(0, 0, 10^5, 0), R_1 = 0.4$. The terminal penalty weight P_1 is subsequently found by solving the discrete-time algebraic Riccati equation using these values.

The resulting end-effector tracking errors for all four control approaches are dis-

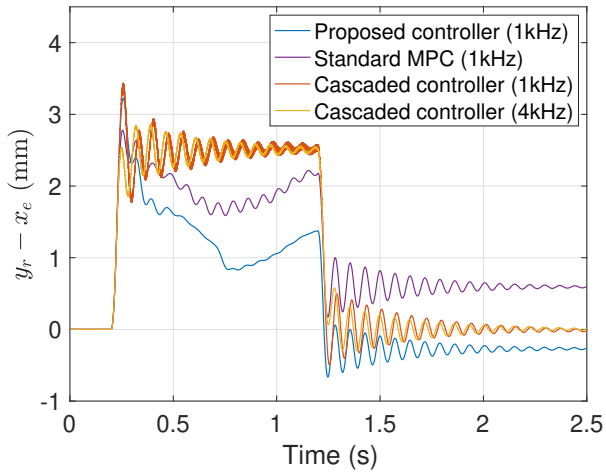

Fig. 4.5: Simulated end-effector tracking error by using different control methods and sampling rate for point-to-point movement.

played in Fig. 4.5. It can be seen that the tracking error of these approaches remains within the specified error tolerance, which is not unexpected considering the simulation model does not explicitly consider estimation error, and thus the disturbance forces arise from the algorithm only considering nonlinear effects considered in (3.7) and (3.8). It is interesting to note, however, that the error trajectories with proposed controller and cascaded PI at 1 kHz sample rate are very close, 3.22 mm and 3.44 mm respectively. Increasing the sample rate for the cascaded PI controller to 4 kHz leads to a slightly reduced 2.86 mm maximum tracking error. As seen in Fig. 4.5, the retuned standard MPC exhibits comparable performance to the proposed MPC scheme, although it must be noted this standard approach does not guarantee constraint satisfaction and requires more calibration of the cost function weights relative to the proposed approach.

Once again, the key benefit of the model-based approach becomes more apparent when looking at the transient response, where significant reductions in the vibration are achieved during the constant velocity manoeuvre from 0.2 to 1.2 s. The average tracking error achieved by the proposed controller is 0.54 mm, which is approximately 20% smaller than 0.66 mm and 0.65 mm achieved by the cascaded controllers operating at 1 kHz and 4 kHz sampling rates.

The key effectiveness of the proposed controller is that it can *guarantee* the desired

tolerance is retained. After the reference reaches the desired position of 0.1 m, the value of control input calculated based on on-line optimisation is reduced considering the error bound already within the required error tolerance. The negative current at the steady state intends to reduce the tracking error, but this force is neutralised by the un-modelled disturbance force, which can be seen from Fig. 4.4b. This causes the small vibration and steady-state offset (albeit within the tolerance bound) of the proposed controller after deceleration - if it was desirable to fully remove the steady-state error, this could be tackled by integrator augmentation within the MPC as discussed in [135].

4.3.3 Experiment results and comparison

Due to the communication limits between the target computer and drive, only the experimental tracking performances of the proposed controller and cascaded PI controller with 1 kHz sampling rate are demonstrated. The same tuning parameters and constraint tolerances as discussed in the Subsection 4.3.2 are considered here, although the optimisation problem (4.20) and solver are matched using CVXGEN to ensure fast on-line implementation [136].

Initially, the same point-to-point reference tracking is conducted. The tracking performance and current output of the proposed controller are given in Fig. 4.6a and Fig. 4.6b respectively. As expected, the trajectory of the end effector lies inside the error bound, and the state and input constraints are obeyed, which supports the proposed controller's ability to maintain error tolerances in the case of further un-modelled disturbances than were considered in the simulation.

As the end effector position was measured (although not used in either control formulation), it is possible to present the corresponding estimated tracking error and the measured tracking error, as shown in Fig. 4.7. The maximum estimated and actual tracking error of end effector are $\|y_r - \hat{x}_e\|_\infty = 4.27$ mm and $\|y_r - x_e\|_\infty = 4.88$ mm.

As seen from Fig. 4.7, the estimated tracking error is within the $\bar{\epsilon}_e$ bound and the actual tracking error is within the ϵ_e error bound. Also, same tracking error offset

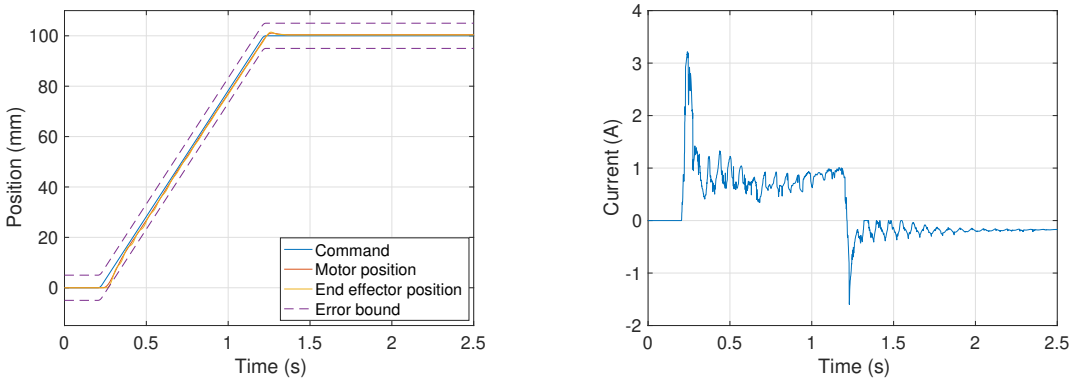

(a) (b)

Fig. 4.6: Experimental point-to-point tracking of proposed controller: (a) position trajectory, (b) current command generated by proposed controller.

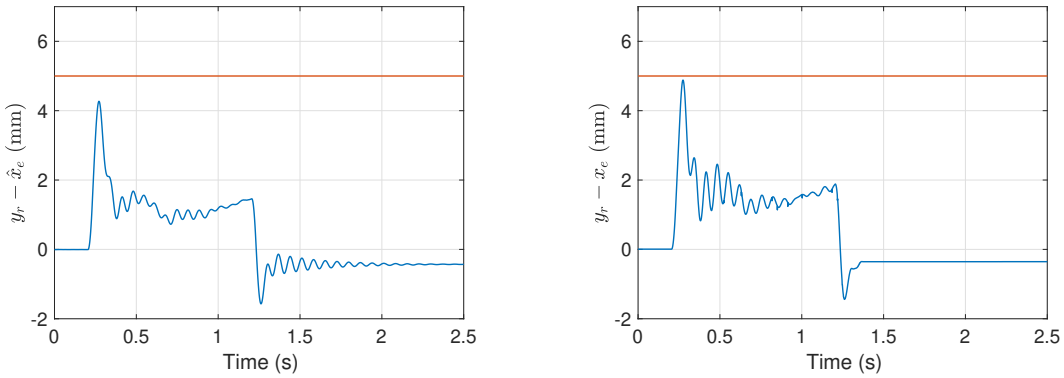

(a) (b)

Fig. 4.7: Experimental end effector tracking error of proposed controller based on point-to-point reference: (a) estimated error; (b) actual error.

as shown in simulation can be seen at the steady state. The vibration after deceleration is smaller compared to simulation (in this case helpful) because an un-modelled disturbance (friction) on the end effector is not considered in the simulation.

For comparison, the trajectory tracking of the same point-to-point reference based on the cascaded controller is conducted, and the tracking error is shown in Fig. 4.8. In this case, the maximal tracking error from the motor and end effector side is 3.87 mm and 5.46 mm, respectively. It can be seen that the tracking error on the motor side is within the desired error bound. However, the end effector tracking error exceeds the

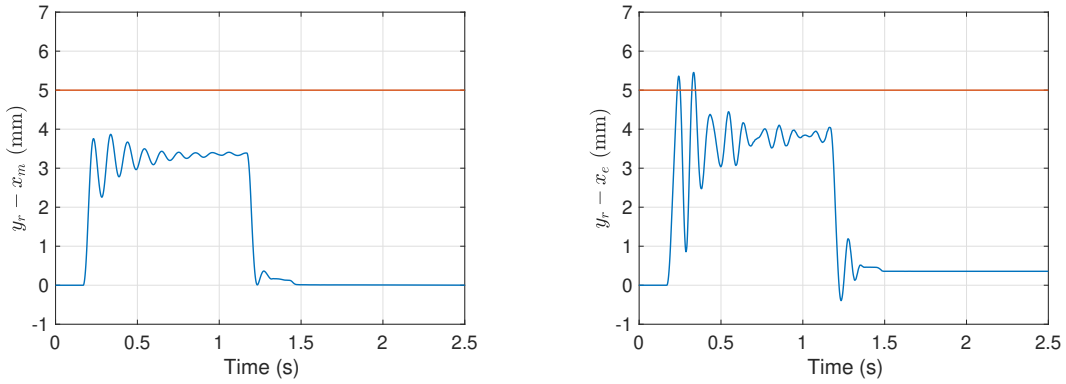

(a) (b)

Fig. 4.8: Experimental end effector tracking error of cascaded PI controller based on point-to-point reference: (a) motor side; (b) end effector side.

error bound, and a more obvious oscillation can be seen on the end effector tracking error, Fig. 4.8b compared to the performance of the proposed controller, Fig. 4.7b.

To further assess the capabilities of the proposed approach, a cosine reference, $y_r = 0.05 + 0.05\cos(2t)$, is considered. This form of reference is typical in generating a circular contour in machining applications. The end effector tracking error of the two control methods is presented in Fig. 4.9. It shows the maximum tracking error is reduced from 3.71 mm to 2.76 mm using the proposed method. Although the error tolerance is achieved by the cascaded PI controller, the qualitative assessment of the two trajectories suggests the proposed approach may be able to achieve a tighter error bound.

The experimental results demonstrate the potential for implementing the proposed control scheme on a machine with an industrial level sampling rate. Furthermore, the proposed approach, in being able to guarantee a given tolerance, offers substantial benefit in machining applications. Naturally, whilst the performance of the proposed approach is superior in the case studies considered, this does come at a computational cost, as the average computation time of MPC in the experiments considered was found to be 0.69 ms at each sampling instant, which is substantially higher than that of the cascaded PI algorithm, 0.04 ms. The maximum computation time of MPC and cascaded PI is 0.72 ms and 0.13 ms respectively. The relative merit of ensuring tolerance bounds are met using the proposed approach must be weighed against the potential increase in

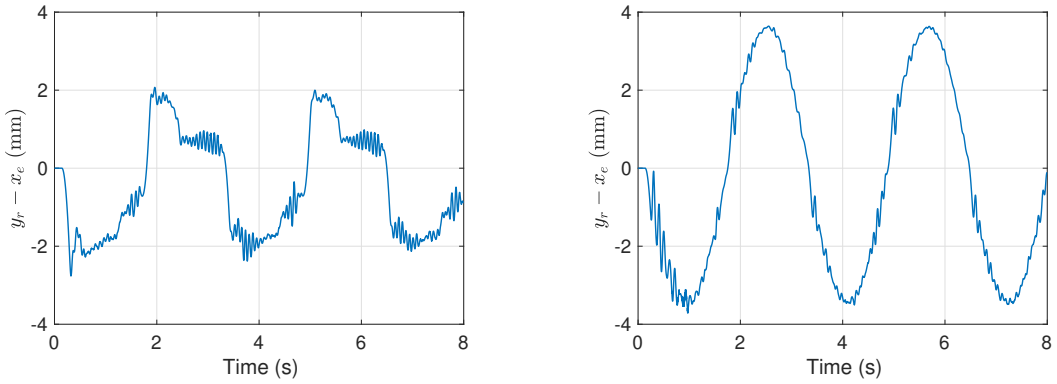

Fig. 4.9: Experimental sinusoidal reference end effector tracking error of two methods: (a) proposed controller; (b) cascaded PI controller.

computational, and therefore financial cost when fully considering the choice of which algorithm to use in an industrial context.

4.4 Summary

In this chapter, an error bounded tracking control scheme based on an MPC structure is proposed. The approach requires the estimation of the maximal RCI set to ensure that feasibility and stability guarantees for the approach are possible. As existing approaches for estimating RCI sets may not converge, an augmented approach was proposed.

The proposed robust MPC algorithm was then tested in both simulations and on a linear motor test rig with a flexible connection to the end effector. It has been demonstrated that the proposed controller guarantees satisfaction of the specified end-effector error bound and can be implemented in real time on an industrial machine with a 1 ms sampling time. By contrast, the error bound was exceeded by a conventional cascaded PI controller with a notch filter.

This page intentionally left blank.

Chapter 5

Modelling and contouring control of a biaxial industrial gantry machine *

DUAL drive gantry machines are widely used in industry for manufacturing. However, due to the limited joint stiffness, the non-synchronised movement of the dual drive may lead to deterioration in contouring accuracy, and traditional control architectures commonly used in machining cannot explicitly bound the contouring error to meet a desired tolerance. In this chapter, we first propose a model predictive control architecture based on switched linear time invariant control-oriented models as an extension of Chapter 4. This controller is able to guarantee a two-dimensional contouring tolerance in the presence of uncertainty arising from imperfect drive synchronisation. A second MPC is also proposed, with stronger assumptions on the reference trajectory to be tracked. These assumptions lead to less conservative performance results but will be more restrictive in the paths that can be followed.

To develop the controllers, we introduce a high-fidelity model for the dual drive gantry machine in Section 5.1. The parameters of the model are identified using data from an industrial machine, and the results are presented in Section 5.2. In Section 5.3 and Section 5.4, we present the two contouring error bounded control algorithms. For the first approach, the contouring error bound is guaranteed by ensuring the tracking error of each axis is within the desired tolerance, whereas the second contouring controller is designed to bound the calculated contouring error explicitly in real time. To test the

*Part of this chapter is presented in *Proc. 3rd IEEE Conference on Control Technology and Applications* [137] and a significant part is being prepared for journal submission.

efficacy of proposed methods and based on the fact that the position measurement of end-effector for laser machine is not applicable, we build a back-to-back motor based test bench. Simulation and experiment results are presented in Sections 5.5 and 5.6.

5.1 System description

A typical structure of the dual-drive gantry machine consists of two motors that separately sit on parallel linear slides carrying a crossbeam in the orthogonal direction. Generally, there is another drive on the gantry holding the end-effector head. The industrial machine shown in Fig. 2.4a is investigated in this chapter.

Since intensive finite-element optimisation has been widely used for the structural design of industrial machines, the structural parts generally have more rigidity than the joints. Such machines can be successfully modelled with rigid elements connected by flexible joints [18].

5.1.1 Structural configuration

In order to capture the characteristics of systems with limited stiffness joints, we firstly propose a physics-based model with linear and torsional springs that possesses position-dependent structural coupling characteristics as shown in Fig. 5.1. This schematic figure shows the behaviour of the system when the dual drive is in synchronised (dot grey line) and non-synchronised (solid black line) conditions. In order to allow the lateral deformation in the X direction, linear springs that link the Y-axis motors and linear guides are introduced. The two linear springs with spring constant k_s are assumed symmetrically located at the vertical centre of the two sides of each Y-axis motors. The torsional spring links the drive and crossbeam with spring constant k_r.

In the schematic of the gantry machine, OXY is the fixed inertial coordinate frame with origin O located in the middle point between the two linear guides and Y axis parallel to the linear guides. Let O' be the centre of mass (CoM) of the crossbeam. The

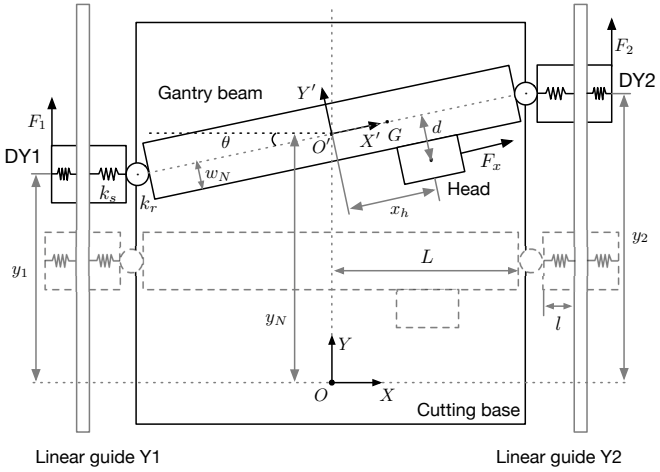

Fig. 5.1: Schematic of moving gantry machine with Y-axis dis-synchronisation.

half-length of the crossbeam and motor are L and l respectively. The half-width of the beam is w_N. The dual drives on Y axis are denoted as $DY1$ and $DY2$ respectively. Here, $O'X'Y'$ is a moving coordinate frame with the X' axis paralleling the lateral direction of the beam.

When the movements of the two Y-axis drives are not synchronised perfectly, the angle formed between the X and X' axes is θ. The moving distance of the X-axis head with respect to X' is x_h which can be directly measured by the linear encoder on the gantry. Let d denote the projection of the distance between the head and beam mass centre in the Y' direction. Given the mass of the head is relatively small compared to the mass of crossbeam, the centre of mass of the entire assembly is well approximated by the COM, O'

Finally, let y_1, y_2 be the position of the Y-axis motors along the respective guides, which can be measured by the linear encoders.

5.1.2 Lagrangian-based system modelling

If it is assumed that the rotation angle of the gantry is small and the beam is rigid, the angle of rotation and position of CoM for the gantry beam can be approximated by $\theta = (y_2 - y_1)/2L$ and $y_N = (y_1 + y_2)/2$. Linear springs are included to support some

degree of misalignment between $DY1$ and $DY2$, although translational dynamics are neglected in the modelling. The planar movement dynamics can be described by the generalised coordinates x_h, y_N and θ.

Based on these generalised coordinates, the CoM positions of Y-axis drives, gantry and end effector head are respectively defined as:

$$\begin{aligned}
P_1 &= (x_1, y_1) = (-L\cos\theta - l, y_N - L\sin\theta),\\
P_2 &= (x_2, y_2) = (L\cos\theta + l, y_N + L\sin\theta),\\
P_N &= (0, y_N),\\
P_e &= (x_h\cos\theta + d\sin\theta, y_N + x_h\sin\theta - d\cos\theta).
\end{aligned}$$

The velocity of the four separate objects, namely two dual drives, gantry and end effector head, are denoted as V_1, V_2, V_N and V_e with value:

$$V_1 = \begin{bmatrix} L\sin\theta\dot{\theta} \\ \dot{y}_N - L\cos\theta\dot{\theta} \end{bmatrix}, V_2 = \begin{bmatrix} -L\sin\theta\dot{\theta} \\ \dot{y}_N + L\cos\theta\dot{\theta} \end{bmatrix},$$

$$V_N = \begin{bmatrix} 0 \\ \dot{y}_N \end{bmatrix}, V_e = \begin{bmatrix} \Upsilon\cos\theta - x_h\sin\theta\dot{\theta} \\ \dot{y}_N + \Upsilon\sin\theta + x_h\cos\theta\dot{\theta} \end{bmatrix}, \tag{5.1}$$

where $\Upsilon \triangleq \dot{x}_h + d\dot{\theta}$. Let M_1, M_2, M_e and M_n denote the mass of the drive $DY1$, drive $DY2$, X-axis head drive, and the gantry respectively. Since the gantry and end-effector are two distinct rigid bodies, only the rotary kinetic energy of the gantry is calculated. Let I_N denotes the moment of inertia of the gantry corresponding to the central point O' as:

$$I_N = \frac{1}{12}M_n\left((2L)^2 + (2w_N)^2\right). \tag{5.2}$$

The moment of inertia of the end effector head about its centre of mass is assumed negligible. The total kinetic energy is then calculated as

$$\mathcal{K} = \frac{1}{2}M_1V_1^TV_1 + \frac{1}{2}M_2V_2^TV_2 + \frac{1}{2}M_nV_N^TV_N + \frac{1}{2}M_eV_e^TV_e + \frac{1}{2}I_N\dot{\theta}^2. \tag{5.3}$$

The total potential energy stored in linear and torsional springs is $\mathcal{P} = k_r\theta^2 + k_s L^2 (1-\cos\theta)^2$. The Lagrangian, $\mathcal{L} = \mathcal{K} - \mathcal{P}$, allows the dynamic equations for this three degree-of-freedom system with generalised coordinates $q_j = \{x_h, y_N, \theta\}$, $j = 1, 2, 3$ to be calculated from the Lagrange equation $\frac{d}{dt}\left(\frac{\partial \mathcal{L}}{\partial \dot{q}_j}\right) - \frac{\partial \mathcal{L}}{\partial q_j} = Q_{q_j}$.

The external generalised forces Q_{q_j} are computed based on kinematic approach:

$$Q_{x_h} = k_x i_x - b_x \dot{x}_h, \tag{5.4}$$

$$Q_{y_N} = k_y(i_1 + i_2) - b_y(\dot{y}_1 + \dot{y}_2), \tag{5.5}$$

$$Q_\theta = (k_y(i_2 - i_1) - b_y(\dot{y}_2 - \dot{y}_1))\, L\cos\theta, \tag{5.6}$$

where k_x, k_y are the force constant of the X, Y-axis motors; i_x, i_1, i_2 are the current inputs of the end effector motor, drives $DY1$ and $DY2$ respectively; b_x, b_y are the viscous friction coefficient of gantry and linear guides, where the viscous coefficients on $Y1$ and $Y2$ are assumed identical.

The governing equations of the gantry mechanism are given by (5.7), (5.8) and (5.9),

$$M_e(-x_h\dot{\theta}^2 + \ddot{x}_h + d\ddot{\theta} + \ddot{y}_N \sin\theta) = Q_{x_h}, \tag{5.7}$$

$$\begin{aligned} &M_e \sin\theta \ddot{x}_h + M_t \ddot{y}_N + (M_e d\sin\theta - M_d L\cos\theta + M_e x_h \cos\theta)\,\ddot{\theta} + M_e(-x_h \sin\theta\dot{\theta}^2 \\ &+ 2\dot{x}_h\cos\theta\dot{\theta} + d\dot{\theta}^2\cos\theta) + M_d L\dot{\theta}^2\sin\theta = Q_{y_N}, \end{aligned} \tag{5.8}$$

$$\begin{aligned} &M_e d\ddot{x}_h + (M_e d\sin\theta - M_d L\cos\theta + M_e x_h\cos\theta)\,\ddot{y}_N + \Bigg(L^2(M_1+M_2) + \frac{M_n(L^2+w_N^2)}{3} \\ &+ M_e\left(d^2 + x_h^2\right)\Bigg)\ddot{\theta} + 2k_r\theta + 2L^2 k_s \sin\theta(1-\cos\theta) + 2M_e\dot{\theta}\dot{x}_h x_h = Q_\theta, \end{aligned} \tag{5.9}$$

where $M_t = M_1 + M_2 + M_e + M_n$ is the total mass of the system; $M_d \triangleq M_1 - M_2$ is the mass difference. Unlike existing models, the governing equations are able to capture the position dependent structural variation when the head motor moves along the gantry beam.

5.2 System identification

To parameterise the proposed model, data was collected from a commercial laser machine shown in Fig. 2.4a. This machine is made by Farley Laserlab with a moving distance of 1.5 and 3 m in X and Y axes respectively. Analogue incremental encoders ERN1387 with 2048 lines resolution are used to measure the position of actuators.

During the laser cutting process, the raw material to be cut is put on the operating base, and the cutter moves above the base to perform the desired movement as specified by engineers. To increase productivity, the operating base is movable. By interchanging two operating bases, the time for removing and loading the machining parts is saved. However, if the base is not installed properly, the movable operating base may induce oscillation when the cutter moves.

5.2.1 Acceleration test

Considering the operating base may have potential oscillation, before conducting the system identification, we install two accelerometers on the laser head and cutting base separately for acceleration test. The experiment setup is shown in Fig. 5.2. We require the machine to move with high speed and acceleration to double-check if there is unexpected relative vibration between the laser head and base when the machine moves.

The two accelerometers are based on Bosch XDK110 sensor platform and are programmed with features including SD-card data recording and wireless-controlled operation. The sampling rate of accelerometers is set as 1 kHz, and a square-shape movement is conducted.

The reference and the trajectory of two axes are shown in Fig. 5.3. For validation, the acceleration of the laser head and cutting base from accelerometers is compared with the value derived from the motor position. The measured acceleration for X and Y axes are shown in Fig. 5.4 and Fig. 5.5 respectively. The red lines in Fig. 5.4 and Fig. 5.5 reflect the actual machine movement, which is the acceleration derived from the actuator position.

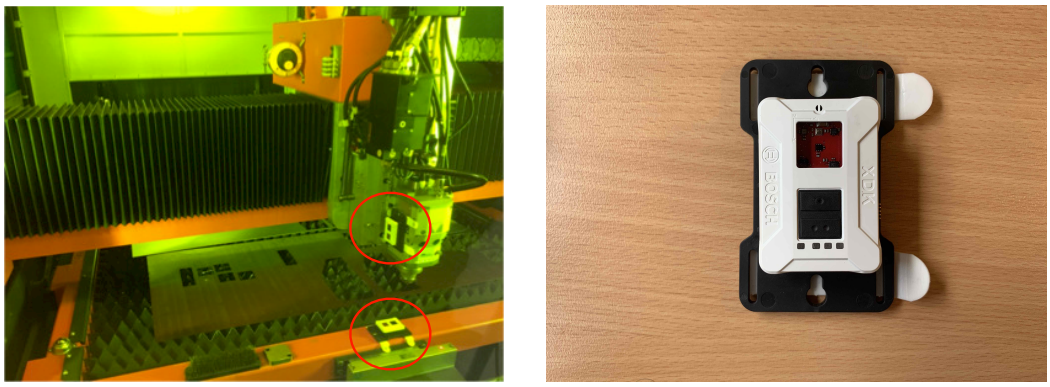

(a) (b)

Fig. 5.2: Experiment setup for acceleration test: (a) two accelerometers that are installed; (b) accelerometer based on Bosch XDK110 platform.

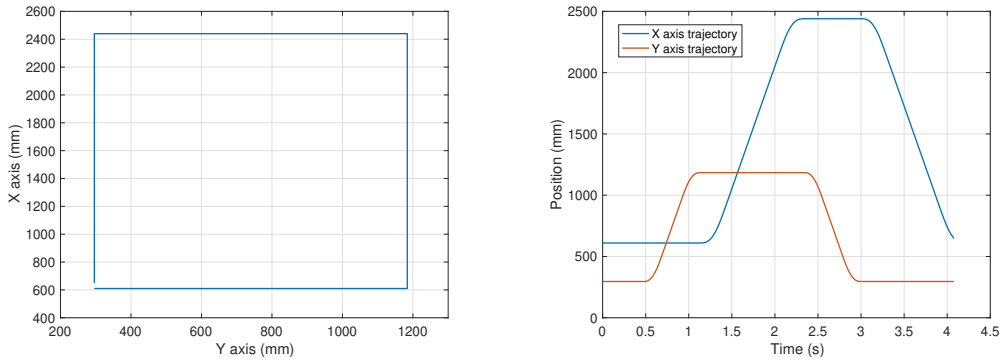

(a) (b)

Fig. 5.3: The reference for acceleration test: (a) desired contour; (b) trajectory of two axes.

The accelerometer installed on the laser head is used to validate the reliability of sensor, and it can be seen from the shaded area 1 and 3 in Fig. 5.4a and area 1 in Fig. 5.5a that the mean value of blue line agrees with the red line for X and Y axes.

However, as highlighted in the shaded area 2 of Fig. 5.4a, there is a discrepancy between the measured acceleration and the double derivative from the motor position. This shows that the sensitivity of the accelerometer mounting makes it unsuitable for controller design in most cases.

In the meantime, as highlighted in Fig. 5.4b and Fig. 5.5b, the movement of the laser head does not lead to the oscillation of the operating base. This is important because the

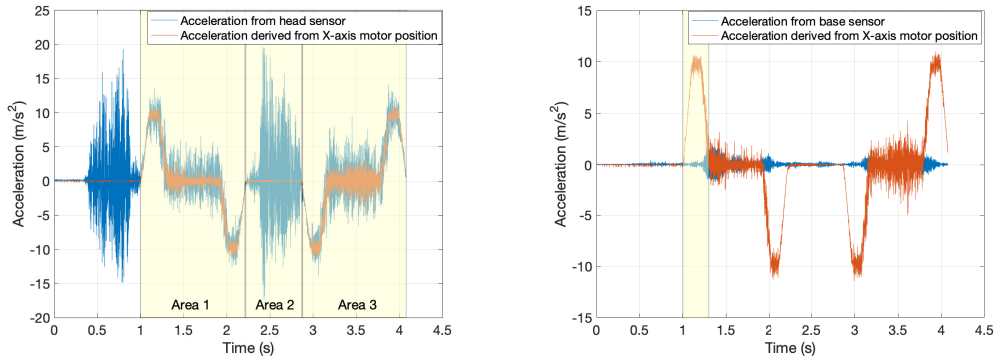

(a) (b)

Fig. 5.4: X-axis acceleration: (a) data measured from sensor installed at laser head; (b) data measured from sensor installed at operating base.

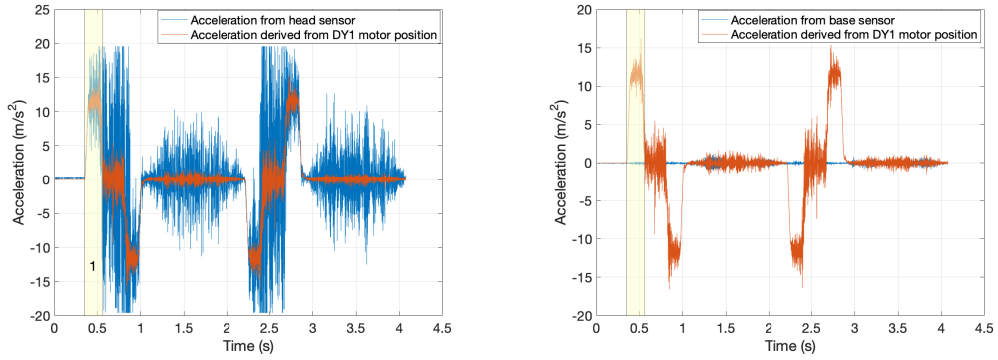

(a) (b)

Fig. 5.5: Y-axis acceleration: (a) data measured from sensor installed at laser head; (b) data measured from sensor installed at operating base.

dynamics of base vibration can be ignored in modelling the machine.

5.2.2 Parameter identification

To simplify the system identification, a small angle approximation to (5.8) and (5.9) is applied at different operating point $\bar{x}_h$ and the terms $M_e\bar{x}_h\ddot{\theta}$ and $M_e\bar{x}_h\ddot{y}_N$ arising are neglected and considered as plant-model mismatch. The full-order nonlinear model is

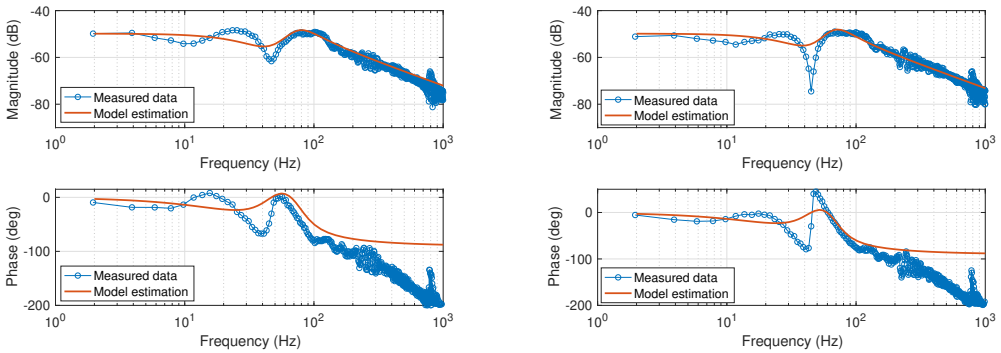

(a) (b)

Fig. 5.6: Bode plot from drive current to velocity when the laser head is located at different positions: (a) $\bar{x}_h = 0$ m, (b) $\bar{x}_h = -0.66$ m.

then approximated by the following dynamic equations for y_1 and y_2:

$$M_t \left(\frac{\ddot{y}_1 + \ddot{y}_2}{2} \right) + b_y \left(\dot{y}_1 + \dot{y}_2 \right) = k_y \left(i_1 + i_2 \right), \tag{5.10}$$

$$J \frac{\ddot{y}_2 - \ddot{y}_1}{2L} + b_y L \left(\dot{y}_2 - \dot{y}_1 \right) + k_r \frac{y_2 - y_1}{L} = k_y L \left(i_2 - i_1 \right), \tag{5.11}$$

where $J(\bar{x}_h) \triangleq J_0 + M_e \bar{x}_h^2$ is the total moment of inertia which depends on value of $\bar{x}_h$, and $J_0 \triangleq L^2 \left(M_1 + M_2 \right) + \frac{M_n \left(L^2 + w_N^2 \right)}{3} + M_e d^2$. Noting J has $\bar{x}_h$ dependency, the approximated transfer function from current i_1 to the drive velocity $\dot{y}_1$ is:

$$G_{iv1}(s) = \frac{k_y \left(\left(J + L^2 M_t \right) s^2 + 4 L^2 b_y s + 2 k_r \right)}{\left(M_t s + 2 b_y \right) \left(J s^2 + 2 L^2 b_y s + 2 k_r \right)}. \tag{5.12}$$

Several of these parameters can be identified from the machine data sheet (e.g. the force constants, k_x and k_y) while the remainder (e.g. J_0, M_t, b_y, k_r) must be identified from the frequency response of collected data. During the data collection, the Y-axis motors are excited with a 4 A peak amplitude chirp-signal current when X-axis motor is held constant at $\bar{x}_h = 0$ m and $\bar{x}_h = -0.66$ m.

The experimental and modelled frequency responses are shown in Fig. 5.6. The physical system exhibits a change in anti-resonance frequency from approximately 47 Hz to 45 Hz as the X-axis motor is moved from 0 to 66 cm along the gantry beam,

exhibiting a state-dependence of this motor on the resulting dynamics. The modelled system is able to capture this dependence and also exhibits a similar magnitude shift in anti-resonance frequency.

5.3 Contouring error bounded control based on bounded tracking error

5.3.1 Control-oriented modelling

To formulate the contouring error bounded controller, the control-oriented model is first derived. For the X axis, the dynamics equation (5.7) can be reformulated as (5.13) by lumping all terms involving y_N, θ into a disturbance term:

$$\ddot{x}_h + \frac{b_x}{M_e}\dot{x}_h = \frac{k_x}{M_e}i_x + d_x, \tag{5.13}$$

where the disturbance term is $d_x \triangleq x_h\dot{\theta}^2 - d\ddot{\theta} - \ddot{y}_N \sin\theta$. To develop an approximate model of Y axis without dependence on the dynamics of x_h, the (5.8) and (5.9) are approximated at different operating point $\bar{x}_h$ and rearranged as follows by applying a small angle approximation:

$$M_t\ddot{y}_N + 2b_y\dot{y}_N + M_e\bar{x}_h\ddot{\theta} = k_y\left(i_1 + i_2\right) + d_1, \tag{5.14}$$

$$M_e\bar{x}_h\ddot{y}_N + J\ddot{\theta} + 2b_yL^2\dot{\theta} + 2k_r\theta = k_yL\left(i_2 - i_1\right) + d_2, \tag{5.15}$$

where M_d is assumed to be zero; the disturbance force are $d_1 = M_e(\bar{x}_h\theta\dot{\theta}^2 - \theta\ddot{x}_h - d\theta\ddot{\theta} - 2\dot{x}_h\dot{\theta} - d\dot{\theta}^2)$ and $d_2 = -M_e(2\dot{\theta}\dot{x}_h\bar{x}_h + d\theta\ddot{y}_N + d\ddot{x}_h)$.

Multiple linearisation at different $\bar{x}_h$ is undertaken to reduce the model mismatch, leading to a switched LTI model for these axes.

5.3.2 Preliminary of controller formulation

For the type of two-axes contouring problem commonly seen industrially, the reference trajectory is time stamped and is therefore different from the class of path-following problems. In this subsection, we will extend the tracking error bounded controller in Chapter 4 to the contouring control problem.

As discussed in Section 1.1, the bounded tracking error can lead to a bounded contouring error. For the contouring error bounded control (CEBC) problem investigated, we have the lemma as follows:

Lemma 5.1. *Given a desired contouring error bound ϵ_c, the bounded contouring error $\|\epsilon\|_\infty \leq \epsilon_c$ can be guaranteed by bounding the tracking error of X and Y axes as $\|e_x\|_\infty + \|e_y\|_\infty \leq \epsilon_c$.*

Proof. Since $(x_e^c(k), y_e^c(k))$ is the closest point from the actual end effector position, we have $|\epsilon(k)| \leq |e_c(k)|$, $\forall k$. Based on the triangle inequality, we have $|e_c(k)| \leq |e_x(k)| + |e_y(k)|$. Then the following inequalities hold: $|\epsilon(k)| \leq |e_c(k)| \leq |e_x(k)| + |e_y(k)| \leq \epsilon_c$. □

From Lemma 5.1, the control objective can be restated as ensuring $\|e_x\|_\infty \leq \epsilon_x$ and $\|e_y\| \leq \epsilon_y$, where ϵ_x and ϵ_y are the upper bound of tracking error on X and Y axes respectively, and $\epsilon_x + \epsilon_y = \epsilon_c$.

Because the X-axis tracking error in the control oriented model is $e_x = x_e^* - x_e = x_e^* - x_h - d\theta$, the following remark is provided to show how to ensure $\|e_x\|_\infty \leq \epsilon_x$ based on the X-axis dynamics and reference trajectory.

Remark 5.1. *Consider a desired X-axis tracking error bound, ϵ_x that the system is initialised within, and set the rotation angle constraint as $|\theta| \leq \theta_{max} \leq \epsilon_x/d$. If the designed X-axis controller can guarantee $|x_e^*(k) - x_h(k)| \leq \bar{\epsilon}_x \triangleq \epsilon_x - d\theta_{max}$, $\forall k$, the bounded tracking error can be guaranteed, i.e. $\|e_x\|_\infty \leq \epsilon_x$. Note that the RCI set calculation in this instance potentially introduces an asymmetry between the X- and Y- axes error bounds due to the $d\theta_{max}$ tightening of ϵ_x. This is an artefact of decoupling the axes controller in the proposed approach.*

5.3.3 Model predictive based controller formulation

A tracking error bounded control method for a single-axis machine described as an LTI system with disturbance has been proposed in [131]. We now extend this work to allow bounds to be imposed on contouring error in biaxial systems.

Same as the single-axis tracking problem, the trajectory of end-effector position is assumed to be generated offline and with specified position, velocity and acceleration constraints. In keeping with standard approaches, we assume the reference model of individual axis is in the same format of (4.6) as:

$$r_j(k+1) = A_r r_j(k) + B_r a_j(k),\ j = \{x, y\}\,, \tag{5.16}$$

where $r_j \in \mathbb{R}^2$, $a_j \in \mathbb{R}$ are the state and input of the reference model. The matrices A_r and B_r are given with reference sampling time T_r as:

$$A_r = \begin{bmatrix} 1 & T_r \\ 0 & 1 \end{bmatrix},\ B_r = \begin{bmatrix} 0 \\ T_r \end{bmatrix}.$$

For X-axis reference, $r_x \triangleq \begin{bmatrix} x_e^* & v_x^* \end{bmatrix}^T$ with x_e^* and v_x^* as the desired position and velocity and a_x is the desired acceleration. The same model (5.16) can be used to describe the evolution of Y-axis reference as well when states $r_y \triangleq \begin{bmatrix} y_e^* & v_y^* \end{bmatrix}^T$ represent the Y-axis desired position, velocity and a_y is the acceleration. The reference trajectory generated with (5.16) is considered to satisfy constraints of the form:

$$\begin{bmatrix} -\bar{x}_e \\ -\bar{v}_x \end{bmatrix} \leq r_x \leq \begin{bmatrix} \bar{x}_e \\ \bar{v}_x \end{bmatrix},\ -\bar{a}_x \leq a_x \leq \bar{a}_x, \tag{5.17}$$

$$\begin{bmatrix} -\bar{y}_e \\ -\bar{v}_y \end{bmatrix} \leq r_y \leq \begin{bmatrix} \bar{y}_e \\ \bar{v}_y \end{bmatrix},\ -\bar{a}_y \leq a_y \leq \bar{a}_y. \tag{5.18}$$

The discrete-time state space models for the X and Y axes can be derived from (5.13),

(5.14) and (5.15) with given sampling time T_s as

$$\xi_x(k+1) = A_x\xi_x(k) + B_x i_x(k) + E_x d_x(k), \tag{5.19}$$

$$\xi_y(k+1) = A_y(\bar{x}_h)\xi_y(k) + B_y(\bar{x}_h) i_y(k) + E_y(\bar{x}_h) d_y(k), \tag{5.20}$$

where $\xi_x \triangleq (x_h, \dot{x}_h)$, $\xi_y \triangleq \left(y_N, \dot{y}_N, \theta, \dot{\theta}\right)$ are the states, i_x, $i_y \triangleq (i_1, i_2)$ are the inputs; $d_y \triangleq (d_1, d_2)$ is the disturbance vector. The system coefficient matrix of (5.19) and (5.20) and d_y can be inferred from (5.14) and (5.15).

The states and inputs of the system are required to remain within bounded constraints, i.e.:

$$\xi_x \in \mathcal{X}_m \subseteq \mathbb{R}^2,\ \xi_y \in \mathcal{X}_y \subseteq \mathbb{R}^4,\ i_x \in \mathcal{U}_x \subseteq \mathbb{R},\ i_y \in \mathcal{U}_y \subseteq \mathbb{R}^2. \tag{5.21}$$

As a conservative approach, the constraints on states and inputs are used to define bounds on the disturbance forces using the explicit form of d_x and d_y in (5.19), (5.20). This leads to compact disturbance sets of the form:

$$d_x \in \mathcal{W}_x \subseteq \mathbb{R},\ d_y \in \mathcal{W}_y \subseteq \mathbb{R}^2.$$

Based on the definition of RCI and robust admissible input (RAI) set, we require the reference generated by (5.16) stays in the reference CI set $r_j(k) \in \mathcal{R}_\infty^{r_j}, \forall k \in \mathbb{Z}_{0+}$ during all the process by selecting $a_j(k) \in \Theta^{a_j}(r_j(k)) \subseteq \mathcal{U}_{a_j}$, for $j = \{x, y\}$.

Then, to ensure $\|x_e^* - x_h\|_\infty \leq \bar{\epsilon}_x$, we start by defining a set of the system and reference states, $\mathcal{S}^{\xi_x, r_x}$ with feature,

$$\mathcal{S}^{\xi_x, r_x} = \left\{(\xi_x, r_x) \,|\, \xi_x \in \mathcal{X}_m, r_x \in \mathcal{R}_\infty^{r_x}, \|x_e^* - x_h\|_\infty \leq \bar{\epsilon}_x\right\}. \tag{5.22}$$

If at any time $k \in \mathbb{Z}_{0+}$ the combined state $(\xi_x(k), r_x(k)) \in \mathcal{S}^{\xi_x, r_x}$, we want the system and reference states stay in $\mathcal{S}^{\xi_x, r_x}$ in the next time instant as well. This requires a RCI set

$\mathcal{R}^{\xi_x,r_x} \subseteq \mathcal{S}^{\xi_x,r_x}$ as

$$(\xi_x(k), r_x(k)) \in \mathcal{R}^{\xi_x,r_x}, \exists_{i_x(k)\in\mathcal{U}_x} : (\xi_x(k+1), r_x(k+1)) \in \mathcal{R}^{\xi_x,r_x}, \\ \forall\, (d_x(k), a_x(k)) \in (\mathcal{W}_x \times \Theta^{a_x}(r_x))\,,$$

where $\Theta^{a_x}(r_x)$ is the robust admissible input (RAI) set for reference CI set $\mathcal{R}^{r_x}$. For system with disturbance, the RCI set is generally not finitely determined. We will use the method proposed in [131] to calculate the $\mathcal{R}^{\xi_x,r_x}$ in finite number of steps.

The reference position trajectory is assumed known N steps ahead, and may be used to establish a reference velocity trajectory. Thus, using the reference $\gamma_x^N(k) = (r_x(k), \cdots, r_x(k+N-1))$, the X-axis MPC solves the following optimisation problem at each time instant:

$$\begin{aligned} U_x^*(k) = &\arg\min_{U_x(k)} \sum_{i=0}^{N-1} \left(Q_x \left(x_e^*(k+i) - x_h(i|k)\right)^2 + R_x i_x^2(i|k) \right) \\ s.t.\ \ &\xi_x(i+1|k) = A_x \xi_x(i|k) + B_x i_x(i|k), \\ &x_h(i|k) = \begin{bmatrix} 1 & 0 \end{bmatrix} \xi_x(i|k), \\ &x_e^*(k+i) = \begin{bmatrix} 1 & 0 \end{bmatrix} r_x(k+i), \\ &\xi_x(i|k) \in \mathcal{R}^{\xi_x,r_x}(\xi_x, r_x(k+i)),\ i \in \mathbb{Z}_{[0,N-1]}, \\ &\xi_x(0|k) = \xi_x(k), \end{aligned} \tag{5.23}$$

where Q_x and R_x are the cost function weight on X-axis position error and control input respectively; $U_x^*(k) = (i_x^*(0|k), \cdots, i_x^*(N-1|k))$. At each time instant, the optimal control $i_x(k) = i_x^*(0|k)$ is applied to the plant.

The way of computing RCI set $\mathcal{R}^{\xi_y,r_y}$ is similar to that for $\mathcal{R}^{\xi_x,r_x}$. In order to ensure $\|y_e^* - y_e\|_\infty \leq \epsilon_y$, we start with a set $\mathcal{S}^{\xi_y,r_y}$:

$$\mathcal{S}^{\xi_y,r_y} = \left\{ (\xi_y, r_y) \,|\, \xi_y \in \mathcal{X}_y, r_y \in \mathcal{R}_\infty^{r_y}, \|y_e^* - y_N - \bar{x}_h\theta + d\|_\infty \leq \epsilon_y \right\}. \tag{5.24}$$

Since x_h is approximated as a piecewise constant $\bar{x}_h$ over its operating range, for

system (5.20) we need to compute the RCI set $\mathcal{R}_{\bar{x}_h^j}^{\xi_y,r_y}$ for each linearisation point $\bar{x}_h^j$ for $j = 1, \cdots, N_l$ where N_l is the total number of linearisation point. Clearly, there is another trade-off in that using finer intervals in $\bar{x}_h$ leads to a better approximation of x_h, but leads to more controller switching and requires more off-line calculation and storage of the RCI sets. The following requirement is imposed for the off-line RCI set calculations:

$$(\xi_y(k), r_y(k)) \in \mathcal{R}_{\bar{x}_h^j}^{\xi_y,r_y}, \exists_{i_y(k)\in\mathcal{U}_y} : (\xi_y(k+1), r_y(k+1)) \in \mathcal{R}_{\bar{x}_h^j}^{\xi_y,r_y}, \\ \forall\, (d_y(k), a_y(k)) \in (\mathcal{W}_y \times \Theta^{a_y}(r_y)), \quad (5.25)$$

where $\Theta^{a_y}(r_y)$ is the RAI set for reference CI set $\mathcal{R}^{r_y}$.

At time instant k, the predictive controller for controlling y_N and θ solves the on-line optimisation based on reference $\gamma_y^N(k) = (r_y(k), \cdots, r_y(k+N-1))$:

$$\begin{aligned} U_y^*(k) = &\arg\min_{U_y(k)} \sum_{i=0}^{N-1} \left(Q_y \left(y_e^*(k+i) - y_e(i|k) \right)^2 + \|i_y(i|k)\|_{R_y}^2 \right) \\ s.t.\ \ &\xi_y(i+1|k) = A_y(\bar{x}_h)\xi_y(i|k) + B_y(\bar{x}_h) i_y(i|k), \\ &y_e(i|k) = \begin{bmatrix} 1 & 0 & \bar{x}_h & 0 \end{bmatrix} \xi_y(i|k) - d, \\ &y_e^*(k+i) = \begin{bmatrix} 1 & 0 \end{bmatrix} r_y(k+i), \\ &\xi_y(i|k) \in \mathcal{R}_{\bar{x}_h^j}^{\xi_y,r_y}(\xi_y, r_y(k+i)),\ i \in \mathbb{Z}_{[0,N-1]}, j \in \mathbb{Z}_{[1,N_l]}, \\ &\xi_y(0|k) = \xi_y(k), \end{aligned} \quad (5.26)$$

where $\|i_y(i|k)\|_{R_y}^2 = i_y^T(i|k) R_y i_y(i|k)$; Q_y and R_y are the tuning weight on Y-axis position tracking error and control input respectively; $U_y^*(k) \triangleq \left(i_y^*(0|k), \cdots, i_y^*(N-1|k) \right)$. At each time instant, the optimal control $i_y(k) = i_y^*(0|k)$ is applied to the plant. The constraint of rotation angle θ, which is required in Remark 5.1, is guaranteed by enforcing the state ξ_y stays in the calculated RCI set.

5.4 Contouring error bounded control based on explicit contouring error

In this section, the second contouring error bounded controller is proposed. Instead of tightening the contouring error by reducing the tracking error of each axis, we propose a control algorithm with the explicit consideration of computed contouring error.

5.4.1 Problem formulation

In Cartesian space, the path to be tracked can be represented as:

$$f\left(x_e^*, y_e^*\right) = 0, \tag{5.27}$$

where x_e^* and y_e^* are the desired position of the end-effector in X and Y axes respectively.

Assumption 5.1. *The desired contour constraint function f is a finite group of straight line and circular contour.*

The given path (5.27) is parameterised with time dependency and the evolution of x_e^* and y_e^* are chosen as:

$$f\left(x_e^*(k), y_e^*(k)\right) = 0,\ k \in \mathbb{Z}_{0+}. \tag{5.28}$$

Based on the fact that the contouring error is only related to the shape of contour and the actual position of end-effector, the bounded contouring error requirement is represented as,

$$\epsilon\left(x_e(k), y_e(k)\right) \leq \epsilon_c,\ k \in \mathbb{Z}_{0+}, \tag{5.29}$$

where ϵ_c is the desired contouring tolerance. Then the problem of interest is formalised as,

Problem 5.1. *Consider the nonlinear system* (5.7), (5.8) *and* (5.9) *subjects to constraints* (5.21). *Given the reference in the form of* (5.28) *and a desired contouring tolerance $\epsilon_c \in \mathbb{R}_+$, if conditions* (5.21) *and* (5.29) *are satisfied initially, design a contouring controller to determine the multi-variable inputs $u_c(k) \triangleq (i_x(k), i_y(k))$ such that the closed loop system*

ensures (5.29) *for all* $k \in \mathbb{Z}_{0+}$ *and asymptotic convergence of the error* e_c *with* $e_c(k) \triangleq \|(x_e^*(k) - x_e(k), y_e^*(k) - y_e(k))\|_2$.

5.4.2 Feedback linearisation of coupling terms

Different from the contouring control method in Section 5.3, feedback linearisation is utilised first in computing the current command. By doing so, the nonlinearities in the model are cancelled, and a control-oriented model with smaller disturbance sets is obtained, thus reducing the conservativeness of the previous control method.

Let M_e' and k_x' be the nominal value of end-effector mass and X-axis force constant and by choosing

$$i_x = \frac{M_e'}{k_x'}\left(-x_h\dot{\theta}^2 + d\ddot{\theta} + \ddot{y}_N \sin\theta\right) + i_x', \tag{5.30}$$

the X-axis dynamic (5.7) is rewritten as,

$$M_e\ddot{x}_h + b_x\dot{x}_h = k_x i_x' + \eta_x, \tag{5.31}$$

where the lumped disturbance η_x includes the model mismatch and nonlinear coupling in the form,

$$\begin{aligned}\eta_x &= \left(\frac{k_x M_e'}{k_x'} - M_e\right)\left(-x_h\dot{\theta}^2 + d\ddot{\theta} + \ddot{y}_N \sin\theta\right) \\ &= \left(\frac{\Delta k_x M_e' - \Delta M_e k_x'}{k_x'}\right)\left(-x_h\dot{\theta}^2 + d\ddot{\theta} + \ddot{y}_N \sin\theta\right),\end{aligned}$$

where $M_e = M_e' + \Delta M_e$ and $k_x = k_x' + \Delta k_x$. The value of ΔM_e and Δk_x characterise the range of model mismatch.

Let Δx_h be the interval of the system be linearised and $x_h = \bar{x}_h + \delta x_h$ as demonstrated in Fig. 5.7, with the assumption $M_d = 0$ and the condition $|\delta x_h| \leq \Delta x_h$, the dynamics relating to coordinate y_N (5.8) are rewritten as,

$$\begin{aligned}M_t\ddot{y}_N + 2b_y\dot{y}_N + M_e\bar{x}_h\ddot{\theta} = k_y i_{y1} - M_e\Big(&\sin\theta\ddot{x}_h + d\sin\theta\ddot{\theta} - x_h\sin\theta\dot{\theta}^2 + 2\dot{x}_h\cos\theta\dot{\theta} \\ &+ d\dot{\theta}^2\cos\theta\Big) - M_e\delta x_h\ddot{\theta},\end{aligned}$$

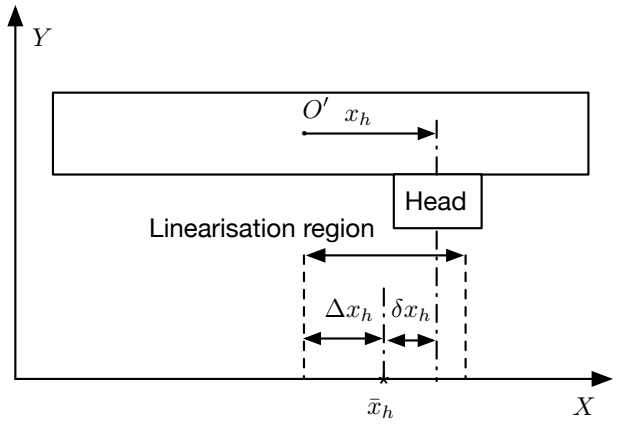

Fig. 5.7: Approach for linear modelling of axis. Here x_h is the position of head, $\bar{x}_h$ is the linearisation point, Δx_h characterises half length of the linearisation region, δx_h is the deviation from x_h to $\bar{x}_h$.

where $i_{y1} = i_1 + i_2$ and $\dot{y}_N = (\dot{y}_1 + \dot{y}_2)/2$.

By choosing the input i_{y1} as

$$i_{y1} = \frac{M_e'}{k_y'}(\sin\theta\ddot{x}_h + d\sin\theta\ddot{\theta} - x_h\sin\theta\dot{\theta}^2 + 2\dot{x}_h\cos\theta\dot{\theta} + d\dot{\theta}^2\cos\theta) + i_{y1}', \tag{5.32}$$

we have

$$M_t\ddot{y}_N + 2b_y\dot{y}_N + M_e\bar{x}_h\ddot{\theta} = k_{y1}i_{y1}' + \eta_{y1}, \tag{5.33}$$

where the lumped disturbance η_{y1} is in the form,

$$\begin{aligned}\eta_{y1} =&(\frac{k_yM_e'}{k_y'} - M_e)(\sin\theta\ddot{x}_h + d\sin\theta\ddot{\theta} - x_h\sin\theta\dot{\theta}^2 + 2\dot{x}_h\cos\theta\dot{\theta} + d\dot{\theta}^2\cos\theta) - M_e\delta x_h\ddot{\theta}\\ =&(\frac{\Delta k_yM_e' - \Delta M_ek_y'}{k_y'})(\sin\theta\ddot{x}_h + d\sin\theta\ddot{\theta} - x_h\sin\theta\dot{\theta}^2 + 2\dot{x}_h\cos\theta\dot{\theta} + d\dot{\theta}^2\cos\theta)\\ &- M_e\delta x_h\ddot{\theta},\end{aligned}$$

where $k_y = k_y' + \Delta k_y$.

Similarly, the dynamics relate to the coordinate θ, i.e., (5.9), are rewritten as,

$$\begin{aligned}M_e\bar{x}_h\ddot{y}_N + J(\bar{x}_h)\ddot{\theta} + 2b_yL^2\dot{\theta} + 2k_r\theta =&k_yLi_{y2} - M_e\left(d\ddot{x}_h + d\sin\theta\ddot{y}_N + 2\dot{\theta}\dot{x}_hx_h\right)\\ &- M_e\delta x_h\ddot{y}_N - 2M_e\bar{x}_h\delta x_h\ddot{\theta} - M_e\delta x_h^2\ddot{\theta},\end{aligned}$$

where $i_{y2} = i_2 - i_1$. By choosing the i_{y2} as,

$$i_{y2} = \frac{M'_e}{k'_y L}\left(d\ddot{x}_h + d\sin\theta\ddot{y}_N + 2\dot{\theta}\dot{x}_h x_h\right) + i'_{y2}, \tag{5.34}$$

we have

$$M_e\bar{x}_h\ddot{y}_N + J(\bar{x}_h)\ddot{\theta} + 2b_y L^2\dot{\theta} + 2k_r\theta = k_y L i'_{y2} + \eta_{y2}, \tag{5.35}$$

where the lumped disturbance η_{y2} is in the form,

$$\begin{aligned}\eta_{y2} =&(\frac{k_y M'_e}{k'_y} - M_e)(d\ddot{x}_h + d\sin\theta\ddot{y}_N + 2\dot{\theta}\dot{x}_h x_h) - M_e\delta x_h\ddot{y}_N - 2M_e\bar{x}_h\delta x_h\ddot{\theta} - M_e\delta x_h^2\ddot{\theta}\\ =&(\frac{\Delta k_y M'_e - \Delta M_e k'_y}{k'_y})(d\ddot{x}_h + d\sin\theta\ddot{y}_N + 2\dot{\theta}\dot{x}_h x_h) - M_e\delta x_h\ddot{y}_N - 2M_e\bar{x}_h\delta x_h\ddot{\theta}\\ &- M_e\delta x_h^2\ddot{\theta}.\end{aligned}$$

Then the discrete-time state space model for the X and Y axes can be derived from (5.31), (5.33) and (5.35) with given sampling time T_s as,

$$\begin{aligned}\xi_x(k+1) &= A_x\xi_x(k) + B_x i'_x(k) + E_x\eta_x(k),\\ \xi_y(k+1) &= A_{y2}(\bar{x}_h)\xi_y(k) + B_{y2}(\bar{x}_h)i'_y(k) + E_{y2}(\bar{x}_h)\eta_y(k),\end{aligned}$$

where $\xi_x \triangleq (x_h, \dot{x}_h)$ and $\xi_y \triangleq \left(y_N, \dot{y}_N, \theta, \dot{\theta}\right)$ are the states; i'_x and $i'_y \triangleq \left(i'_{y1}, i'_{y2}\right)$ are the inputs; $\eta_y \triangleq (\eta_{y1}, \eta_{y2})$ is the disturbance vector. Note that A_x, B_x and E_x here are same as in (5.19). Let $\xi_c \triangleq \left(x_h, \dot{x}_h, y_N, \dot{y}_N, \theta, \dot{\theta}\right)$ be the states, the state space model of entire system is,

$$\xi_c(k+1) = A_c(\bar{x}_h)\xi_c(k) + B_c(\bar{x}_h)i'(k) + E_c(\bar{x}_h)\eta(k), \tag{5.36}$$

where $i' \triangleq (i'_x, i'_y)$ and $\eta \triangleq (\eta_x, \eta_y)$. The states and inputs have operational constraints

$$\xi_c \in \mathcal{X}_c \subseteq \mathbb{R}^6,\ i' \in \mathcal{U}_c \subseteq \mathbb{R}^3.$$

With the knowledge of potential parameter mismatch range, the constraints of states and inputs (5.21) can be used to determine the bounds of disturbance. The compact

disturbance set is represented as $\eta \in \mathcal{W}_c \subseteq \mathbb{R}^3$.

5.4.3 Computation of robust control invariant set

Linear contour

For linear contour with the form $f\left(x_e^*, y_e^*\right) = ax_e^* + by_e^* + c$, the contouring error is

$$\epsilon\left(x_e, y_e\right) = \frac{|ax_e + by_e + c|}{\sqrt{a^2 + b^2}}.$$

Then, the requirement of bounded contouring error is represented as

$$\epsilon\left(x_h, y_N, \theta\right) = \frac{|a(x_h + d\theta) + b(y_N + \bar{x}_h\theta - d) + c|}{\sqrt{a^2 + b^2}} \leq \epsilon_c. \tag{5.37}$$

For linear contour that covers N_q linearisation points, we start by defining a set of system states to ensure $\epsilon \leq \epsilon_c$,

$$\mathcal{S}_l^q = \left\{ \xi_c \in \mathbb{R}^6 | \, \frac{|a\left(x_h + d\theta\right) + b\left(y_N + \bar{x}_h^q\theta - d\right) + c|}{\sqrt{a^2 + b^2}} \leq \epsilon_c \right\}, \, q \in \mathbb{Z}_{[\dot{q}, \dot{q}+N_q-1]}, \tag{5.38}$$

where $\bar{x}_h^q$ with value $q \in \mathbb{Z}_{[\dot{q}, \dot{q}+N_q-1]}$ specify the involved linearisation point as shown in Fig. 5.8.

The sets characterised by (5.38) are convex and can be represented by a finite number of inequalities. These sets are used later to compute the RCI set for ensuring bounded contouring error. It has to be noticed that the sets $\mathcal{S}_l^q$ are not related to the states of the reference model.

Circular contour

For circular contour with form $f\left(x_e^*, y_e^*\right) = \left(x_e^* - x_o\right)^2 + \left(y_e^* - y_o\right)^2 - R_c^2$, the contouring error is:

$$\epsilon(x_e, y_e) = \left| R_c - \sqrt{(x_e - x_o)^2 + (y_e - y_o)^2} \right|.$$

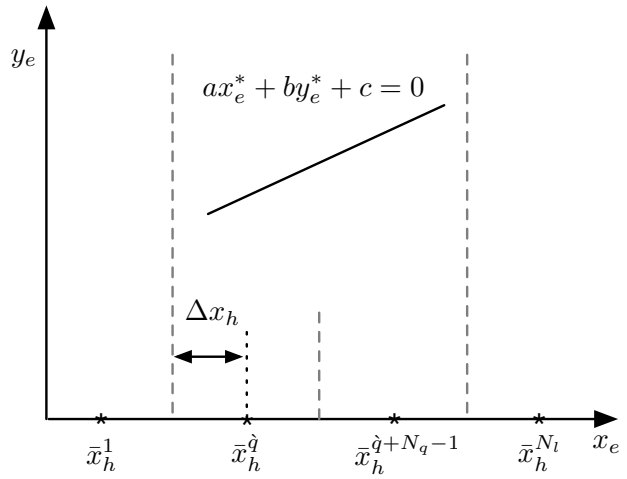

Fig. 5.8: Schematic diagram of linear contour and linearisation region, where the star symbol shows the linearisation point.

Then, the requirement of bounded contouring error is represented as,

$$\epsilon\left(x_e, y_e\right) = \left| R_c - \sqrt{(x_e - x_o)^2 + (y_e - y_o)^2} \right| \leq \epsilon_c. \tag{5.39}$$

This inequality corresponds to a feasible set $\mathcal{S}_c^{\xi_c}$ shown in Fig. 5.9a, which is non-convex and not applicable for computing the corresponding RCI set directly. To solve this problem, the set approximation and partitioning is conducted.

At first, the smallest inner regular polygon (an outer approximation of inner circle) and the largest outer regular polygon (an inner approximation of outer circle) are found as demonstrated in Fig. 5.9b.

Let n_{in} and n_{out} be the side number of inner and outer polygons respectively, e.g., in the example of Fig. 5.9b, $n_{in} = 6$ and $n_{out} = 8$, the feasible set $\mathcal{S}_c^{\xi_c}$ is approximated by the area between the two polygons $\hat{\mathcal{S}}_c^{\xi_c}$ and is partitioned into n_{in} numbers of convex sets:

$$\hat{\mathcal{S}}_c^{\xi_c} = \bigcup_{i=1}^{n_{in}} S_c^i,$$

where S_c^i are convex sets. This estimated feasible set $\hat{\mathcal{S}}_c^{\xi_c}$ can be represented by $n_{in} + n_{out}$ numbers of inequalities.

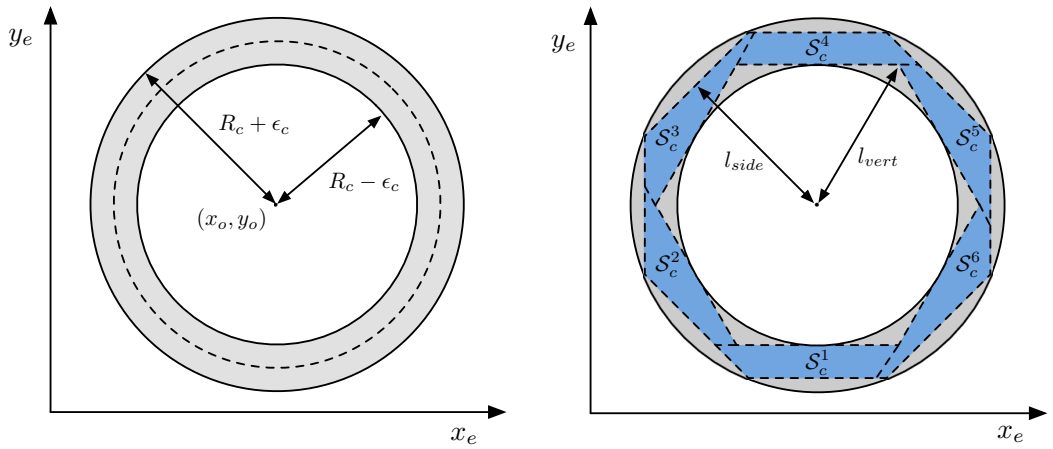

Fig. 5.9: Example of feasible sets for bounded contouring error: (a) non-convex set $\mathcal{S}_c^{\xi_c}$ (grey shaded area) and desired contour (dot line); (b) approximated sets with partitioned polygons in blue shaded area.

Let the distance from the circular centre to the vertices of inner polygon, to the side of outer polygon be l_{vert} and l_{side} respectively. Once the contour radius R_c and desired contour tolerance ϵ_c are given, the value of l_{vert} and l_{side} are related to the side number of inner and outer polygons and can be computed as,

$$l_{vert} = \frac{R_c - \epsilon_c}{\cos\left(\pi / n_{in}\right)},$$

$$l_{side} = \left(R_c + \epsilon_c\right) \cos \frac{\pi}{n_{out}}.$$

Since the estimated feasible set $\hat{\mathcal{S}}_c^{\xi_c}$ will be used for subsequent RCI set computation, the number of inequalities used for set approximation, i.e. $n_{in} + n_{out}$ directly influences the complexity of the corresponding RCI set. At the same time, in order to obtain a feasible RCI set, constraints $l_{vert} \leq R_c$ and $l_{vert} \leq l_{side}$ should hold. To reduce the online computation burden when implementing the MPC with RCI set constraints, we would like to solve the optimisation problem as follows:

$$\arg \min_{n_{in}, n_{out}} \; n_{in} + n_{out} \tag{5.40}$$

$$s.t. \frac{R_c - \epsilon_c}{\cos\left(\pi / n_{in}\right)} \leq R_c, \tag{5.41}$$

$$\frac{R_c - \epsilon_c}{\cos\left(\pi/n_{in}\right)} \leq (R_c + \epsilon_c)\cos\frac{\pi}{n_{out}}. \tag{5.42}$$

Considering the constraint (5.41) is independent of n_{out}, a sub-optimal algorithm is conducted as Algorithm 2. It starts with determining the minimum $\bar{n}_{in}$ based on (5.41) with given R_c and ϵ_c. Then a suitable number of $\bar{n}_{out}$ is chosen to ensure a feasible group of RCI sets can be obtained.

Algorithm 2 Computation of side numbers of inner and outer polygons

1: *Input*: R_c and ϵ_c
2: *Output*: $\bar{n}_{in}$ and $\bar{n}_{out}$
3: Compute $\bar{n}_{in}$ based on:

$$\bar{n}_{in} = \arg\min_{n_{in}} n_{in} \quad s.t.\ \frac{R_c - \epsilon_c}{\cos\left(\pi/n_{in}\right)} \leq R_c$$

4: Compute $\bar{n}_{out}$ based on:

$$\bar{n}_{out} = \arg\min_{n_{out}} n_{out} \quad s.t.\ \frac{R_c - \epsilon_c}{\cos\left(\pi/\bar{n}_{in}\right)} \leq (R_c + \epsilon_c)\cos\frac{\pi}{n_{out}}$$

5: **if** $\{(x_e^*, y_e^*) | \, (x_e^* - x_o)^2 + (y_e^* - y_o)^2 = R_c^2\} \subseteq \hat{\mathcal{S}}_c^{\xi_c}$ **then**
6: **return** $\bar{n}_{in}$ and $\bar{n}_{out}$
7: **else**
8: $\bar{n}_{out} \leftarrow \bar{n}_{out} + 1$
9: **go to** 5
10: **end if**

Once $\bar{n}_{in}$ and $\bar{n}_{out}$ are determined, the partitioned polygons $\mathcal{S}_c^i$ are used to compute the RCI based on switched LTI system dynamics (5.36). Since the system dynamics is linearised at different points $\bar{x}_h$, the feasible set $\mathcal{S}_c^i$ may cover several regions where the system is linearised. Let N_i be the numbers of linearisation region the set $\mathcal{S}_c^i$ covers and $\bar{x}_h^j$ be the linearisation point involved for $j \in \mathbb{Z}_{[p_i, p_i+N_i-1]}$, the schematic diagram of partitioned feasible set and linearised region is shown in Fig. 5.10 where $N_1 = 2$ for $\mathcal{S}_c^1$.

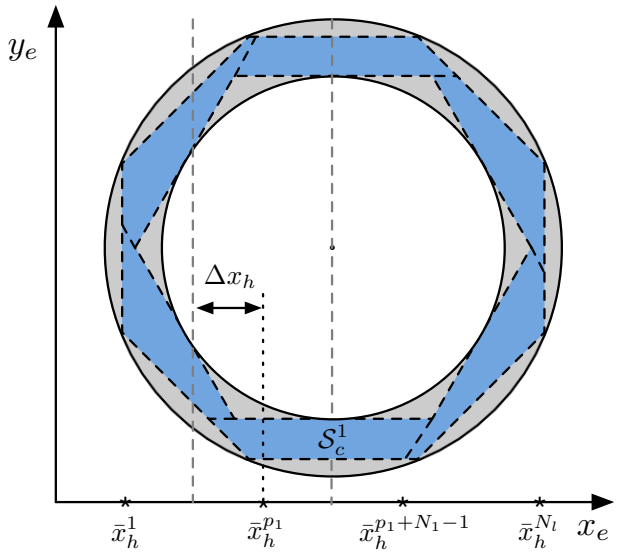

Fig. 5.10: Partitioned feasible sets and the linearised region (area between dot grey lines) where the star symbols stand for the linearisation points.

RCI set for contouring error bounded control

Let the RCI set corresponding to set $\mathcal{S}_l^q$ with system dynamics linearised at $\bar{x}_h^q$ be $\mathcal{R}_l^q$ and the RCI set corresponding to set $\mathcal{S}_c^i$ with system dynamics linearised at $\bar{x}_h^j$ be $\mathcal{R}_c^{i,j}$ for $q \in \mathbb{Z}_{[\dot{q},\dot{q}+N_q-1]}$, $i \in \mathbb{Z}_{[1,\bar{n}_{in}]}$ and $j \in \mathbb{Z}_{[p_i,p_i+N_i-1]}$. Given the feasible set $\mathcal{S}_l^q$ and $\mathcal{S}_c^i$ for linear and circular contour, and the system dynamics (5.36), the algorithm for computing the RCI set $\mathcal{R}^{\xi_c} = \left\{\mathcal{R}_l^q, \mathcal{R}_c^{i,j}\right\}$ for contouring error bounded control is proposed as Algorithm 3.

Proposition 5.1. *The computed set $\mathcal{R}_{m+1}^{\xi_c}$ is an RCI set for ensuring bounded contouring error.*

Proof. The proof to show $\mathcal{R}_{m+1}^{\xi_c}$ is an RCI set is similar to the proof for Algorithm 1 with appropriate modification, and is thus omitted here. □

Here, two characteristics of Algorithm 3 should be noticed:

1. The evolution of reference states are not required when computing the RCI set considering the contouring error is independent of the reference.

2. When computing the RCI sets for circular contour, the system dynamics is position-dependent, and this may lead to more than one RCI set corresponding to $\mathcal{S}_c^i$ if more than

Algorithm 3 RCI set computation for contouring error bounded control

Initialisation:
$m \leftarrow 0$, $\mathcal{R}_0^{\xi_c} \leftarrow \mathcal{R}_s^{\xi_c} \cap \bar{\mathcal{R}}_0^{\xi_c}$, where
$\mathcal{R}_s^{\xi_c} \leftarrow \left\{\xi_c \in \mathbb{R}^6 \,|\, \xi_c \in \mathcal{X}_c,\, \bar{x}_h - \frac{\Delta x_h}{2} \leq x_h \leq \bar{x}_h + \frac{\Delta x_h}{2}\right\}$, for $\bar{x}_h = \left\{\bar{x}_h^q, \bar{x}_h^j\right\}$
$\bar{\mathcal{R}}_0^{\xi_c} \leftarrow \left\{\xi_c \in \mathbb{R}^6 \,|\, \xi_c \in \left\{\mathcal{S}_l^q, \mathcal{S}_c^i\right\}\right\}$, $q \in \mathbb{Z}_{[\dot{q}, \dot{q}+N_q-1]}$, $i \in \mathbb{Z}_{[1,\bar{n}_{in}]}$, $j \in \mathbb{Z}_{[p_i, p_i+N_i-1]}$.
Iteration:
$\mathcal{R}_{m+1}^{\xi_c} \leftarrow \mathcal{R}_s^{\xi_c} \cap \bar{\mathcal{R}}_{m+1}^{\xi_c}$, where $\bar{\mathcal{R}}_{m+1}^{\xi_c} \leftarrow \hat{D}\left(\bar{\mathcal{R}}_m^{\xi_c}, \rho\right) \cap \bar{\mathcal{R}}_m^{\xi_c}$,

$$\hat{D}\left(\bar{\mathcal{R}}_m^{\xi_c}, \rho\right) \leftarrow \{\xi_c \in \mathbb{R}^n \,|\, \exists_{i' \in \mathcal{U}_c}, A_c(\bar{x}_h)\xi_c + B_c(\bar{x}_h)i' + E_c(\bar{x}_h)\eta \in \bar{\mathcal{R}}_m^{\xi_c} - \mathbb{B}^6(\rho), \forall \eta \in \mathcal{W}_c\}.$$

if $\mathcal{R}_m^{\xi_c} - \mathbb{B}^6(\rho) \subseteq \mathcal{R}_{m+1}^{\xi_c}$ **then**
    return $\mathcal{R}^{\xi_c} = \left\{\mathcal{R}_l^q, \mathcal{R}_c^{i,j}\right\} \leftarrow \mathcal{R}_{m+1}^{\xi_c}$
else
    $m \leftarrow m + 1$
    go to 4
end if

one linearisation region is overlapped with $\mathcal{S}_c^i$. In total, there are $N_q + \sum_{i=1}^{\bar{n}_{in}} N_i$ number of RCI sets need to be computed offline for guaranteeing the contouring error bound.

5.4.4 Model predictive based controller formulation

Let the term $y_c \triangleq (x_e, y_e + d)$ and $r_c = (x_e^*, y_e^* + d)$ stand for the output and reference respectively. Assume the N-step reference ($N \in \mathbb{Z}_+$), $\gamma_c^N(k) = (r_c(k), \ldots, r_c(k+N-1))$, is known. The controller ensuring bounded contouring error and convergence of tracking error is required to solve the following optimisation problem at each time instant:

$$\begin{aligned} U_c^*(k) = &\arg\min_{U_c(k)} \sum_{i=0}^{N-1} \left(\|y_c(i|k) - r_c(k+i)\|_{Q_o}^2 + \left\|i'(i|k)\right\|_{R_o}^2\right) + \|y_c(N|k) - r_c(k+N)\|_{P_o}^2 \\ s.t.\ &\xi_c(i+1|k) = A_c(\bar{x}_h)\xi_c(i|k) + B_c(\bar{x}_h)i'(i|k), \\ &y_c(i|k) = C_c\xi_c(i|k), \\ &\xi_c(i|k) \in \mathcal{R}^{\xi_c}\left(\xi_c(k), r_c(k)\right), i \in \mathbb{Z}_{[0,N-1]}, \\ &\xi_c(0|k) = \xi_c(k). \end{aligned} \tag{5.43}$$

Here, $U_c^*(k) = (i'^*(0|k), \ldots, i'^*(N-1|k))$. The total current command is generated by addition of the feedback linearisation term, i.e.,

$$i_t(k) = i'^*(0|k) + i_f(k), \tag{5.44}$$

where $i_t \triangleq (i_x^*, i_{y1}^*, i_{y2}^*)$ and the feedback linearisation term i_f can be inferred from (5.30), (5.32) and (5.34). The current command of Y-axis motors is then computed as $i_1^* = (i_{y1}^* - y_{y2}^*)/2$ and $i_2^* = (i_{y1}^* + i_{y2}^*)/2$. The explicit form of output matrix C_c is,

$$C_c = \begin{bmatrix} 1 & 0 & 0 & 0 & d & 0 \\ 0 & 0 & 1 & 0 & \bar{x}_h & 0 \end{bmatrix}.$$

The term $\mathcal{R}^{\xi_c}(\xi_c(k), r_c(k))$ in (5.43) means the applied RCI set is related to reference and system state at time instant k. The value of $r_c(k)$ determines whether the RCI element $\mathcal{R}_l^q$ or $\mathcal{R}_c^{i,j}$ is used, and the value of $\xi_c(k)$ decides which element, i.e., the value of q , i and j for $q \in \mathbb{Z}_{[\dot{q}, \dot{q}+N_q-1]}$, $i \in \mathbb{Z}_{[1,\bar{n}_{in}]}$ and $j \in \mathbb{Z}_{[p_i, p_i+N_i-1]}$, is used in the controller formulation.

The Q_o and R_o are the tuning parameters to penalise the tracking error and control effort. The value of P_o is chosen based on the following remark.

Remark 5.2. *Once we have $\grave{Q} = C_c^T Q_o C_c$ and $\grave{P} = C_c^T P_o C_c$, the cost function in the* (5.43) *is equivalent to the form of MPC formulation in [102], with the steady state $\xi_d = (x_e^*, 0, y_e^* + d, 0, 0, 0)$ and steady input $i_d = (0, 0, 0)$.*

With the chosen Q_o and R_o, the value $\grave{Q}$ is computed as $\grave{Q} = C_c^T Q_o C_c$. As described in [102], the positive definite matrix $\grave{P}$ is a solution of equation

$$(A_c + B_c K_c)^T \grave{P} (A_c + B_c K_c) - \grave{P} = -(\grave{Q} + K_c^T R_c K_c),$$

where K_c is a stablising control gain such that $(A_c + B_c K_c)$ is Hurwitz. The weighting matrix P_o is computed as $P_o = (C_c C_c^T)^{-1} C_c \grave{P} C_c^T (C_c C_c^T)^{-1}$.

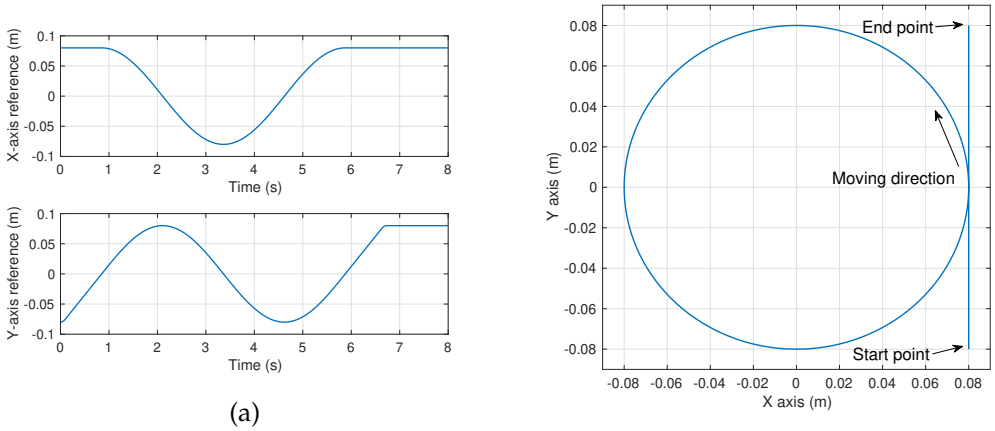

(a) (b)

Fig. 5.11: Desired reference: (a) time-dependent trajectory in X and Y axes; (b) contour.

5.5 Simulation results of contouring control methods

To evaluate the effectiveness of the two proposed methods, contouring control simulation based on the high-fidelity model identified in Section 5.2 is conducted. The end-effector is required to follow a contour consisting of a circular path with centre at $(0, 0)$ and 0.08 m radius and a straight line part for acceleration and deceleration with the maximum velocity at 0.1 m/s and maximum acceleration at 1 m/s^2. The desired path and trajectory on X and Y axes are shown in Fig. 5.11.

The desired contouring error bound is chosen as 4 mm, corresponding to 5% of the radius of the circular part of trajectory. Considering the computation load for biaxial control is higher than single-axis tracking control, the controller is updated at 2 ms and the data sampling rate is chosen as 0.25 ms.

5.5.1 CEBC based on bounded tracking error

The contouring control method proposed in Section 5.3 is tested first. In order to guarantee the 4 mm contouring error bound, the upper bound of X and Y-axis tracking error is chosen as $\epsilon_x = 2$ mm and $\epsilon_y = 2$ mm. The upper bound of rotation angle is chosen as $\theta_{max} = 0.0025$ rad and this gives $\bar{\epsilon}_x = 1.5$ mm.

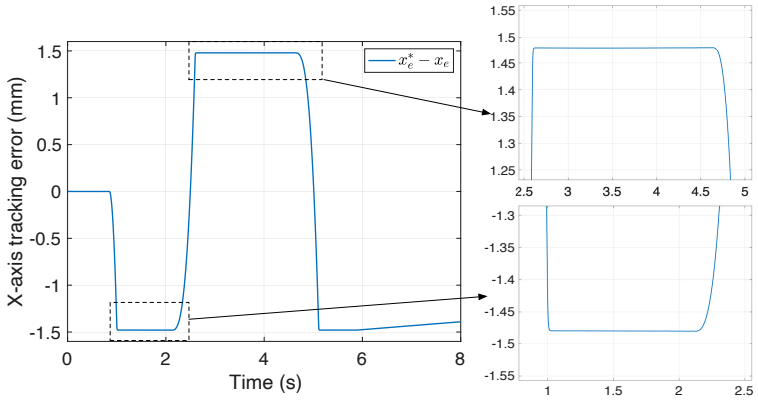

Fig. 5.12: Simulated X-axis end-effector tracking error.

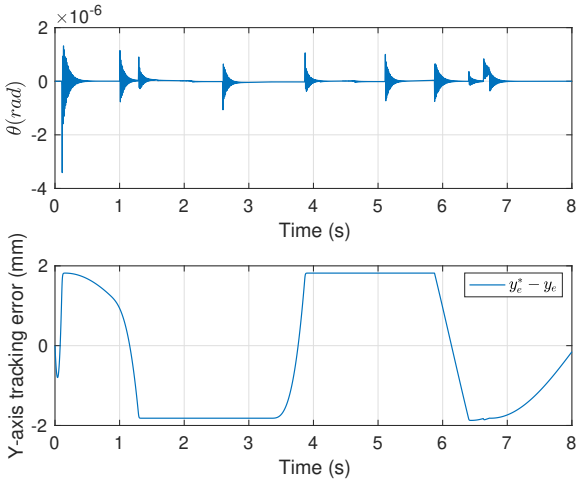

Fig. 5.13: Simulated rotation angle (up) and Y-axis tracking error (down).

For the Y-axis control, the switching LTI model (5.20) is linearised at point $\bar{x}_h = \{-0.075, -0.025, 0.025, 0.075\}$ m with $\Delta x_h = 0.025$ m to achieve a trade-off between the accuracy of the control-oriented model and numbers of controller switching. The weighting parameters in the MPC cost function (5.23) and (5.26) are chosen as $Q_x = Q_y = 10^5$, $R_x = 0.1$ and R_y is chosen as a scalar matrix with multiple 0.1 to put more weight on the tracking errors.

The tracking error of end-effector on X axis $x_e^* - x_e$ is shown in Fig. 5.12 with the maximum absolute value as 1.48 mm. The value of rotation angle and tracking error of Y axis $y_e^* - y_e$ are demonstrated in Fig. 5.13. It can be seen that the rotation angle is

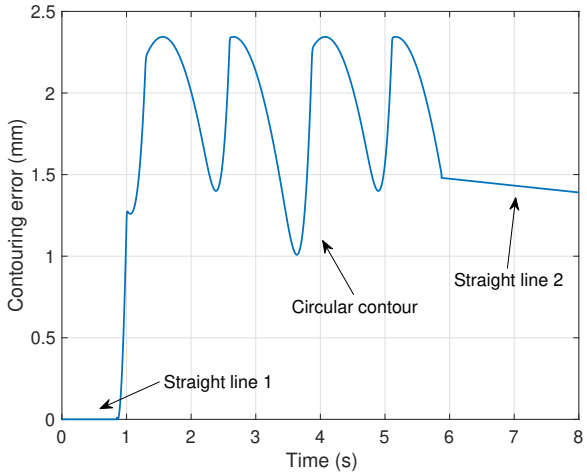

Fig. 5.14: Contouring error during the whole process based on CEBC with bounded tracking error.

much smaller compared to the desired tolerance, i.e., $\theta \ll \theta_{max} = 0.0025$ rad, and the tracking error on Y axis is within the 2 mm tolerance.

Since the entire path only consists of straight line and circle, the contouring error can be directly calculated and is illustrated in Fig. 5.14. The maximum contouring error is 2.34 mm, which is below the specified error tolerance and is around 2.92% of the circle radius.

On the first straight line segment, the non-zero tracking error on Y axis leads to a zero contouring error. This is due to the fact that the end-effector starts on the contour and there is no displacement on the X axis.

While on the circular path, during 1 to 2 seconds, the X-axis tracking error is constant around 1.5 mm, however, the Y-axis tracking error changes from around $+0.9$ to -1.8 mm as seen in Fig. 5.12 and Fig. 5.13. The corresponding contouring error, therefore, passes through a minimum shortly after 1 seconds. Although the tracking error on both axes is constant through next 0.78 seconds, when the mapped contour is projected and it results in the decreasing contouring error from 1.6 to 2.1 seconds, before the X-axis tracking error increases again. This pattern continues for the rest of the circular contour.

On the last straight line segment, the tracking error on X axis maps directly to con-

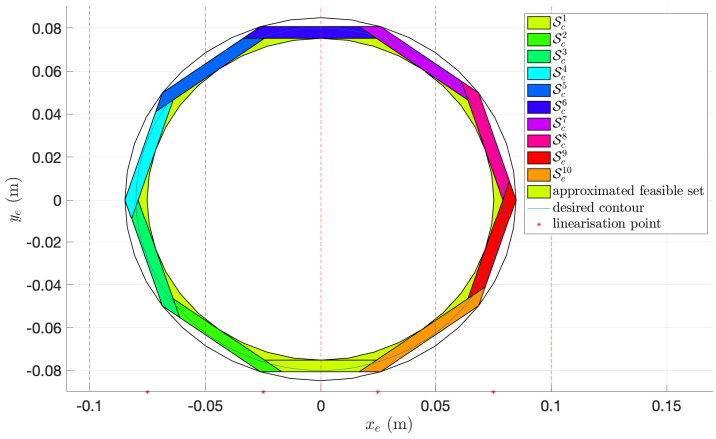

Fig. 5.15: Feasible sets for bounded contouring error.

touring error. The simulation results demonstrate the ability of the proposed controller in meeting a specified contouring error requirement for a system with position-dependent flexibility.

5.5.2 CEBC based on computed contouring error

To achieve the contouring error bounded control with tolerance 4 mm, the method proposed in Section 5.4 starts by choosing the number of inner polygon based on (5.41). The values $\bar{n}_{in} = 10$ and $\bar{n}_{out} = 10$ are determined by Algorithm 2. The switched LTI model (5.36) is linearised at points $\bar{x}_h = \{-0.075, -0.025, 0.025, 0.075\}$ m as previously, and 10 feasible sets for circular contour are found and shown in Fig. 5.15. We started by indexing the RCI set corresponding to $\mathcal{S}_c^1$ at linearisation point $\bar{x}_h = -0.025$ m as Set 1, and did the subsequent computation clockwise as shown in Fig. 5.15 for all the RCI sets until Set 16. The RCI set for linear contour is computed based on the model linearised at $\bar{x}_h^4 = 0.075$ m and is represented as $\mathcal{R}_l^4$ for $q = 4$.

The tuning weights in MPC formulation (5.43) are chosen as $Q_o = diag(10^5, 10^5)$ and $R_o = diag(10^{-1}, 10^{-3}, 10^2)$ to emphasise more weight on tracking errors. The value of P_o is computed based on the Remark 5.2. The contouring error bound is guaranteed by ensuring the system state ξ_c within the group of RCI set $\mathcal{R}^{\xi_c}$.

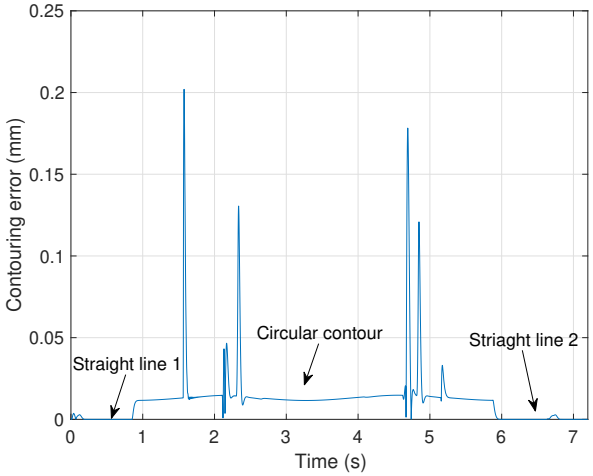

Fig. 5.16: Contouring error based on CEBC with explicitly computed contouring error.

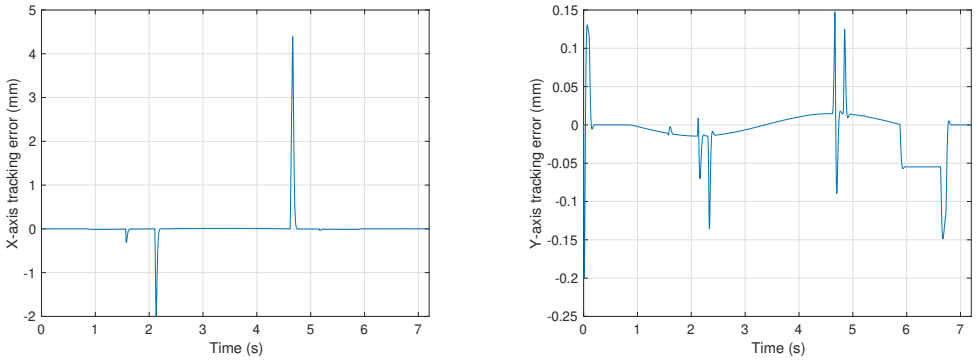

(a) (b)

Fig. 5.17: End-effector tracking error by using CEBC with explicitly computed contouring error: (a) X-axis tracking error; (b) Y-axis tracking error.

The contouring error during the whole process is computed and demonstrated in Fig. 5.16. The maximum contouring error is 0.202 mm, which is within the error tolerance and smaller than the maximum error achieved by CEBC based on bounded tracking error. This is due to the fact that the approximated feasible set $\hat{\mathcal{S}}_c^{\xi_c}$ is used for RCI set computation, which leads to a group of more conservative RCI sets.

In addition, the tracking errors on X and Y axes are computed and given in Fig. 5.17 to offer more information about the performance of the proposed controller.

Similar to the trend presented in Fig. 5.14, the contouring error shown in Fig. 5.16

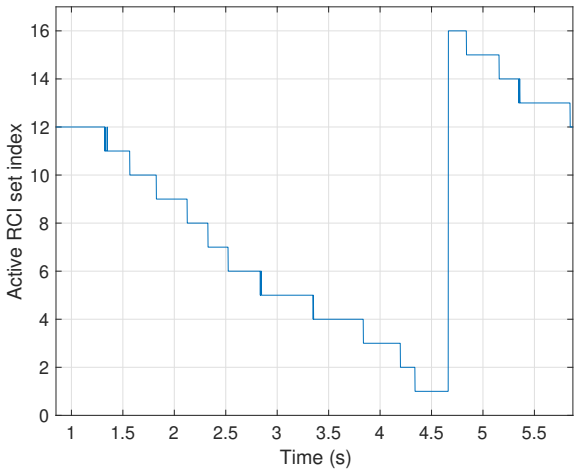

Fig. 5.18: Active RCI set when the end-effector moves along circular contour.

is related to the three segments of the path. On the first straight line segment, the contouring error is close to zero due to small displacement in the X axis.

During the circular contour segment, the change of velocity on X axis results in spike tracking error and indeed leads to contouring error.

In the last straight line part, although the tracking error on Y axis exists, the contouring error is close to zero due to the existence of a small X-axis tracking error. In addition, it is interesting to see that although the X-axis tracking error is above 4 mm, the contouring error is much smaller than the desired tolerance.

The index of active RCI set is given in Fig. 5.18. This offers the information about the time and which RCI is activated when the end-effector moves. For the region where two RCI sets are overlapped, the active RCI set switches between the two sets and only the control output results in the lowest cost is applied.

5.6 Experiment results

To validate the contouring control performance of the proposed methods, the experimental contouring control is conducted. However, due to the fact that there is no direct position measurement of end-effector on the laser machine, we build a back-to-back mo-

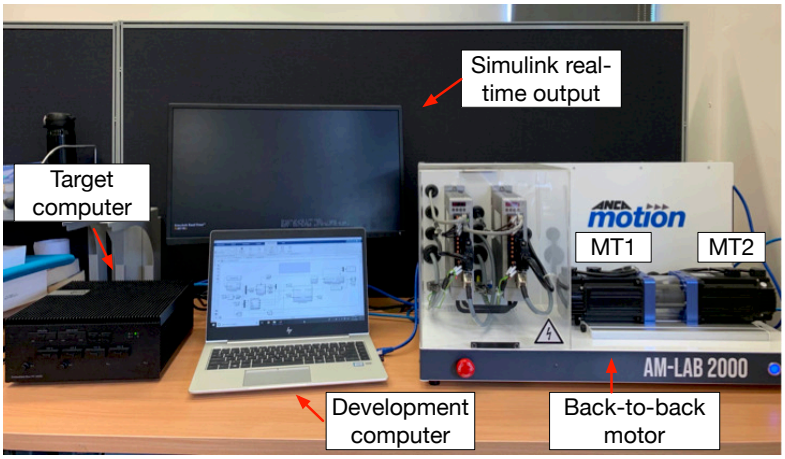

Fig. 5.19: Experimental test bench for contouring control.

tor based test bench, and the contouring control is implemented in a hardware-in-loop configuration as described later. Moreover, due to hardware limitation, only the CEBC method based on bounded tracking error is implemented.

5.6.1 Experiment setup

The entire experiment setup is shown as Fig. 5.19, which consists of a development computer, target computer and two back-to-back motors. The Simulink Real-Time environment is used for controller implementation.

The designed test bench 'AM-Lab 2000' includes two back-to-back rotary motors with the same specification and two separate control drives. By properly generating the current command for the motor MT2, this test bench can be used to represent the dynamics of (5.7). With the rotary to translational unit conversion, the feedback of motor MT1 is used to represent the position measurement of laser head along the X' axis, i.e., x_h.

The dynamics of the back-to-back motor can be represented as:

$$J_A\ddot{\theta}_h = k_A i_x - b_r\dot{\theta}_h - F_L - F_{fn}, \tag{5.45}$$

where J_A is the total moment of inertial including two motors and the coupling part;

θ_h is the rotary angle of motor MT1; k_A is the force constant of the motors; b_r is the rotary viscous friction coefficient; F_L is the load torque imposed on the motor MT1 with expression $F_L = k_A i_T$; F_{fn} is the nonlinear component of friction.

With the unit conversion $\theta_h \triangleq \frac{x_h}{r_A}$, where r_A is the radius of the motor shaft, the dynamics (5.45) is rewritten as:

$$\ddot{x}_h = \frac{k_A}{M_A} i_x - \frac{b_A}{M_A} \dot{x}_h - \frac{F_L}{M_A} - \frac{F_{fn}}{M_A},$$

where $M_A \triangleq \frac{J_A}{r_A}$ is the equivalent total mass and $b_A \triangleq \frac{b_r}{r_A}$ is the viscous friction coefficient for the translational movement.

By choosing the current command of motor MT2 as

$$i_T^* = F_L^*/k_A = \frac{M_A}{k_A} \left(\left(\frac{k_A}{M_A} - \frac{k_x}{M_e} \right) i_x - \left(\frac{b_A}{M_A} - \frac{b_x}{M_e} \right) \dot{x}_h - d_x \right), \tag{5.46}$$

where i_T^* is the current command of motor MT2 and F_L^* is the command of load toque.

Then the dynamics of test bench would be:

$$\ddot{x}_h = \frac{k_x}{M_e} i_x - \frac{b_x}{M_e} \dot{x}_h + d_x - \frac{F_{fn}}{M_A}. \tag{5.47}$$

This test bench is used with the simulated model (5.8) and (5.9) as the plant for later contouring control.

5.6.2 Input delay in test bench

Before we implement the proposed method on the plant for contouring control, we did the test of current command tracking first, and the result is shown as Fig. 5.20.

The communication rate between the target PC and servo drive is set at 4 kHz, and a cascaded controller is implemented at the drive level for current tracking. The servo drive has an intrinsic cycle time of 1 ms, and this means if there is no delay, it takes 1 ms for the current feedback to respond after the drive receiving the command change.

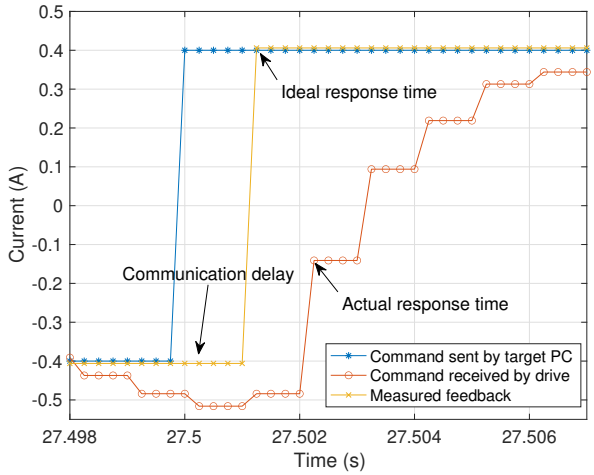

Fig. 5.20: Closed-loop response of current loop on motor MT1.

However, it can be seen from Fig. 5.20 that there is another 1 ms communication delay between the target PC and servo drive. This may be due to the setting of the firmware provided and cannot be avoided at the time doing the experiment.

Therefore, if the controller is updated every 2 ms, there is one sample delay of the input and this should be considered in the controller design.

5.6.3 Modified control-oriented model

In this section, we require the end-effector to traverse the same reference shown in Fig. 5.11.

Since there is one sample delay in the current loop feedback, the dynamics of test bench in discrete time with sampling T_s is indeed:

$$\dot{x}_h(k+1) = \frac{T_s k_A}{M_A} i_x(k-1) + \left(1 - \frac{T_s b_A}{M_A}\right) \dot{x}_h(k) - \frac{T_s F_L(k-1)}{M_A} - \frac{T_s F_{fn}(k)}{M_A}.$$

Then by implementing the current command of motor MT2 as (5.46), the load torque

implemented is:

$$F_L(k-1) = M_A \left(\left(\frac{k_A}{M_A} - \frac{k_x}{M_e} \right) i_x(k-1) - \left(\frac{b_A}{M_A} - \frac{b_x}{M_e} \right) \dot{x}_h(k-1) - d_x(k-1) \right).$$

The test bench behaves as:

$$\dot{x}_h(k+1) = \frac{T_s k_x}{M_e} i_x(k-1) + \left(1 - \frac{T_s b_A}{M_A} \right) \dot{x}_h(k) + F_{Nx}(k) \tag{5.48}$$

where $F_{Nx}(k) = T_s \left(\frac{b_A}{M_A} - \frac{b_x}{M_e} \right) \dot{x}_h(k-1) + T_s d_x(k-1) - \frac{T_s F_{fn}(k)}{M_A}$ can be considered as the disturbance and is assumed within a bounded set $F_{Nx} \in \mathcal{W}_N$.

Let $\xi_x \triangleq (x_h, \dot{x}_h)$ and $i_x(k-1)$ be the state and input respectively, the dynamics (5.48) is represented in state space form as:

$$\xi_x(k+1) = A_e \xi_x(k) + B_e i_x(k-1) + E_e F_{Nx}(k), \tag{5.49}$$

where the matrix A_e, B_e and E_e can be inferred from (5.48).

Let $\bar{\xi}_x(k) \triangleq (\xi_x(k), i_x(k-1))$ be the state of the augmented system. To account for the input delay, the 1-sample delay is incorporated into the X-axis system dynamics (5.49) as:

$$\begin{aligned} \begin{bmatrix} \xi_x(k+1) \\ i_x(k) \end{bmatrix} &= \begin{bmatrix} A_e & B_e \\ 0_{1,2} & 0 \end{bmatrix} \begin{bmatrix} \xi_x(k) \\ i_x(k-1) \end{bmatrix} + \begin{bmatrix} 0_{2,1} \\ 1 \end{bmatrix} i_x(k) + \begin{bmatrix} E_e \\ 0 \end{bmatrix} F_{Nx}(k) \\ &\triangleq \bar{A} \bar{\xi}_x(k) + \bar{B} i_x(k) + \bar{E} F_{Nx}(k). \end{aligned} \tag{5.50}$$

Then this control-oriented model (5.50) is used to compute the RCI set $\mathcal{R}^{\bar{\xi}_x, r_x}$ and $\bar{\xi}_x(k+1) = \bar{A} \bar{\xi}_x(k) + \bar{B} i_x(k)$ is used in the MPC based formulation (5.23) to ensure the tracking bounded control.

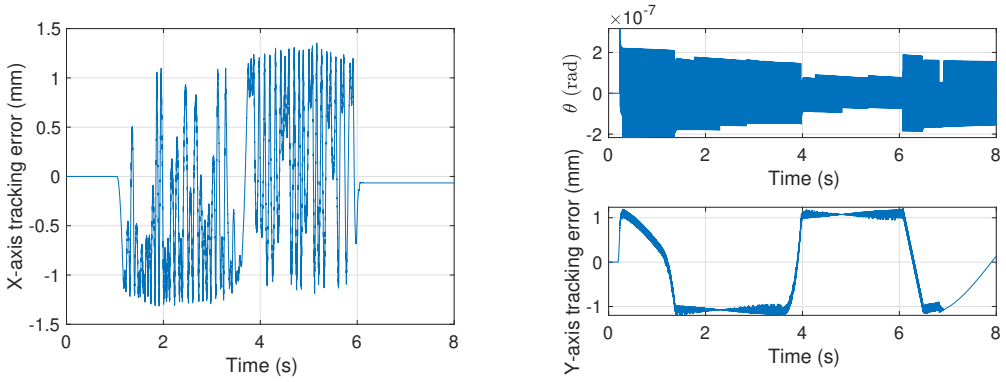

(a) (b)

Fig. 5.21: Experimental end-effector tracking error: (a) X-axis error; (b) rotation angle (up) and Y-axis error (down).

5.6.4 Contouring control performance

The tuning parameters in the MPC cost function are first chosen as the same values used in the simulation parts, i.e., $Q_x = Q_y = 10^5$ and $R_x = 0.1$ and $R_y = diag(0.1, 0.1)$, for contouring error bounded control.

The tracking performance of X and Y axes is given in Fig. 5.21. The maximum tracking errors of X and Y axes are 1.35 mm and 1.23 mm, respectively, and both are within the desired tracking error tolerance. The computed contouring error is demonstrated in Fig. 5.22 and the maximum contouring error is 1.65 mm, which is around 2% of the circle radius.

Then we retune the parameters in (5.23) and (5.26) with a less aggressive way to investigate the effect of tuning onto the contouring performance. The parameters are chosen as $Q_x = Q_y = 10^3$, $R_x = 0.5$ and $R_y = diag(0.5, 0.5)$. The same reference in Fig. 5.11 is used as the position command of X and Y-axis controller. The tracking performance of X and Y axes is shown in Fig. 5.23. The maximum tracking errors on X and Y axes are 1.48 mm and 1.27 mm respectively, which are both within the error tolerance. The computed contouring error is demonstrated in Fig. 5.24 and the maximum contouring error is 1.62 mm, which is around 2% of the circle radius.

By comparing the X-axis tracking errors of the two experiments, i.e., Fig. 5.21a and

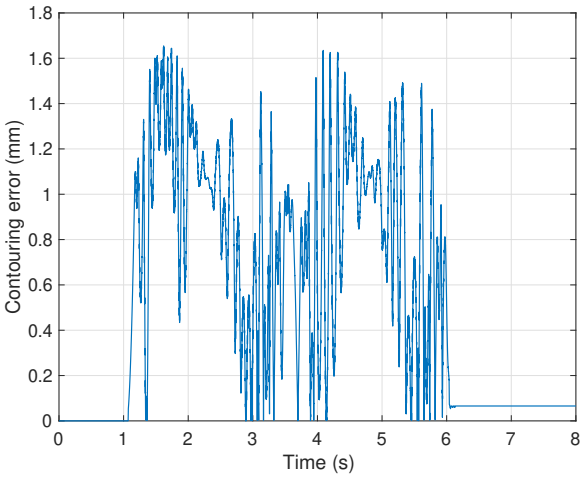

Fig. 5.22: Experimental contouring error during the whole process with $Q_x = Q_y = 10^5$, $R_x = 0.1$ and $R_y = diag(0.1, 0.1)$.

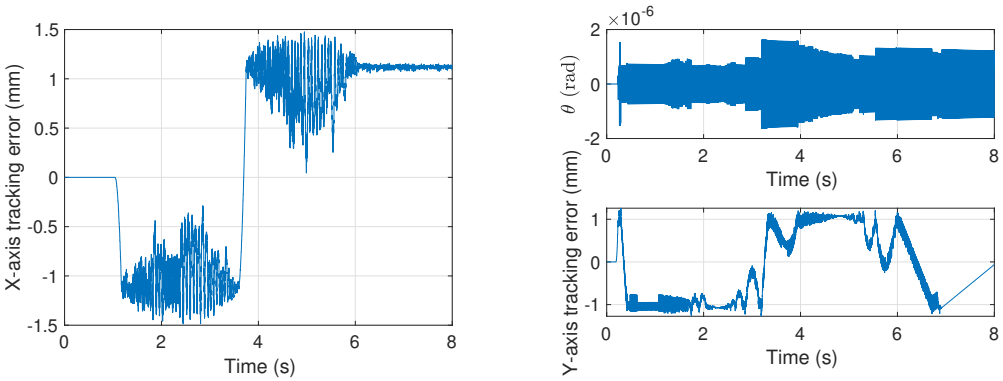

(a) (b)

Fig. 5.23: End-effector tracking performance with less emphasis on tracking: (a) X-axis tracking error; (b) Rotation angle (up) and Y-axis tracking error (down).

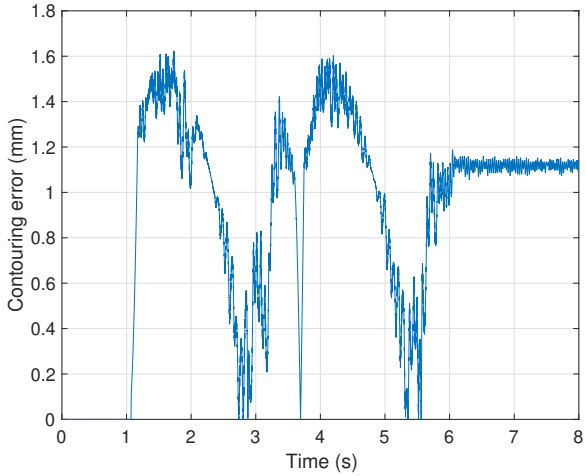

Fig. 5.24: Experimental contouring error during the whole process with $Q_x = Q_y = 10^3$, $R_x = 0.5$ and $R_y = diag(0.5, 0.5)$.

Fig. 5.23a, it can be seen that although putting more weight on tracking error may result in a smaller maximum tracking error, at the same time, it results in more oscillation in tracking. By comparing Fig. 5.22 and Fig. 5.24, it shows that by detuning the proposed controller, the contouring error can still be bounded within the desired tolerance. Although a larger steady-state contouring error is achieved with the detuned controller, this steady-state error can be removed by including the integrator augmentation in the MPC formulation as shown in [135].

When we move to the comparison of the contour achieved by two-different-tuning controllers as shown in Fig. 5.25, it is clear that putting more effort on tracking error results in more obvious vibration along the path and the proposed error bounded control method can ensure the contour error is not violated for different tuning schemes.

By comparing the experimental contouring error in Fig. 5.25a with the simulated result in Fig. 5.14, it can be seen a smaller maximum contouring error is reached during the experiment, but this is achieved at the expense of more introduced oscillation. This is due to the fact that there is a one-sample delay in the control input and the nonlinear friction is included in the disturbance set.

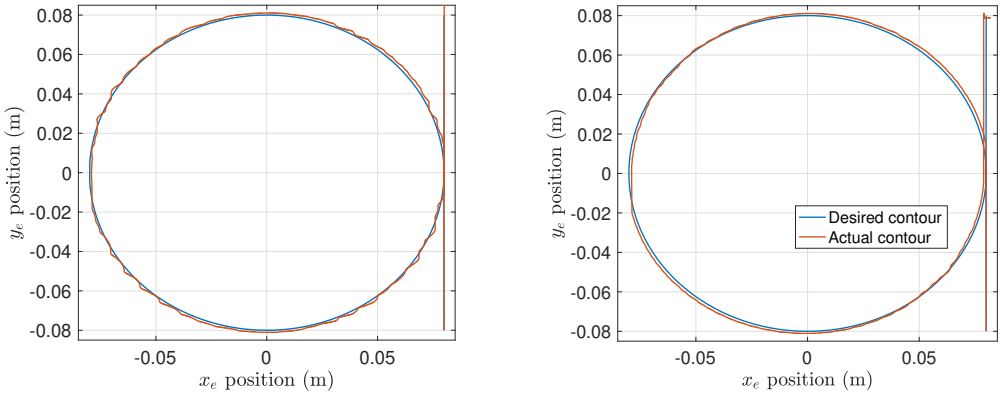

(a) (b)

Fig. 5.25: Desired and actual contour with tuning: (a) $Q_x = Q_y = 10^5$, $R_x = 0.1$ and $R_y = diag(0.1, 0.1)$; (b) $Q_x = Q_y = 10^3$, $R_x = 0.5$ and $R_y = diag(0.5, 0.5)$.

5.7 Summary

In this chapter, a model for a dual-drive industrial gantry machine was proposed and it captured twist in the gantry beam that may lead to contouring control problems. This model was used in the design of two biaxial model predictive based contouring controllers that can guarantee a given contouring tolerance. The effectiveness of the proposed two contouring error bounded control methods are first demonstrated in high-fidelity simulation. Then a back-to-back motor based test bench is designed. Finally, the contouring control based on bounded tracking error is tested on the designed test bench. The experiment results validate the efficacy of the proposed controller in an 'industry-emulated' circumstance.

Chapter 6

Contributions and future work

THIS chapter summarises the contributions of the thesis and lists the articles that are published or submitted for publications as the outcome of this research. Lastly, the possible directions of future work are outlined at last.

6.1 Summary of contributions

As identified in Section 2.4, there were three main research aims, which now forms the basis of contributions in this thesis.

Providing an in-depth benefit and limitation of existing tracking control algorithms

With the ever-increasing demands on industrial machining, there is a need to objectively assess the benefit and limitation of existing tracking control algorithms for systems with structural flexibility, non-collocated control output and external disturbance. In Chapter 3, we build a linear motor based test bench for end-effector tracking control. The tracking performance of widely used cascaded control, cascaded control with notch filter and cascaded control with linear extended state observer are compared in terms of tracking accuracy, control effort and implementation cost. The presented results provide an insight for the practitioners for when the advanced controller is required as an alternative to the PID-based approaches.

Development and demonstration of error bounded tracking control for systems with structural flexibility

The inherent structural flexibility of the industrial system has a detrimental influence on the tracking/contouring accuracy at the end-effector side. Moreover, it is desirable to guarantee the tracking error during the whole process is not violated. In Chapter 4, an error bounded tracking control for systems with structural flexibility and unmeasurable control output is proposed.

The proposed control algorithm involves an augmented control architecture that incorporates the dynamics of the estimated state. By ensuring the error between the reference and estimated end-effector position is in a tighter tolerance, the end-effector tracking is guaranteed within the desired tolerance.

The robust control invariant set (RCI) is essential in guaranteeing the tracking error bound and ensuring the feasibility of MPC for achieving error-bounded control. Based on the fact that the computed RCI is not finitely determined for systems with disturbances, an algorithm for computing the robust RCI set with finite-step termination guarantees is proposed [130, 131]. In Chapter 4, the computed RCI set is incorporated into the controller formulation for tracking error bounded control.

To validate the effectiveness of the proposed control algorithm, reference tracking control of the proposed method is conducted on a linear motor based single-axis test bench, and the results are compared with a cascaded PI controller.

Development and demonstration of contouring error bounded control

Dual drive gantry machines are widely used in industry for manufacturing. However, the non-synchronised movement of the dual drive may lead to deterioration in contouring accuracy. In Chapter 5, we first propose a model for a dual-drive gantry machine, that captures the twist caused by non-synchronised movement.

For applications that involve multi-axis movement, it is desirable the contouring error can be bounded within the desired tolerance during the whole process. In Chapter 5, the

error bounded tracking controller is first extended to the biaxial application to ensure the contouring error is guaranteed [137]. A second MPC is proposed, with a strong assumption on the reference to be tracked. With the explicit consideration of contouring error, the second proposed controller has less conservative performance but is more restrictive in the paths that can be followed. The two designed model predictive control based architectures are able to guarantee a two-dimensional contouring tolerance in the presence of uncertainty arising from imperfect drive synchronisation.

Due to the fact that the position measurement of the end effector is not available for the laser machine, we build a back-to-back motor based test bench for contouring control. The proposed contouring control method based on bounded tracking error is implemented on the built test bench, and the contouring error is shown to be within the desired tolerance.

6.2 Research publications

The research carried out for this thesis has been, or is intended to be, published in the following.

Journal papers

1. M. Yuan, C. Manzie, M. Good, I. Shames, L. Gan, F. Keynejad, and T. Robinette, "Error bounded reference tracking MPC for machines with structural flexibility," *IEEE Transactions on Industrial Electronics*, Early Access, 2019

2. M. Yuan, C. Manzie, M. Good, I. Shames, L. Gan, F. Keynejad, and T. Robinette, "A review of industrial tracking control algorithms," *Control Engineering Practice*, minor amendment, 2019

Conference papers

1. M. Yuan, C. Manzie, L. Gan, M. Good, and I. Shames, "Modelling and contouring error bounded control of a biaxial industrial gantry machine," in *2019 IEEE Conference on Control Technology and Applications (CCTA)*. IEEE, 2019, pp. 388–393.

2. M. Yuan, C. Manzie, M. Good, I. Shames, F. Keynejad, and T. Robinette, "Bounded error tracking control for contouring systems with end effector measurements," in *2019 IEEE International Conference on Industrial Technology (ICIT)*. IEEE, Feb 2019, pp. 66–71.

In preparation

The work in Chapter 5 is currently being prepared for journal submission.

6.3 Future work

6.3.1 Extension to error bounded reference tracking control problem

It was seen in Section 4.3.2 and Section 4.3.3 that the steady state tracking error exists by using the proposed control method. This error can be fully removed by including the integrator augmentation within the MPC formulation as discussed in [135].

Moreover, in Chapter 4, the trajectory tracking control is only tested on the test bench built with one beam with a particular specification. An investigation of the influence of different stiffness beams on the control performance can be conducted.

6.3.2 Extension to contouring error bounded control algorithm

In Section 5.4, the controller is designed based on the assumption the desired contour is a combination of straight line and circular contours. It is desirable to extend the applicable contour to more shapes such as ellipses, and this requires the computation of contouring

error for the particular path. Ultimately, the contouring error bounded control (CEBC) can be extended to free-form contour, but it is likely the upper bound of the estimated contouring error is required.

In addition, reshaping/recalculating the reference online while delivering the bounded contouring error can be investigated.

6.3.3 Develop good tuning guideline for contouring error bound control methods

In Section 5.6.4, the effect of different tuning on the closed-loop system response is investigated. Further research to develop good tuning guidelines for contouring error bounded control with RCI set constraint can be conducted.

6.3.4 Real-time implementation of contouring error bounded control on industrial laser machine

In Section 5.5.2, the high-fidelity contouring control simulation of the method based on explicit computed contouring error is carried. However, as the computation burden increases nonlinearly with respect to system dimension and more than one optimisation problem needs to be solved to determine the suitable RCI set, this CEBC algorithm spends a much longer time in computation than the bounded tracking error based approach. Therefore, in order to facilitate the real-time implementation of contouring error bounded control that relies on explicit contouring error, further reduction of computation burden is required. The potential solution may be applying more advanced/suitable QP solvers, resorting to an embedded system with a fix-point processor or implementing the proposed CEBC method at the drive level instead of using an external target PC.

Moreover, in Chapter 5, the proposed contouring control method is implemented on an 'industry-emulated' test bench instead of a laser machine due to the fact that the real-time measurement of end-effector position is not available. Implementation of the proposed contouring control method on a real industrial machine can further

demonstrate its efficacy of guaranteeing the error bound and show the possibility of its commercial adoption.

It is likely that external sensors such as an industrial accelerometer are required to be installed on the laser head to offer real-time feedback related to end-effector. Moreover, all the measured data needs to be fed into CNC for timestamp matching. The information measured from the end-effector side would allow for a more detailed analysis of the performance of proposed controllers.

References

[1] Statista, "Global motion control market size between 2016 and 2022," 2019. [Online]. Available: https://www.statista.com/statistics/920084/global-motion-control-market-size/

[2] B. Yao, C. Hu, and Q. Wang, "An orthogonal global task coordinate frame for contouring control of biaxial systems," *IEEE/ASME Transactions on Mechatronics*, vol. 17, no. 4, pp. 622–634, Aug. 2012.

[3] K. Erkorkmaz and Y. Altintas, "High speed CNC system design. Part III: high speed tracking and contouring control of feed drives," *International Journal of Machine Tools and Manufacture*, vol. 41, no. 11, pp. 1637–1658, Sep. 2001.

[4] A. D. Luca and B. Siciliano, "Trajectory control of a non-linear one-link flexible arm," *International Journal of Control*, vol. 50, no. 5, pp. 1699–1715, Nov. 1989.

[5] H. N. Rahimi and M. Nazemizadeh, "Dynamic analysis and intelligent control techniques for flexible manipulators: A review," *Advanced Robotics*, vol. 28, no. 2, pp. 63–76, 2014.

[6] P. H. Meckl and W. P. Seering, "Minimizing residual vibration for point-to-point motion," *Journal of Vibration and Acoustics*, vol. 107, no. 4, pp. 378–382, 1985.

[7] C. T. Kiang, A. Spowage, and C. K. Yoong, "Review of control and sensor system of flexible manipulator," *Journal of Intelligent & Robotic Systems*, vol. 77, no. 1, pp. 187–213, Jan. 2015.

[8] P. Poignet, M. Gautier, and W. Khalil, "Modeling, control and simulation of high speed machine tool axes," in *1999 IEEE/ASME International Conference on Advanced Intelligent Mechatronics*. IEEE, 1999, pp. 617–622.

[9] W. He and S. S. Ge, "Vibration control of a flexible beam with output constraint," *IEEE Transactions on Industrial Electronics*, vol. 62, no. 8, pp. 5023–5030, Aug. 2015.

[10] L. Lu, Z. Chen, B. Yao, and Q. Wang, "A two-loop performance-oriented tip-tracking control of a linear-motor-driven flexible beam system with experiments," *IEEE Transactions on Industrial Electronics*, vol. 60, no. 3, pp. 1011–1022, Mar. 2013.

[11] P. J. Serkies and K. Szabat, "Application of the MPC to the position control of the two-mass drive system," *IEEE Transactions on Industrial Electronics*, vol. 60, no. 9, pp. 3679–3688, Sep. 2013.

[12] C. Zhang and Y. Chen, "Tracking control of ball screw drives using ADRC and equivalent-error-model-based feedforward control," *IEEE Transactions on Industrial Electronics*, vol. 63, no. 12, pp. 7682–7692, Dec. 2016.

[13] D. Sepasi, R. Nagamune, and F. Sassani, "Tracking control of flexible ball screw drives with runout effect and mass variation," *IEEE Transactions on Industrial Electronics*, vol. 59, no. 2, pp. 1248–1256, Feb. 2012.

[14] A. Kamalzadeh, D. J. Gordon, and K. Erkorkmaz, "Robust compensation of elastic deformations in ball screw drives," *International Journal of Machine Tools and Manufacture*, vol. 50, no. 6, pp. 559–574, 2010.

[15] Y. Altintas, A. Verl, C. Brecher, L. Uriarte, and G. Pritschow, "Machine tool feed drives," *CIRP Annals - Manufacturing Technology*, vol. 60, no. 2, pp. 779–796, 2011.

[16] A. Kamalzadeh and K. Erkorkmaz, "Compensation of axial vibrations in ball screw drives," *CIRP Annals*, vol. 56, no. 1, pp. 373–378, 2007.

[17] G. Zhu, S. S. Ge, and T. H. Lee, "Simulation studies of tip tracking control of a single-link flexible robot based on a lumped model," *Robotica*, vol. 17, no. 1, pp. 71–78, 1999.

[18] L. Wang, H. Liu, L. Yang, J. Zhang, W. Zhao, and B. Lu, "The effect of axis coupling on machine tool dynamics determined by tool deviation," *International Journal of Machine Tools and Manufacture*, vol. 88, pp. 71–81, 2015.

[19] C. S. Teo, K. K. Tan, S. Y. Lim, S. Huang, and E. B. Tay, "Dynamic modeling and adaptive control of a H-type gantry stage," *Mechatronics*, vol. 17, no. 7, pp. 361–367, 2007.

[20] C. Li, B. Yao, and Q. Wang, "Modeling and synchronization control of a dual drive industrial gantry stage," *IEEE/ASME Transactions on Mechatronics*, vol. 23, no. 6, pp. 2940–2951, Dec. 2018.

[21] L. Wang, S. Chai, D. Yoo, L. Gan, and K. Ng, *PID and predictive control of electrical drives and power converters using Matlab/Simulink*. Wiley, 2014.

[22] S. Ge, T. Lee, and G. Zhu, "Non-model-based position control of a planar multi-link flexible robot," *Mechanical Systems and Signal Processing*, vol. 11, no. 5, pp. 707–724, Sep. 1997.

[23] A. Visioli and G. Legnani, "On the trajectory tracking control of industrial SCARA robot manipulators," *IEEE Transactions on Industrial Electronics*, vol. 49, no. 1, pp. 224–232, 2002.

[24] G. Buja and M. Kazmierkowski, "Direct torque control of PWM inverter-fed AC motors - A survey," *IEEE Transactions on Industrial Electronics*, vol. 51, no. 4, pp. 744–757, Aug. 2004.

[25] G. Goodwin, S. Graebe, and M. Salgado, *Control system design*. Prentice Hall, 2000.

[26] S. Vukosavic and M. Stojic, "Suppression of torsional oscillations in a high-performance speed servo drive," *IEEE Transactions on Industrial Electronics*, vol. 45, no. 1, pp. 108–117, 1998.

[27] K. Szabat and T. Orlowska-Kowalska, "Vibration suppression in a two-mass drive system using PI speed controller and additional feedbacks - Comparative study," *IEEE Transactions on Industrial Electronics*, vol. 54, no. 2, pp. 1193–1206, Apr. 2007.

[28] W. Singhose, "Command shaping for flexible systems: A review of the first 50 years," *International Journal of Precision Engineering and Manufacturing*, vol. 10, no. 4, pp. 153–168, Oct. 2009.

[29] Z. Mohamed and M. Tokhi, "Command shaping techniques for vibration control of a flexible robot manipulator," *Mechatronics*, vol. 14, no. 1, pp. 69–90, Feb. 2004.

[30] N. C. Singer and W. P. Seering, "Preshaping command inputs to reduce system vibration," *Journal of Dynamic Systems, Measurement, and Control*, vol. 112, no. 1, pp. 76–82, Mar. 1990.

[31] N. Singer, W. Singhose, and W. Seering, "Comparison of filtering methods for reducing residual vibration," pp. 208–218, 1999.

[32] W. Singhose and J. Vaughan, "Reducing vibration by digital filtering and input shaping," *IEEE Transactions on Control Systems Technology*, vol. 19, no. 6, pp. 1410–1420, Nov. 2011.

[33] D. J. Gordon and K. Erkorkmaz, "Accurate control of ball screw drives using pole-placement vibration damping and a novel trajectory prefilter," *Precision Engineering*, vol. 37, no. 2, pp. 308–322, Apr. 2013.

[34] D.-H. Lee, J. Lee, and J.-W. Ahn, "Mechanical vibration reduction control of two-mass permanent magnet synchronous motor using adaptive notch filter with fast Fourier transform analysis," *IET Electric Power Applications*, vol. 6, no. 7, p. 455, 2012.

[35] K. Erkorkmaz and Y. Hosseinkhani, "Control of ball screw drives based on disturbance response optimization," *CIRP Annals - Manufacturing Technology*, vol. 62, no. 1, pp. 387–390, 2013.

[36] W. Bahn, T. I. Kim, S. H. Lee, and D. I. D. Cho, "Resonant frequency estimation for adaptive notch filters in industrial servo systems," *Mechatronics*, vol. 41, pp. 45–57, 2017.

[37] L. Wang, *PID control system design and automatic tuning using MATLAB/Simulink*. Wiley, 2020.

[38] C. Bonivento, A. Nersisian, and R. Zanasi, "A cascade structure for robust control design," *IEEE Transactions on Automatic Control*, vol. 39, no. 4, pp. 846–849, 1994.

[39] T. B. Sekara and M. R. Matausek, "Optimization of PID controller based on maximization of the proportional gain under constraints on robustness and sensitivity to measurement noise," *IEEE Transactions on Automatic Control*, vol. 54, no. 1, pp. 184–189, Jan. 2009.

[40] O. Garpinger, T. Hägglund, and K. J. Åström, "Performance and robustness trade-offs in PID control," *Journal of Process Control*, vol. 24, no. 5, pp. 568–577, May 2014.

[41] H. Van Brussel and P. Van den Braembussche, "Robust control of feed drives with linear motors," *CIRP Annals*, vol. 47, no. 1, pp. 325–328, 1998.

[42] N. Amann, D. H. Owens, E. Rogers, and A. Wahl, "An H_∞ approach to linear iterative learning control design," *International Journal of Adaptive Control and Signal Processing*, vol. 10, pp. 767–781, Nov. 1996.

[43] W. Li and P. X. Liu, "Robust adaptive tracking control of uncertain electrostatic micro-actuators with H-infinity performance," *Mechatronics*, vol. 19, no. 5, pp. 591–597, Aug. 2009.

[44] X. Wang and D. Chen, "Output tracking control of a one-link flexible manipulator via causal inversion," *IEEE Transactions on Control Systems Technology*, vol. 14, no. 1, pp. 141–148, Jan. 2006.

[45] J. J. Slotine and S. S. Sastry, "Tracking control of non-linear systems using sliding surfaces, with application to robot manipulators," *International Journal of Control*, vol. 38, no. 2, pp. 465–492, 1983.

[46] J.-M. Yang and J.-H. Kim, "Sliding mode control for trajectory tracking of nonholonomic wheeled mobile robots," *IEEE Transactions on Robotics and Automation*, vol. 15, no. 3, pp. 578–587, Jun. 1999.

[47] Y. Altintas, K. Erkorkmaz, and W.-H. Zhu, "Sliding mode controller design for high speed feed drives," *CIRP Annals*, vol. 49, no. 1, pp. 265–270, 2000.

[48] K. Åström, H. Panagopoulos, and T. Hägglund, "Design of PI controllers based on non-convex optimization," *Automatica*, vol. 34, no. 5, pp. 585–601, May 1998.

[49] W. Tan, J. Liu, T. Chen, and H. J. Marquez, "Comparison of some well-known PID tuning formulas," *Computers and Chemical Engineering*, vol. 30, no. 9, pp. 1416–1423, 2006.

[50] N. J. Killingsworth and M. Krstic, "PID tuning using extremum seeking: Online, model-free performance optimization," *IEEE Control Systems*, vol. 26, no. 1, pp. 70–79, Feb. 2006.

[51] M. Steinbuch and M. Norg, "Advanced motion control: An industrial perspective," *European Journal of Control*, vol. 4, no. 4, pp. 278–293, Jan. 1998.

[52] C. Aguilar-Avelar and J. Moreno-Valenzuela, "New feedback linearization based control for arm trajectory tracking of the Furuta pendulum," *IEEE/ASME Transactions on Mechatronics*, vol. 21, no. 2, pp. 638–648, Apr. 2016.

[53] W. H. Chen, J. Yang, L. Guo, and S. Li, "Disturbance-observer-based control and related methods - An overview," *IEEE Transactions on Industrial Electronics*, vol. 63, no. 2, pp. 1083–1095, 2016.

[54] K. Ohishi, K. Ohnishi, and K. Miyachi, "Torque-speed regulation of DC motor based on load torque estimation method," pp. 1209–1218, 1983.

[55] K. Ohishi, Y. Ogino, and M. Hotta, "High performance motion control based on model following acceleration joint control method," in *Proceedings, 1989 International Conference on Robotics and Automation*. IEEE Comput. Soc. Press, 1989, pp. 1792–1798.

[56] T. Umeno and Y. Hori, "Robust speed control of DC servomotors using modern two degrees-of-freedom controller design," *IEEE Transactions on Industrial Electronics*, vol. 38, no. 5, pp. 363–368, 1991.

[57] W.-S. Huang, C.-W. Liu, P.-L. Hsu, and S.-S. Yeh, "Precision control and compensation of servomotors and machine tools via the disturbance observer," *IEEE Transactions on Industrial Electronics*, vol. 57, no. 1, pp. 420–429, Jan. 2010.

[58] K. K. Tan, T. H. Lee, H. F. Dou, S. J. Chin, and S. Zhao, "Precision motion control with disturbance observer for pulsewidth-modulated-driven permanent-magnet linear motors," *IEEE Transactions on Magnetics*, vol. 39, no. 3, pp. 1813–1818, May 2003.

[59] J. Solsona, M. Valla, and C. Muravchik, "Nonlinear control of a permanent magnet synchronous motor with disturbance torque estimation," *IEEE Transactions on Energy Conversion*, vol. 15, no. 2, pp. 163–168, Jun. 2000.

[60] C. Kempf and S. Kobayashi, "Disturbance observer and feedforward design for a high-speed direct-drive positioning table," *IEEE Transactions on Control Systems Technology*, vol. 7, no. 5, pp. 513–526, 1999.

[61] H. S. Lee and M. Tomizuka, "Robust motion controller design for high-accuracy positioning systems," *IEEE Transactions on Industrial Electronics*, vol. 43, no. 1, pp. 48–55, 1996.

[62] Z. Jamaludin, H. Van Brussel, and J. Swevers, "Friction compensation of an XY feed table using friction-model-based feedforward and an inverse-model-based disturbance observer," *IEEE Transactions on Industrial Electronics*, vol. 56, no. 10, pp. 3848–3853, Oct. 2009.

[63] K. Tan, S. Lim, S. Huang, H. Dou, and T. Giam, "Coordinated motion control of moving gantry stages for precision applications based on an observer-augmented composite controller," *IEEE Transactions on Control Systems Technology*, vol. 12, no. 6, pp. 984–991, Nov. 2004.

[64] Y. Oh and W. K. Chung, "Disturbance-observer-based motion control of redundant manipulators using inertially decoupled dynamics," *IEEE/ASME Transactions on Mechatronics*, vol. 4, no. 2, pp. 133–146, Jun. 1999.

[65] K. S. Eom, I. H. Suh, and W. K. Chung, "Disturbance observer based path tracking control of robot manipulator considering torque saturation," *Mechatronics*, vol. 11, no. 3, pp. 325–343, Apr. 2001.

[66] P. Zhou, W. Dai, and T. Y. Chai, "Multivariable disturbance observer based advanced feedback control design and its application to a grinding circuit," *IEEE Transactions on Control Systems Technology*, vol. 22, no. 4, pp. 1474–1485, 2014.

[67] J. Han, "The extended state observer of a class of uncertain systems," *in Chinese, Control and Decision*, vol. 10, no. 1, pp. 85–88, 1995.

[68] ——, "From PID to active disturbance rejection control," *IEEE Transactions on Industrial Electronics*, vol. 56, no. 3, pp. 900–906, Mar. 2009.

[69] H. Liu and S. Li, "Speed control for PMSM servo system using predictive functional control and extended state observer," *IEEE Transactions on Industrial Electronics*, vol. 59, no. 2, pp. 1171–1183, 2012.

[70] J. Yao, Z. Jiao, and D. Ma, "Adaptive robust control of DC motors with extended state observer," *IEEE Transactions on Industrial Electronics*, vol. 61, no. 7, pp. 3630–3637, Jul. 2014.

[71] Y. Su, C. Zheng, and B. Duan, "Automatic disturbances rejection controller for precise motion control of permanent-magnet synchronous motors," *IEEE Transactions on Industrial Electronics*, vol. 52, no. 3, pp. 814–823, Jun. 2005.

[72] H. Sira-Ramirez, J. Linares-Flores, C. Garcia-Rodriguez, and M. A. Contreras-Ordaz, "On the control of the permanent magnet synchronous motor: An active disturbance rejection control approach," *IEEE Transactions on Control Systems Technology*, vol. 22, no. 5, pp. 2056–2063, Sep. 2014.

[73] Y. Su, B. Duan, C. Zheng, Y. Zhang, G. Chen, and J. Mi, "Disturbance-rejection high-precision motion control of a Stewart platform," *IEEE Transactions on Control Systems Technology*, vol. 12, no. 3, pp. 364–374, May 2004.

[74] S. Talole, J. Kolhe, and S. Phadke, "Extended-state-observer-based control of flexible-joint system with experimental validation," *IEEE Transactions on Industrial Electronics*, vol. 57, no. 4, pp. 1411–1419, Apr. 2010.

[75] Y. Huang, Z. Luo, M. Svinin, T. Odashima, and S. Hosoe, "Extended state observer based technique for control of robot systems," in *Proceedings of the 4th World Congress on Intelligent Control and Automation*, vol. 4. IEEE, 2002, pp. 2807–2811.

[76] B. Sun and Z. Gao, "A DSP-based active disturbance rejection control design for a 1-kW H-bridge DC–DC power converter," *IEEE Transactions on Industrial Electronics*, vol. 52, no. 5, pp. 1271–1277, 2005.

[77] J. Liu, S. Vazquez, S. Member, L. Wu, and S. Member, "Extended state observer-based sliding-mode control for three-phase power converters," *IEEE Transactions on Industrial Electronics*, vol. 64, no. 1, pp. 22–31, 2017.

[78] J. Yang, J. Wang, B. Wu, S. Li, and Q. Li, "Extended state observer-based sliding mode control for PWM-based DC–DC buck power converter systems with mismatched disturbances," *IET Control Theory & Applications*, vol. 9, no. 4, pp. 579–586, Feb. 2015.

[79] Texas Instruments, "TMS320F28069M, TMS320F28068M InstaSPIN^{TM}-MOTION software technical reference manual," 2014. [Online]. Available: http://www.ti.com/lit/ug/spruhj0b/spruhj0b.pdf

[80] B. Guo and Z. Zhao, "On the convergence of an extended state observer for nonlinear systems with uncertainty," *Systems & Control Letters*, vol. 60, no. 6, pp. 420–430, Jun. 2011.

[81] Q. Zheng, L. Q. Gaol, and Z. Gao, "On stability analysis of active disturbance rejection control for nonlinear time-varying plants with unknown dynamics," in *2007 46th IEEE Conference on Decision and Control*. IEEE, 2007, pp. 3501–3506.

[82] X. Yang and Y. Huang, "Capabilities of extended state observer for estimating uncertainties," in *2009 American Control Conference*. IEEE, 2009, pp. 3700–3705.

[83] H. K. Khalil, *Nonlinear Systems*, 3rd ed. Pearson, 2002.

[84] Y. Su, C. Zheng, D. Sun, and B. Duan, "A simple nonlinear velocity estimator for high-performance motion control," *IEEE Transactions on Industrial Electronics*, vol. 52, no. 4, pp. 1161–1169, Aug. 2005.

[85] Z. S. Hou and Z. Wang, "From model-based control to data-driven control: Survey, classification and perspective," *Information Sciences*, vol. 235, pp. 3–35, 2013.

[86] S.-M. Suh, C. C. Chung, and S.-H. Lee, "Discrete-time LQG/LTR dual-stage controller design in magnetic disk drives," *IEEE Transactions on Magnetics*, vol. 37, no. 4, pp. 1891–1895, Jul. 2001.

[87] A. S. Morris and A. Madani, "Quadratic optimal control of a two-flexible-link robot manipulator," *Robotica*, vol. 16, no. 1, pp. 97–108, Jan. 1998.

[88] S. Carrière, S. Caux, and M. Fadel, "Optimised speed control in state space for PMSM direct drives," *IET Electric Power Applications*, vol. 4, no. 3, pp. 158–168, 2010.

[89] S. P. Bhat and D. K. Miu, "Precise point-to-point positioning control of flexible structures," *Journal of Dynamic Systems, Measurement, and Control*, vol. 112, no. 4, pp. 667–674, Dec. 1990.

[90] M. Dadfarnia, N. Jalili, B. Xian, and D. Dawson, "Lyapunov-based piezoelectric control of flexible cartesian robot manipulators," in *Proceedings of the 2003 American Control Conference, 2003.* IEEE, 2003, pp. 5227–5232.

[91] S. K. Tso, T. W. Yang, W. L. Xu, and Z. Q. Sun, "Vibration control for a flexible-link robot arm with deflection feedback," *International Journal of Non-Linear Mechanics*, vol. 38, pp. 51–62, 2003.

[92] C. Makkar, G. Hu, W. Sawyer, and W. Dixon, "Lyapunov-based tracking control in the presence of uncertain nonlinear parameterizable friction," *IEEE Transactions on Automatic Control*, vol. 52, no. 10, pp. 1988–1994, Oct. 2007.

[93] M. Bodson, J. Chiasson, R. Novotnak, and R. Rekowski, "High-performance nonlinear feedback control of a permanent magnet stepper motor," *IEEE Transactions on Control Systems Technology*, vol. 1, no. 1, pp. 5–14, Mar. 1993.

[94] C. F. Castillo-Berrio and V. Feliu-Batlle, "Vibration-free position control for a two degrees of freedom flexible-beam sensor," *Mechatronics*, vol. 27, pp. 1–12, 2015.

[95] J. M. Maciejowski, *Predictive Control: With Constraints*, 1st ed. Prentice Hall, 2002.

[96] S. Qin and T. A. Badgwell, "A survey of industrial model predictive control technology," *Control Engineering Practice*, vol. 11, no. 7, pp. 733–764, Jul. 2003.

[97] P. Boucher, D. Dumur, and K. F. Rahmani, "Generalized predictive cascade control (GPCC) for machine tools drives," *CIRP Annals*, vol. 39, no. 1, pp. 357–360, 1990.

[98] D. Dumur, P. Boucher, and G. Ramond, "Direct adaptive generalized predictive control. Application to motor drives with flexible modes," *CIRP Annals*, vol. 49, no. 1, pp. 271–274, 2000.

[99] E. Gilbert, I. Kolmanovsky, and K. Tan, "Nonlinear control of discrete-time linear systems with state and control constraints: A reference governor with global convergence properties," in *Proceedings of 1994 33rd IEEE Conference on Decision and Control*, vol. 1. IEEE, 1994, pp. 144–149.

[100] E. Garone, S. Di Cairano, and I. Kolmanovsky, "Reference and command governors for systems with constraints: A survey on theory and applications," *Automatica*, vol. 75, pp. 306–328, Jan. 2017.

[101] L. Chisci and G. Zappa, "Dual mode predictive tracking of piecewise constant references for constrained linear systems," *International Journal of Control*, vol. 76, no. 1, pp. 61–72, Jan. 2003.

[102] D. Limon, I. Alvarado, T. Alamo, and E. Camacho, "MPC for tracking piecewise constant references for constrained linear systems," *Automatica*, vol. 44, no. 9, pp. 2382–2387, Sep. 2008.

[103] U. Maeder and M. Morari, "Offset-free reference tracking with model predictive control," *Automatica*, vol. 46, no. 9, pp. 1469–1476, 2010.

[104] L. Wang, C. T. Freeman, S. Chai, and E. Rogers, "Predictive-repetitive control with constraints: From design to implementation," *Journal of Process Control*, vol. 23, no. 7, pp. 956–967, 2013.

[105] L. Wang, "Tutorial review on repetitive control with anti-windup mechanisms," *Annual Reviews in Control*, vol. 42, pp. 332–345, 2016.

[106] S. Di Cairano and F. Borrelli, "Reference tracking with guaranteed error bound for constrained linear systems," *IEEE Transactions on Automatic Control*, vol. 61, no. 8, pp. 2245–2250, Aug. 2016.

[107] F. Blanchini, "Set invariance in control," *Automatica*, vol. 35, no. 11, pp. 1747–1767, 1999.

[108] S. Rakovic, E. Kerrigan, D. Mayne, and J. Lygeros, "Reachability analysis of discrete-time systems with disturbances," *IEEE Transactions on Automatic Control*, vol. 51, no. 4, pp. 546–561, Apr. 2006.

[109] M. Rungger and P. Tabuada, "Computing robust controlled invariant sets of linear systems," *IEEE Transactions on Automatic Control*, vol. 62, no. 7, pp. 3665–3670, Jul. 2017.

[110] G.-C. Chiu and M. Tomizuka, "Contouring control of machine tool feed drive systems: A task coordinate frame approach," *IEEE Transactions on Control Systems Technology*, vol. 9, no. 1, pp. 130–139, 2001.

[111] L. Tang and R. G. Landers, "Multiaxis contour control - the state of the art," *IEEE Transactions on Control Systems Technology*, vol. 21, no. 6, pp. 1997–2010, 2013.

[112] Y. Koren, "Cross-coupled biaxial computer control for manufacturing systems," *Journal of Dynamic Systems, Measurement, and Control*, vol. 102, no. 4, pp. 265–272, Dec. 1980.

[113] C.-C. Lo and Y. Koren, "Evaluation of servo-controllers for machine tools," in *1992 American Control Conference*, vol. 1. IEEE, Jun. 1992, pp. 370–374.

[114] Y. Koren and C.-C. Lo, "Variable-gain cross-coupling controller for contouring," *CIRP Annals*, vol. 40, no. 1, pp. 371–374, 1991.

[115] C.-C. Lo and C. Y. Chung, "Tangential-contouring controller for biaxial motion control," *Journal of Dynamic Systems, Measurement and Control, Transactions of the ASME*, vol. 121, no. 1, pp. 126–129, 1999.

[116] C.-L. Chen and C.-C. Peng, "Coordinate transformation based contour following control for robotic systems," *Advances in Robot Manipulators*, 2010.

[117] A. El Khalick and N. Uchiyama, "Discrete-time model predictive contouring control for biaxial feed drive systems and experimental verification," *Mechatronics*, vol. 21, no. 6, pp. 918–926, 2011.

[118] S.-L. Chen, H.-L. Liu, and S. C. Ting, "Contouring control of biaxial systems based on polar coordinates," *IEEE/ASME Transactions on Mechatronics*, vol. 7, no. 3, pp. 329–345, Sep. 2002.

[119] J.-H. Chin and T.-C. Lin, "Cross-coupled precompensation method for the contouring accuracy of computer numerically controlled machine tools," *International Journal of Machine Tools and Manufacture*, vol. 37, no. 7, pp. 947–967, Jul. 1997.

[120] C. S. Chen and L. Y. Chen, "Cross-coupling position command shaping control in a multi-axis motion system," *Mechatronics*, vol. 21, no. 3, pp. 625–632, 2011.

[121] D. Lam, C. Manzie, and M. C. Good, "Model predictive contouring control for biaxial systems," *IEEE Transactions on Control Systems Technology*, vol. 21, no. 2, pp. 552–559, Mar. 2013.

[122] C. Okwudire and Y. Altintas, "Minimum tracking error control of flexible ball screw drives using a discrete-time sliding mode controller," *Journal of Dynamic Systems, Measurement, and Control*, vol. 131, no. 5, p. 051006, Aug. 2009.

[123] A. Hace, K. Jezernik, and A. Šabanović, "SMC with disturbance observer for a linear belt drive," *IEEE Transactions on Industrial Electronics*, vol. 54, no. 6, pp. 3402–3412, 2007.

[124] E. J. Fuentes, C. A. Silva, and J. I. Yuz, "Predictive speed control of a two-mass system driven by a permanent magnet synchronous motor," *IEEE Transactions on Industrial Electronics*, vol. 59, no. 7, pp. 2840–2848, Jul. 2012.

[125] G. Zhu, S. S. Ge, and T. H. Lee, "Simulation studies of tip tracking control of a single-link flexible robot based on a lumped model," *Robotica*, vol. 17, no. 1, pp. 71–78, 1999.

[126] J. F. Gieras, Z. J. Piech, and B. Tomczuk, *Linear Synchronous Motors: Transportation and Automation Systems*. CRC Press, 1999.

[127] C. Hu, B. Yao, and Q. Wang, "Coordinated adaptive robust contouring control of an industrial biaxial precision gantry with cogging force compensations," *IEEE Transactions on Industrial Electronics*, vol. 57, no. 5, pp. 1746–1754, May 2010.

[128] D. P. Hess and A. Soom, "Friction at a lubricated line contact operating at oscillating sliding velocities," *Journal of Tribology*, vol. 112, no. 1, p. 147, 1990.

[129] D. Karnopp, "Computer simulation of stick-slip friction in mechanical dynamic systems," *Journal of Dynamic Systems, Measurement, and Control*, vol. 107, no. 1, p. 100, 1985.

[130] M. Yuan, C. Manzie, M. Good, I. Shames, F. Keynejad, and T. Robinette, "Bounded error tracking control for contouring systems with end effector measurements," in *2019 IEEE International Conference on Industrial Technology (ICIT)*. IEEE, Feb. 2019, pp. 66–71.

[131] M. Yuan, C. Manzie, M. Good, I. Shames, L. Gan, F. Keynejad, and T. Robinette, "Error-bounded reference tracking MPC for machines with structural flexibility," *IEEE Transactions on Industrial Electronics*, 2019.

[132] S. Rakovic, E. Kerrigan, K. Kouramas, and D. Mayne, "Invariant approximations of the minimal robust positively invariant set," *IEEE Transactions on Automatic Control*, vol. 50, no. 3, pp. 406–410, Mar. 2005.

[133] J. Lofberg, "YALMIP: A toolbox for modeling and optimization in MATLAB," in *2004 IEEE International Conference on Robotics and Automation (IEEE Cat. No.04CH37508)*. IEEE, 2004, pp. 284–289.

[134] M. Herceg, M. Kvasnica, C. N. Jones, and M. Morari, "Multi-parametric toolbox 3.0," in *2013 European Control Conference (ECC)*. IEEE, Jul. 2013, pp. 502–510.

[135] M. A. Stephens, C. Manzie, and M. C. Good, "Model predictive control for reference tracking on an industrial machine tool servo drive," *IEEE Transactions on Industrial Informatics*, vol. 9, no. 2, pp. 808–816, May 2013.

[136] J. Mattingley and S. Boyd, "CVXGEN: A code generator for embedded convex optimization," *Optimization and Engineering*, vol. 13, no. 1, pp. 1–27, Mar. 2012.

[137] M. Yuan, C. Manzie, L. Gan, M. Good, and I. Shames, "Modelling and contouring error bounded control of a biaxial industrial gantry machine," in *2019 IEEE Conference on Control Technology and Applications (CCTA)*. IEEE, 2019, pp. 388–393.